

EVERT NASEDKIN

SUB-STELLAR ATMOSPHERES IN THE MID-INFRARED

Simulated Instrumental Constraints on Sub-Stellar Atmospheric Retrievals for the James Webb Space Telescope's Mid-Infrared Instrument.

Supervised by:

Sascha Quanz & Polychronis Patapis

Evert Nasedkin

Sub-Stellar Atmospheres in the Mid-Infrared

*Simulated Instrumental Constraints on Sub-Stellar Atmospheric Retrievals for the
James Webb Space Telescope's Mid-Infrared Instrument.*

Supervised by: Sascha Quanz and Polychronis Patapis

Copyright © 2020

TITLEBACK

This document was written with L^AT_EX on Ubuntu using ArsClassica, de-signed by André Miede.

CONTACTS

 evertn@student.ethz.ch

Declaration of originality

The signed declaration of originality is a component of every semester paper, Bachelor's thesis, Master's thesis and any other degree paper undertaken during the course of studies, including the respective electronic versions.

Lecturers may also require a declaration of originality for other written papers compiled for their courses.

I hereby confirm that I am the sole author of the written work here enclosed and that I have compiled it in my own words. Parts excepted are corrections of form and content by the supervisor .

Title of work (in block letters):

SUB-STELLAR ATMOSPHERES IN THE MID INFRARED:

SIMULATED INSTRUMENTAL CONSTRAINTS ON SUB-STELLAR ATMOSPHERIC RETRIEVALS
FOR THE JAMES WEBB SPACE TELESCOPE'S MID INFRARED INSTRUMENT

Authored by (in block letters):

For papers written by groups the names of all authors are required.

Name(s):

NASEDKIN

First name(s):

NICHOLAS EVERT

With my signature I confirm that

- I have committed none of the forms of plagiarism described in the '[Citation etiquette](#)' information sheet.
- I have documented all methods, data and processes truthfully.
- I have not manipulated any data.
- I have mentioned all persons who were significant facilitators of the work .

I am aware that the work may be screened electronically for plagiarism.

Place, date

Zurich, 2020-03-30

Signature(s)



For papers written by groups the names of all authors are required. Their signatures collectively guarantee the entire content of the written paper.

ACKNOWLEDGEMENTS

*Astronomy compels the soul to look upwards
and leads us from this world to another.*

— Plato

First and foremost I'd like to thank my supervisor, Sascha Quanz, for providing me with the guidance and resources with which to pursue this project. You have been an inspiration, and my experience here at ETH has set me down an exciting path in exoplanet research. It has been an honour to be a part of the growth of your group for the last two years, and I look forward to working with you in the future.

I have to thank the rest of the Exoplanet and Habitability Group for accepting me and teaching me over the last few years. Bibiana, thank you for our coffee discussions and your editing of this manuscript, I can't wait to see where you will go next. To Judit Szulagyi, I cannot thank you enough for your constant support and mentorship, both in and outside of academia. Your advice has helped shape the course of my future, and I will always be grateful for that. I'd especially like to thank Gabrielle Cugno for always answering my questions, Eleonara Alei for our discussions of atmospheres and music and Adrian Glauser for getting me started at ETH and involved with this project. And to all the rest: Anna, Franziska, Greta, Haiyang, Hans-Martin, Jie, Natalia, Silvan, Timothy and Tomas, thank you for our discussions, literature meetings, lessons and laughter. It has been a true pleasure to be a part of this group, I will miss it.

Additional thanks to Paul Mollière for our discussions of petitRADTRANS and atmospheric retrievals, and for encouraging me to continue in my work. I would have been lost multiple times throughout this project without your insight.

I must also thank my Zurich friends, without you it would have been impossible to survive here. You have all made this a truly memorable experience. Special thanks to Francisco for proofreading this document. Of course I have to thank my parents, Bill and Sherry, for supporting me in every possible way: not just here in Zurich, but throughout my life. I am eternally grateful for your love and encouragement.

Last, and certainly not least, I have to thank Polychronis Patapis for his supervision of this project. You got me into this and have set me on a path that I am excited to explore. I can't imagine many others answering my constant questions late at night, and for pushing me to always do better. I'm so grateful to call you not just my supervisor, but my friend. There will always be coffee waiting for you whenever you come to visit.

ABSTRACT

Following its launch in 2021, the James Webb Telescope will provide the best infrared observations of exoplanets and brown dwarfs to date. In particular, the Mid-Infrared Instrument (MIRI), will allow for medium resolution spectroscopy across a wide wavelength band, from $4.9\text{-}28.8\mu\text{m}$. This will allow us to derive atmospheric properties of objects at lower temperatures than currently possible. MIRI's medium resolution spectrometer (MRS) is an integrated field unit that will perform these observations, providing both spatial and spectral information about targets. Understanding the instrumental effects is critical to analyzing data from MIRI. With that in mind, the MIRISIM instrumental simulator was developed to provide observational simulations of the various sub instruments of MIRI.

This thesis improves the implementation of a thin-film fringing model for point sources to MIRISIM, considering how the fringing effect from the detector layers varies with position. Fringing is a periodic, wavelength dependent effect, and thus has a strong impact on any spectroscopic observations. A comparison to the existing model was made, demonstrating the necessity of considering this effect when analyzing data. A new point-source based model was implemented in MIRISIM, and the current state-of-the-art corrections compared using the cross correlation technique. We also explore using this technique to identify the presence of individual species, or to infer the presence of an object in an IFU data cube.

Understanding the instrumental effects is key to quantifying the ability of MIRI to derive atmospheric properties. Existing literature has considered the NIRCAM instrument and the MIRI Low-Resolution Spectrometer, but to date no retrieval studies have been performed using MIRISIM, or for the MIRI MRS, though it is critical to extend wavelength coverage to improve the results of an atmospheric retrieval. Model emission spectra for three JWST GTO and ERS targets, VHS-1256b, WISE 0855 and 2M1207b, were generated using petitRADTRANS. These were processed using MIRISIM using the proposed observing parameters and reduced with the JWST pipeline to produce a mock observation. We found temperature, radii and atmospheric parameters for each of the targets, as well as the abundances for individual species. This was done using two subsets of the MRS wavelength range, as well as comparing a realistic fringing case to an optimistic correction.

CONTENTS

1	INTRODUCTION	1
1.1	Exoplanets	1
1.2	Brown Dwarfs	7
1.2.1	Observational Properties	7
1.3	Motivation	9
1.3.1	Current Status of Atmospheric Characterization	9
1.3.2	JWST Studies	12
1.3.3	Biosignatures and Future Missions	12
1.4	Thesis Overview	13
2	MIRI: THE MID-INFRARED INSTRUMENT	15
2.1	The James Webb Space Telescope	15
2.2	MIRI	16
2.3	The Medium Resolution Spectrograph	17
2.3.1	Coordinates	17
2.3.2	Integral Field Spectroscopy	18
2.3.3	Detectors	19
2.4	Observations	20
2.4.1	Dithering	21
2.4.2	Exposure time calculations	21
3	FRINGING EFFECTS IN MIRI	23
3.1	Fringing	23
3.1.1	Current Status of Fringing Correction	25
3.2	MIRISIM	25
3.2.1	Architecture	26
3.2.2	Data Products	27
3.2.3	Fringing Model Implementation	28
3.3	JWST Pipeline	29
3.3.1	Stage 1 Processing	29
3.3.2	Stage 2 Processing	30
3.4	Cross Correlation	34
3.4.1	Residual Statistics	35
3.4.2	Molecular Mapping	35
3.5	Results	37
3.5.1	Molecular Mapping	40
3.5.2	Discussion	43
4	ATMOSPHERIC RETRIEVALS	45
4.1	petitRADTRANS	45
4.1.1	Radiative Transfer	46
4.1.2	Opacity Sources	47
4.2	Bayesian Inference	48
4.2.1	Nested Sampling	49
4.2.2	Multinest	50
4.3	Observations	51
4.4	Methods	54

4.4.1	Spectra Generation	54
4.4.2	Atmospheric Retrieval Setup	55
4.5	Results	57
4.5.1	VHS-1256b	57
4.5.2	WISE 0855	65
4.5.3	2M1207b	69
4.5.4	Fringing Comparison	71
4.5.5	Discussion	71
5	DISCUSSION AND CONCLUSIONS	73
5.1	Summary of Results	73
5.1.1	Fringing in the MIRI MRS	73
5.1.2	Effects of fringing on atmospheric retrievals	74
5.1.3	Atmospheric retrievals with the MIRI MRS	74
5.2	Discussion	75
5.2.1	Implications for GTO Observations	75
5.2.2	Caveats and Limitations	76
5.2.3	Future work	76
A	APPENDIX	79
A.1	Extracted Spectra	79
A.2	Cross Correlations	80
A.3	Full Posterior Distributions	84
A.4	Package Requirements	90
	WORKS CITED	91

1

INTRODUCTION

Since the first detection of a planet around a sun-like star (Mayor and Queloz, 1995) the field of exoplanets has evolved rapidly. Thousands of companions have been identified using the radial velocity and transit detection methods, and a handful have been imaged directly using both ground and space based observatories. In the last decade, many advances have been made that allow us to begin to characterize the properties of a few of these planets using spectroscopy. With the launch of the James Webb Space Telescope (JWST) in 2021, and the dawn of the era of extremely large telescopes, we will be able to peer deeper into these planets and further constrain atmospheric or geological properties. This will allow us to answer questions about their formation history, climate, and in the long term even the prospects for habitability and life.

JWST will operate in near to mid infrared wavelengths, which will provide a new window into studying the atmospheres of exoplanets and brown dwarfs. The Mid Infrared Instrument (MIRI) will provide unprecedented spectral resolution in the mid infrared, allowing for the measurement of composition, pressure and temperature. Novel instrumentation does not come without challenges. Optical and instrumental effects will constrain the ability to which we can measure spectral features, which will ultimately limit the science that can be accomplished.

In this thesis, we will measure the impact of thin-film fringing in the layers of the detectors in the MIRI Medium-Resolution Spectrometer (MRS) on measurements of atmospheric parameters of brown dwarfs and exoplanets. This will yield a baseline for determining the level of correction necessary to minimize the impact of fringing, as well as providing a first look into the ability of the MRS to characterize atmospheres through mid-infrared spectroscopic observations, and using modern atmospheric retrieval techniques.

1.1 EXOPLANETS

The last quarter century of observations has revealed the diversity of exoplanets and extra-solar systems. Both the architecture and individual planetary characteristics vary greatly when compared to each other, as well as to our own solar system. From the hot Jupiters initially found by (Mayor and Queloz, 1995) to the thousands of planets discovered by the Kepler mission, the variety in exoplanets has raised questions about their formation and development, as well as their present day structure and climate. Improvements to observational techniques have allowed us to improve our understanding of these planets. Secondary eclipse and transmission spectroscopy has opened the door to the study of planets in close orbits to their host stars, while emission spectroscopy of young planet has allowed for constraints on

models of planet formation. Over the next decades new instruments will be developed that improve sensitivity, allowing us to study smaller, colder and fainter planets. This will address one of the ultimate goals of exoplanet science in studying the atmospheric and surface features of an earth-like planet in the hopes of detecting unambiguous biosignatures.

Of particular interest are observable features that allow us to measure physical properties of exoplanets. The radial velocity (RV) method provides a measure of the planet mass, while a transit can constrain the radius. Already these properties tell us something about the overall structure of the planet. Spectroscopy can provide insight into the composition of the planet's atmosphere, as well as its temperature and pressure. These properties are linked to its age and location of formation in the circumstellar disk. The atmosphere, combined with the distance between the planet and its star determine the climate of the planet.

Direct Imaging

While the majority of exoplanet detections have been made using the radial velocity or transit techniques, direct imaging opens up the possibility of collecting light from the planet itself. This provides a window into the planet's atmosphere and surface. Most direct imaging to date has used near-to-mid infrared wavelengths, where the contrast between the thermal emission from the planet and the star is at a minimum, as in Fig. 2. This has its drawbacks: we are so far only able to image young planets that have retained some of the heat from their formation.

Direct imaging can make use of both ground and space based observatories. However, the high spatial resolution required drives the need for a large primary mirror, limiting the possibilities of space-based telescopes. On the other hand, atmospheric turbulence necessitates the use of an adaptive optics equipped facility to observe from the ground. Atmospheric absorption due to telluric lines (absorption lines of Earth's atmosphere) along with the strong background due to thermal emission from the ground and atmosphere also restrict infrared observations to narrow bands.

In addition to the requiring high spatial resolution, it is also challenging to separate the light emitted by the planet from that of the star. Imaging techniques such as Angular Differential Imaging (ADI) (Marois et al., 2006) and Reference Differential Imaging (RDI) (Lafrenière et al., 2009; Soummer et al., 2011) provide methods for reducing the stellar point-spread-function (PSF). Coronagraphs are optical elements which suppress the stellar PSF through self-destructive interference or physical occultation, depending on the position in the optical path. The difference in spectra between the planet and the star can also be used to separate the two sources.

Presently, 10 m class telescopes such as the Very Large Telescope (VLT) in Paranal, Chile or the Gemini Observatory split between Hawaii and Chile provide the best combination of resolution and instrumentation to perform direct imaging of exoplanets. The NACO instrument at the VLT provided the first image of an exoplanet in 2004 (Chauvin et al., 2004). These observatories are among those equipped with an adaptive optics system, coronagraphic instrumentation and near to mid infrared imaging and spectroscopic

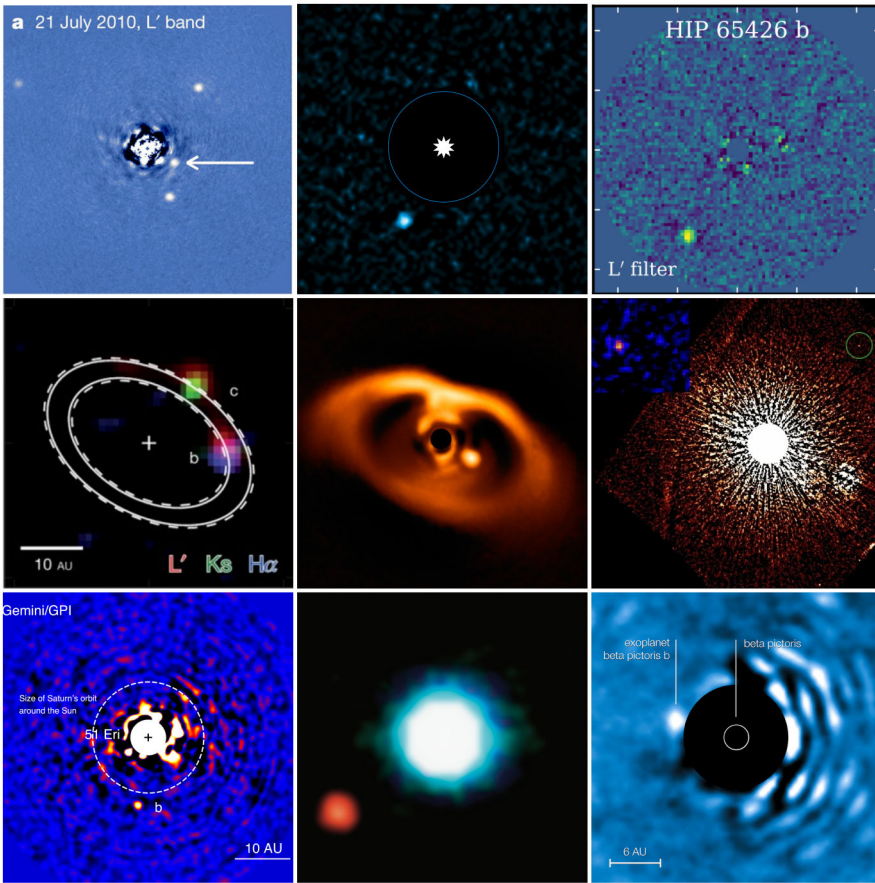


Figure 1: A family portrait of some of the directly imaged exoplanets. In order: (Marois et al., 2010), (Rameau et al., 2013), (Stolker et al., 2020), (Sallum et al., 2015), (Keppler et al., 2018a), (Currie et al., 2012), (Macintosh et al., 2015), (Chauvin et al., 2004), (Quanz et al., 2010).

capabilities to directly image exoplanets, with several exemplar systems becoming standard objects of interest. While it's terribly interesting to explore the details of each of these objects, we will focus our discussion on objects which will be used further in this study due to their scheduled observation as part of the JWST GTO and Early Release Science (ERS) programs (C. A. Beichman et al., 2019c). The parameters of these and other directly imaged exoplanets and brown dwarfs are summarized in table 1.

In order to understand these objects, we must use a measured spectrum in order to infer physical properties. Parameters such as the carbon-to-oxygen (C/O) ratio provide insight into formation mechanisms (Madhusudhan, 2012). A planet that forms near its star will form in a hot region of the circumstellar disk, with a depletion of volatiles due to the high temperature - various species will freeze out at different radii within the disk. The measured C/O ratio of a planet will thus depend on its initial formation location and its migration path. (Turrini et al., 2015) outlines several formation pathways and how the C/O ratio will be affected. The current climate of exoplanets is also of interest. This requires inferences of atmospheric composition and structure from the spectrum, and will ultimately require time resolved measurements in order to study dynamics and variability.

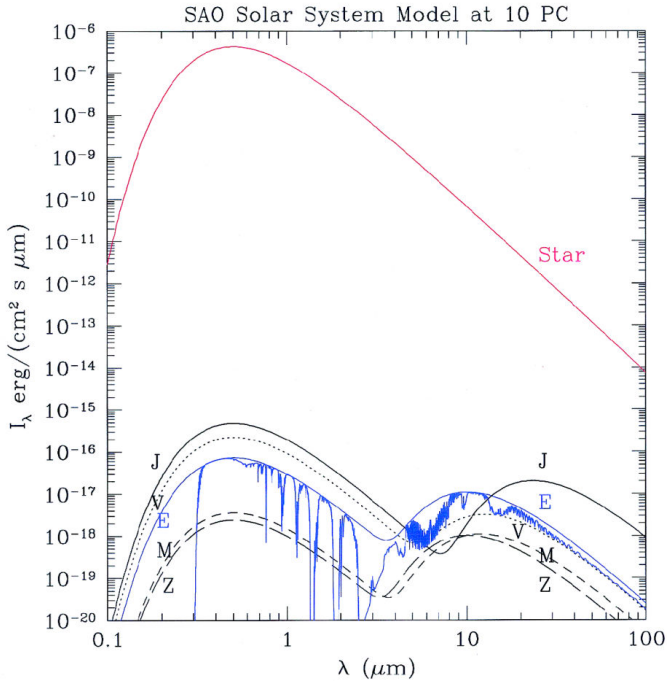


Figure 2: SAO solar system model at 10pc, illustrating the vast difference in luminosity between the Sun and the surrounding planets. However, in the mid infrared the contrast is dramatically reduced at the peak of the planet's emission spectra (Des Marais et al., 2002).

VHS-1256 b

Originally discovered in 2015 (Gauza et al., 2015) as part of the VISTA Hemisphere Survey, VHS-1256b is a late-L dwarf in a 102 AU orbit around an M dwarf. (Gauza et al., 2015) present astrometric, photometric and spectroscopic data on the planet, finding an age of 150-300 Myr from a moving group association, a luminosity $\log(L_{bol}/L_\odot)$ of -5.05 ± 0.22 and infer a mass of $11.2^{+9.2}_{-1.8} M_J$. The effective temperature is found to be 880^{+140}_{-110} K from evolutionary models. This is substantially colder than field dwarfs of a similar spectral type (typically 1400 K), and so it is proposed that a thick Fe and Mg-Si cloud layer acts to reduce the effective temperature. Similar findings are presented by (Rich et al., 2016) using Subaru/IRCS.

In (Miles et al., 2018), methane is detected using KECK/NIRSPEC in the L-band. The shallow depth of the feature indicates chemical disequilibrium in the photosphere, as the derived abundance departs from an equilibrium abundance by a factor of 10-100.

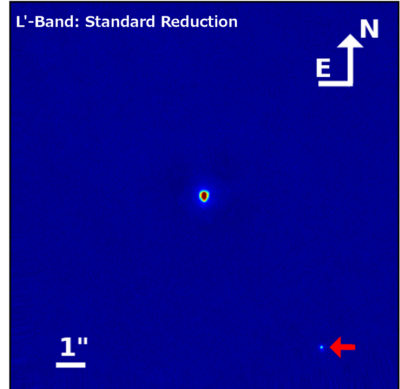


Figure 3: VHS-1256b as observed with Subaru/IRCS in the L'-band (Rich et al., 2016), reduced using the LOCI algorithm (Galicher et al., 2011).

However, the best fit model retrieves substantially different parameters for temperature (1240 K) when compared to previously published results.

The wide separation (8'') and proximity to Earth make VHS-1256b an ideal target for studying atmospheric properties. It will be observed as part of the JWST ERS Program (Hinkley et al., 2019), where a medium resolution spectrum ($R \geq 1700$) will be measured from 0.6-28 micron. This will enable a more precise measurement of the abundance of methane and other species in the atmosphere, and will allow for investigation of the cloud properties in the mid infrared.

2M1207b

Using VLT/NACO, (Chauvin et al., 2004) discovered a low mass companion to the brown dwarf 2MASSWJ 1207334-393254 (2M1207) at a separation of 0.8'', or 55 AU, shown bottom-center in Fig 1. From their H, K and L'-band photometric observations and NIR spectroscopic measurements, 2M1207b was found to have a spectral type of L₅-L_{9.5}, a mass of $5 \pm 2 M_J$ and an effective temperature of 1250 ± 200 K. Follow-up VLT/NACO observations from (Mohanty et al., 2007) found a higher effective temperature of 1600 ± 100 K, and a higher mass of $8 \pm 2 M_J$, pushing it closer to the deuterium burning limit. More recent observations have measured periodic signals due to rotation and variability, but failed to constrain the rotation rate due to pointing variance (Zhou et al., 2019).

(Zhou et al., 2019) also present simulated JWST/NIRCAM observations of 2M1207b. Access to medium resolution spectroscopy in the mid infrared will allow the characterization of cloud condensate properties. The improvement in photometric precision by an order of magnitude will allow better measurement of the rotation rate and variability, and the increase in sensitivity will place lower limits on the possibility of further companions within the system. It will be observed as part of the JWST GTO program (Birkmann et al., 2019).

Name	d [pc]	Mass [M_{\oplus}]	Sep [AU]	Sep ["]	Age [Myr]	$\log(L_{bol}/L_{\odot})$	T_{eff} [K]	References
Widely separated companions								
Close in companions								
VHS 1256b	12.7 ± 1.0	2 ± 1	102	8.1	$10^3 - 10^4$	-5.05 ± 0.22	880	(Gauza et al., 2015)
Fomalhaut b	7.704 ± 0.028	≤ 2	119	13	440 ± 40	...	1600 ± 100	
2M1207b	152.4 ± 1.1	2 ± 1	41	0.8	10 ± 3	-4.68 ± 0.05	1600 ± 100	
51 Eridani b	29.4 ± 0.3	2 ± 1	13	0.45	23 ± 3	-5.06 ± 0.2	700	(Macintosh et al., 2015)
β Pic b	19.3 ± 0.2	2 ± 1	9	0.4	23 ± 3	-3.78 ± 0.03	1600 ± 100	(Quanz et al., 2010)
GJ 504b	17.56 ± 0.08	3 – 30	44	2.5	$100 - 6500$	-6.13 ± 0.03	544	(Skemer et al., 2016a)
HD 95086b	90.4 ± 3.3	5 ± 2	56	0.6	17 ± 4	-4.96 ± 0.10	1050	(De Rosa et al., 2016)
HR8799b	39.4 ± 1.0	5 ± 1	68	1.7	40 ± 5	-5.1 ± 0.1	870^{+30}_{-70}	(Marois et al., 2008; Skemer et al., 2012)
HR8799c	39.4 ± 1.0	7 ± 2	38	0.95	40 ± 5	-4.7 ± 0.1	1090^{+10}_{-90}	(Marois et al., 2008; Skemer et al., 2012)
HR8799d	39.4 ± 1.0	7 ± 2	24	0.62	40 ± 5	-4.7 ± 0.2	1090^{+10}_{-90}	(Marois et al., 2008; Skemer et al., 2012)
HR8799e	39.4 ± 1.0	7 ± 2	14	0.38	40 ± 5	-4.7 ± 0.2	1000	(Marois et al., 2008; Skemer et al., 2012)
LkCa 15b	145 ± 15	6 ± 4	20	0.08	2 ± 1	
PDS 70b	113.43 ± 0.52	7 ± 2	23	0.19	5 ± 1	...	900	(Haffert et al., 2019)
PDS 70c	113.43 ± 0.52	4.4 ± 1	30	0.24	5 ± 1	...	10^4	(Haffert et al., 2019)
Nearby Brown Dwarfs								
WISE 0855	2.2 ± 0.2	3 – 10	$10^3 - 10^4$	-10.5	225 – 260	(Luhman, 2014; Tinney et al., 2014)
Luhman 16B	1.998 ± 0.0004	28.6 ± 0.3	$600 - 800$	-4.68	1201	(Sahlmann and Lazzorenko, 2015); (Garcia et al., 2017)

Table 1: Summary of directly imaged planet and brown dwarf parameters based on (Bowler, 2016) and references therein. Luminosity for WISE 0855 is calculated in H band.

1.2 BROWN DWARFS

Brown dwarfs are the low mass result of a failed star formation process. On the low end of the mass scale, an object is considered a brown dwarf at $>13M_J$, which is the deuterium burning limit. Recent observations of low mass ($1 M_J$), free floating observations have led to challenges of this definition defining the boundaries between planets and brown dwarfs. By $75 M_J$, the object is heavy enough to sustain hydrogen fusion and the object is considered a star. However, there have recently been observations of even lower mass brown dwarfs, down to several Jupiter masses, raising questions of formation processes (Luhman, 2014). It is generally thought that brown dwarfs form during the gravitational collapse of a molecular cloud, while exoplanets form through a core accretion process in a circumstellar disk. Observations of high mass companions and low mass field objects then challenge these standard models.

While brown dwarfs are objects of scientific interest in their own right, we are particularly interested in their use as analogs for exoplanets due to their similar temperatures and pressures. Without the issue of contrast between an exoplanet and its host star, brown dwarfs are ideal targets for medium and high resolution spectroscopic characterization. As shown in table 1, they are also some of the closest known objects to the solar system, with several having been observed at around 2 pc.

1.2.1 Observational Properties

Brown dwarfs are characterized by their spectral type, either by comparison to spectral templates, using indices derived from spectral parameters or through broadband photometric comparison (Helling and Casewell, 2014). Directly imaged exoplanets can also be classified using brown dwarf spectral types. Unlike stars which maintain their temperature and luminosity through fusion, brown dwarfs cool and change their spectral type with age, leading to a degeneracy between mass and age (Burrows et al., 2001). This spectral series is shown in Fig. 4.

As a brown dwarf cools and contracts over time, its surface gravity will increase, leading to the use of $\log(g)$ as a tracer of age (Manjavacas, 2014). Young, low surface gravity objects are particularly comparable to directly imaged exoplanets. In these young objects, clouds are a nearly universal feature (Cooper et al., 2003; Helling and Casewell, 2014), with thicker cloud decks appearing in low gravity objects (Helling and Casewell, 2014).

L-Type

L-dwarfs are the hottest brown dwarfs, with typical effective temperatures between 1300 K and 2100 K (Burrows et al., 2001). L-type spectra are notable for the disappearance of VO and TiO NIR absorption lines and the onset of molecular absorption features such as H_2O and CO, with CH₄ appearing in late L-types (Manjavacas, 2014). Further key features of L-dwarfs is the formation of iron and silicate condensate, as well as the growth of neutral alkali lines (Burrows et al., 2001).

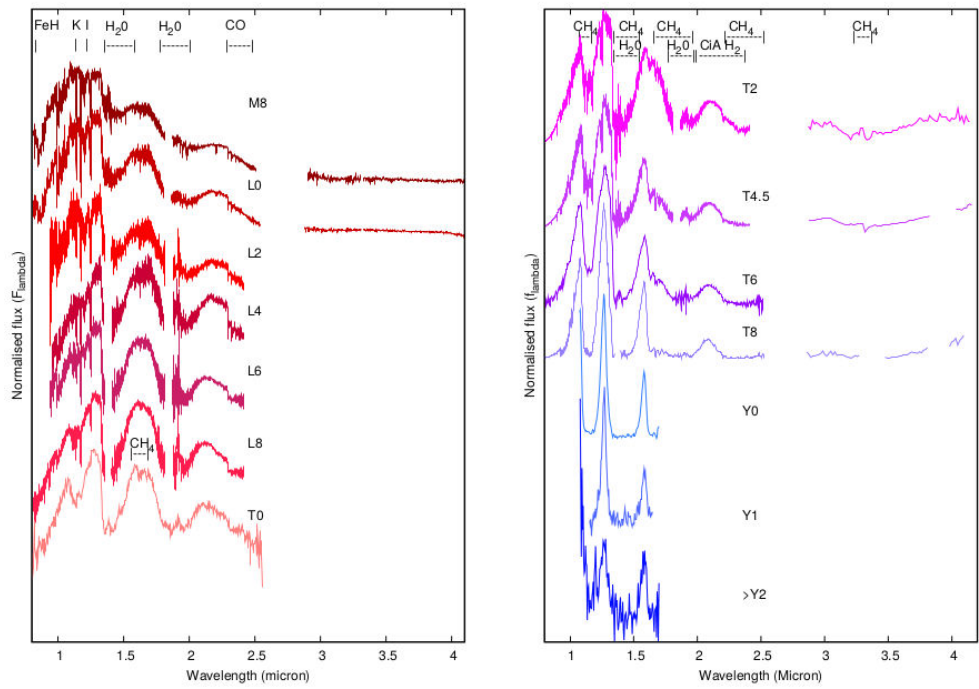


Figure 4: Near Infrared spectral series of brown dwarfs from early-M to early-Y as shown in (Helling and Casewell, 2014).

T-Type

As a brown dwarf ages it moves towards a T-type spectrum. The L/T transition occurs with the appearance of both CH₄ and CO absorption, and is characterized by increasingly blue J-H colour as the temperature decreases. There are several proposed mechanisms for this transition, with cloud fragmentation due to particle microphysics (Burningham et al., 2017) and convection processes being two examples (Tremblin et al., 2015). Both T- and L-dwarfs are highly variable due to complex atmospheric dynamics ranging from clouds to banding structures to hot spots and more (B. Biller, 2017). (Vos et al., 2019) presents how monitoring with JWST/MIRI will be able to constrain the mechanism behind this transition.

Y-Type

Y-type dwarfs are ultra-cool objects first discovered in (Cushing et al., 2011). With such cold temperatures, they contain deeper water and methane absorption features than present in T-dwarfs, and likely contain ammonia as well. Atmospheric models suggest typical temperatures between 300-500 K, which places them as the coldest detected and spectroscopically measured brown dwarfs to date (Cushing et al., 2011). Due to the very low temperatures of Y-dwarfs, mid-infrared observations are ideal for detection and characterization. Most spectral features of interest (CH₄, NH₃, etc) will be present at longer wavelengths, while the mid infrared will also present opportunities for measurements of cloud properties and composition.

WISE 0855-0714

WISE-0855 is the coldest known brown dwarf at 250 K, with an inferred mass of $5 M_J$ (Luhman, 2014), and a Y2-4 spectral type (Leggett et al., 2015). Although faint, with a J-band magnitude of 25, its proximity to the sun makes allows for its spectral characterization. Present measurements indicate the presence of ammonia (Leggett et al., 2015) and water clouds (Faherty et al., 2018; Morley et al., 2014) in its atmosphere.

WISE 0855, along with other Y-dwarfs will be the subject of JWST investigation (Oliveira, 2015; Oliveira et al., 2019). Its low mass and cold temperature make it the closest analog to solar system objects, especially to Jupiter. Further observations will allow for tighter constraints on atmospheric composition and cloud properties, as well as insight into whether such objects are the result of a star-like formation process or are an ejected, free floating planet (C. Beichman et al., 2014).

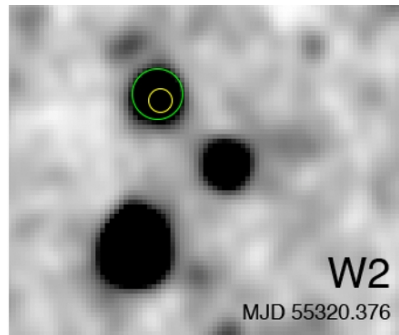


Figure 5: W₂, epoch 1 image of WISE0855 on top of a known background clump. The green circle represents the location of WISE0855, the yellow is the position of the background source (E. L. Wright et al., 2014).

1.3 MOTIVATION

1.3.1 Current Status of Atmospheric Characterization

Both exoplanets and brown dwarfs raise interesting questions with regards to atmospheric properties, but there are substantial challenges both in gathering the data necessary to answer them and modeling the physics underlying the observable parameters. The best methods currently in use involve taking spectroscopic data and inferring atmospheric properties from the spectral features. The light we measure may be thermal emission from the planet, where it is absorbed and scattered as it passes through the planet's atmosphere, or it may be light from the planet's host star which passes through the upper layers of the atmosphere. These provide complementary information about the composition and structure of the atmosphere, probing different altitudes and pressures. While a more complete overview of exoplanet atmospheres is covered in the literature, e.g. (Madhusudhan et al., 2014; Seager and Deming, 2010; Sing et al., 2018), we will briefly summarize the current methods used and what has been learned so far.

Transmission Spectroscopy

Many exoplanets have been discovered using the transit technique in which the planet passes in front of its host star, blocking a small fraction of its light. Through time series observations, particularly with satellites such as Hub-

ble, Kepler, and TESS, we can observe this dip in stellar brightness, and infer properties of the planet. A key feature of this observation is that in the case the planet has an atmosphere, the brightness dip is wavelength dependent. Depending on the wavelength, different species within the atmosphere will absorb the light to a greater or lesser extent. Thus if a species is abundant within the atmosphere, it will create deep absorption features, which will make the apparent radius of the planet larger, increasing the transit depth. Measuring this radius variation is the procedure of transmission spectroscopy, and is used to probe the composition and structure of the upper atmospheres of transiting planets. In addition to transmission spectroscopy, secondary eclipse spectroscopy is another transit measurement that uses the reflected light and thermal emission of the planet, and measures the dip in total luminosity as the planet passes behind its host star. This provides a more direct measurement of the planet's reflection or emission spectrum. (Kreidberg, 2018) presents a concise overview of transmission and eclipse spectroscopy.

Transmission spectroscopy attempts to answer questions about atmospheric composition, formation history and present climate. To date, water features and carbon-bearing molecules have been detected, though molecules commonly present in the solar system such as methane and ammonia have not been detected, largely due to lack of long wavelength coverage and the high temperatures of most transiting planets (Kreidberg, 2018; Lee et al., 2012). The C/O ratio has been measured in some hot Jupiters, including WASP-12b, which provides a trace for formation history and current composition (Madhusudhan et al., 2011). For WASP-12b, the high C/O ratio (>1) and the lack of an observed thermal inversion in the highly irradiated atmosphere both stand in contrast to theoretical predictions, and demonstrate the necessity for improvements in atmospheric and formation modeling (Madhusudhan et al., 2011). In other atmospheres, nitrogen chemistry has been observed, and condensates (clouds and hazes) are nearly universal (MacDonald and Madhusudhan, 2017). Water has been detected on hot Jupiters (Kreidberg et al., 2014), as well as on smaller planets within the 'habitable zone' (Benneke et al., 2019; Tsiaras et al., 2019).

Future observations will increase the spectral resolution of transit observations, and will also extend the wavelength coverage. By probing the mid infrared, it may be possible to determine the composition of the clouds observed, and place tighter constraints of the abundances of species present within atmospheres (Kreidberg, 2018).

Emission Spectroscopy

In contrast to transit observations, emission spectroscopy is a direct measurement of the light emitted by the planet, usually in the infrared, where the planet's luminosity peaks due to Wein's law. Due to the low levels of flux emitted from most planets, most emission spectroscopy to date has been low to medium resolution, in order to collect enough light for measurement. However, this has already allowed us to begin to answer similar questions as posed for transmission spectroscopy. What are these atmospheres made of? How did these planets form? In many ways though, emission and transmis-

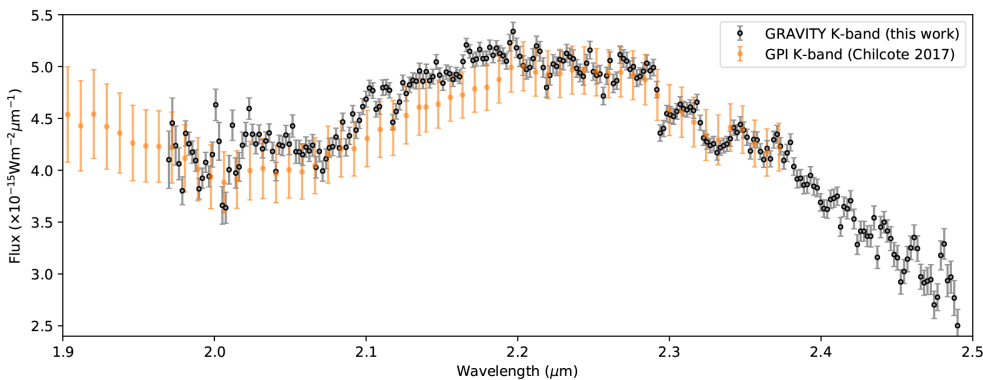


Figure 6: Flux calibrated K-Band emission spectrum of β Pic b as measured using the VLTI/GRAVITY at $R=500$ (GRAVITY Collaboration et al., 2020), along with the GPI K-Band spectrum from (Chilcote et al., 2017).

sion spectroscopy provide complementary information, and multiple ways of approaching these problems. Due to the different wavelength regimes, they are able to identify different species and probe different atmospheric depths.

Only recently has high quality exoplanet emission spectroscopy become possible, and a comprehensive overview is provided in (B. A. Biller and Bonnefoy, 2018). Measurements of H α emission in LkCa 15b have allowed for inferences of the mass accretion rate of a forming planet (Sallum et al., 2015), while observations of the PDS 70 system indicate the presence of a circumplanetary disk around PDS 70b (Christiaens et al., 2019; Keppler et al., 2018a). With integrated field spectroscopy, (Hoeijmakers et al., 2018) show how spectroscopy can identify the presence of molecular species in a spectrum and how this can be used to discover companions within the contrast-limited regime. Using the VLTI/GRAVITY instrument, which combines light from all four Unit Telescopes (UTs) of the VLT into a single interferometer, medium resolution ($R=500$) spectra have been taken of HR 8799e (Lacour et al., 2019) and β Pic b (GRAVITY Collaboration et al., 2020), the latter of which is shown in Fig. 6. These spectra represent some of the best data available to date for exoplanets, and additional observations of well-known directly imaged planets are planned in the near future. With such spectra, atmospheric retrievals are used to infer properties of interest using Bayesian inference, fitting parameterized 1D atmospheric models to the spectrum in order to find the most likely value of those parameters (Madhusudhan and Seager, 2009). While not yet accomplished for an exoplanet, it may be possible in the near future to longitudinally map cloud features of exoplanets, as has already been accomplished for brown dwarfs using the CRIRES instrument (Crossfield et al., 2014).

As most older planets will emit primarily in the thermal infrared, JWST/MIRI will provide unprecedented capabilities at imaging and characterizing these systems. (Danielski et al., 2018) shows that the MIRI Low Resolution Spectrometer will allow for the detection of ammonia in the coldest targets, as well as characterize the abundances of other molecules such as CH $_4$, H $_2$ O, CO $_2$ and PH $_3$. Many direct imaging observations of exoplanets

have been proposed as part of the JWST GTO and ERS programs. In a white paper, (C. A. Beichman et al., 2019c) discuss how JWST will provide new insight into exoplanet atmospheres using direct emission imaging and spectroscopy, while (Line et al., 2019) examines the possibility of characterizing terrestrial planets using thermal emission spectroscopy.

1.3.2 JWST Studies

With the launch of JWST imminent, many proposals have been made to cover a wide range of science cases, as well as performing instrumental testing, calibration and validation. Exoplanet science is well represented within these first observations, and several of the proposals will be presented here.

Early Release Science

The Early Release Science program is an initiative designed to help scientists develop an understanding of the instruments available on JWST, as well as the tools needed to process the data. Thus the ERS provides an extensive catalog of public data immediately upon observation, and will take place within the first 5 months of JWST science operations. Both a transiting program (Bean et al., 2018) and a direct imaging program (Hinkley et al., 2019) have been approved. The direct imaging proposal has 52 hours observing time in order to take data using the full range of JWST instrumentation and observing modes. The goal is to image a representative sample of known directly imaged planets, in order to develop the tools and techniques necessary to push the limits of the instrumentation. For a subset of the imaged planets, including VHS-1256b, spectroscopic data covering the full wavelength range of JWST will be taken using a combination of the available instruments.

GTO Programs

In addition to the ERS program, the Guaranteed Time Observations (GTO) program is designed to provide scientists who helped in the development of JWST hardware and software with a set amount of observing time. Many GTO programs focused on exoplanet science have been approved, including spectroscopic studies of 2M1207b and other commonly studied systems (Birkmann et al., 2019). Brown dwarf science is also well represented within the GTO program, with WISE-0855 receiving full spectroscopic coverage from 0.6-28 μm (Oliveira et al., 2019). Details of the observations for VHS-1256b, 2M1207b and WISE-0855 are discussed in 4.3.

1.3.3 Biosignatures and Future Missions

While JWST will provide higher spectral and spatial resolution in the infrared than any previous observatory, many questions will remain open for future missions. One of the ultimate unanswered questions in science is "Are we alone?". The detection of biosignatures in the near future with next generation 40 m class telescopes (López-Morales et al., 2019) or proposed space missions such as LIFE (Quanz et al., 2019) and LUVOIR (LUVOIR Mission

Concept Study Team, 2019) may provide our best chance at answering such questions. Instruments such as METIS on the ELT will offer high resolution ($R=100000$) integral field spectroscopy of nearby terrestrial planets, while both proposed space missions will have the spatial and spectral resolution necessary to characterize a nearby earth like planet. With such a goal in mind, it is necessary to develop the technical capabilities in both theory and observation order to achieve such ambitious goals in the not-so-distant future.

1.4 THESIS OVERVIEW

With sufficient background and motivation, we will now outline the remainder of this thesis.

Chapter 2 will provide a more extensive background of the James Webb Space Telescope, and in particular the MIRI Medium Resolution Spectrometer (MRS). We will outline the principle optical components dedicated to integral field spectroscopy, as well as the detector characteristics of MIRI. This will provide the necessary background to understand the instrumental and optical effects discussed in Chapter 3.

The third chapter examines the fringing effect in the MIRI MRS instrument. We discuss the optical effects that result in fringing patterns, as well as outlining current and future strategies for fringe correction. We describe the creation and processing of our mock observations using the MIRI instrumental simulator and the JWST data reduction pipeline. With the degraded spectra from the simulated data, we measure the impact of fringing on spectral extraction using cross correlation techniques, and how this impacts molecular mapping studies. This in turn motivates Chapter 4, where the species identified using molecular mapping can justify the inclusion or exclusion of particular species in an atmospheric retrieval.

In Chapter 4 we explore atmospheric retrievals with the MIRI MRS. We outline our procedure for performing a retrieval using the petitRADTRANS radiative transfer code and Multinest as an implementation of the nested sampling strategy for parameter space exploration. We measure the impact of fringing on parameter estimation, and also investigate how observing parameters will impact retrievals, discussing the advantages and challenges of studying atmospheres in the mid infrared.

Finally we summarize and discuss our findings and future investigations in Chapter 5.

2

MIRI: THE MID-INFRARED INSTRUMENT

MIRI is an instrument that will provide unique capabilities for studying exoplanets and other cold and distant objects. This chapter will provide a detailed overview of the technical details and capabilities of the instrument. A complete description of MIRI is provided in a series of papers from (Boccaletti et al., 2015; Bouchet et al., 2015; Glasse et al., 2015; P. Lagage et al., 2015; Ressler et al., 2015; Rieke et al., 2015a,c; Wells et al., 2015; G. S. Wright et al., 2015).

2.1 THE JAMES WEBB SPACE TELESCOPE

JWST is a 6.5 m space based observatory built in collaboration between NASA, ESA and CSA that will be located in a halo orbit at the L2 Earth-Sun Lagrange point. As the successor to the Hubble Space Telescope and the Spitzer Space Telescope, it will provide a new perspective for infrared astronomy. It is currently scheduled to launch in March 2021.

James Webb is fully optimized for infrared astronomy. To reduce instrumental thermal background, the entire telescope will operate at cryogenic temperatures. A large sun-shield will help block solar infrared radiation. The lightweight beryllium mirrors are coated in gold to maximize reflectivity out to the mid-infrared.

Of key interest to exoplanet science is the both the sensitivity and spatial resolution of the instrument. With its 6.5 m primary, JWST will have a spatial resolution from 0.01" at 0.6 micron to 0.92" at 29 micron. The increase in sensitivity is due in part to the larger collecting area, but also to advances in detector technology since the previous generation of infrared observatories. For example, the MIRI instrument will have a minimum detectable flux of 0.13 μ Jy at 5.6 micron and a 10 000 second integration, or roughly a factor of 1000 better than what was possible with the Spitzer Space Telescope (Glasse et al., 2015).

There are four primary instruments that constitute the Integrated Science Instrument Module (ISIM). Near-Infrared Camera (NIRCam), which provides imaging with coronagraphic capabilities from 0.6-5 micron. The Near-Infrared Spectrograph (NIRSpec) provides fixed slit and integrated field unit spectroscopy capable of analyzing multiple objects simultaneously, and operates in the same wavelength range as NIRCam. The Fine Guidance Sensor/ Near-Infrared Imager and Slitless Spectrograph (FGS/NIRISS) allows for low and medium resolution spectroscopy with high photometric stability, as well as aperture masking interferometry. The final instrument, MIRI, is the subject of this thesis.



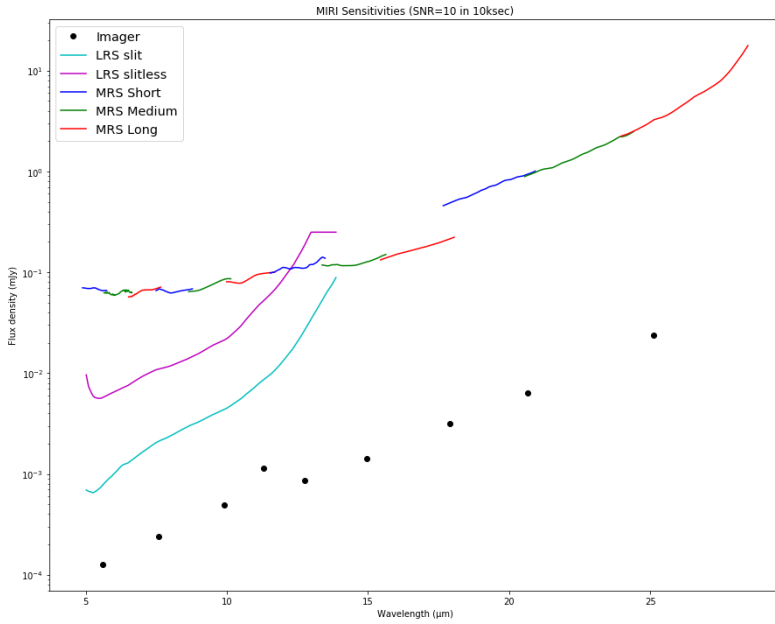
Figure 7: The James Webb Space Telescope during integration of the telescope into the Spacecraft Element (Gunn, 2019).

Subsystem	λ Range [μm]	Px Scale ["/px]	$\Delta\lambda/\lambda$
Imaging	5-28	0.11	3.5-16.1
4QPM Coronagraphic Imaging	10.65, 11.4, 15.5	0.11	14.1-17.2
Lyot Coronagraphic Imaging	23	0.11	4.1
Low Resolution Spectroscopy	5-12	0.11	100 @ $7.5\mu\text{m}$
Medium Resolution Spectroscopy	4.9-28.8	0.196-0.273	1550-3300

Table 2: Summary of MIRI observing modes.

2.2 MIRI

The Mid-Infrared Instrument (MIRI) provides imaging, fixed slit and integrated field spectroscopy between 4.8 and 28 micron (G. S. Wright et al., 2015). These sub-instruments are enclosed in a closed-cycle cooler to maintain a temperature of 6.7 K in order to reduce the thermal background. At its most sensitive, MIRI is about $1000\times$ more sensitive than comparable instrumentation on Spitzer. Sub-instrument sensitivities are shown in Fig. 8. While this will prove tremendously valuable for exoplanet science, it will also allow exploration of star formation, extra galactic astronomy and high-redshift observations. These and further science cases are described in (Rieke et al., 2015a). In its imaging mode, MIRI can operate with either a Lyot or 4-Quadrant-Phase-Mask coronagraph to reduce stellar glare, the MRS is not equipped with such an element. Thus its use for exoplanet observations is restricted to highly separated or bright targets. It may also be possible to use the differences between the host star and companion spectra in order to image close in planets.



2.3 THE MEDIUM RESOLUTION SPECTROGRAPH

The Medium Resolution Spectrograph (MRS) consists of four integrated field spectrographs projected onto two detectors, covering 4.8-28 micron with a spectral resolution varying from $R=1700$ to $R=3500$. Its FoV ranges from $4'' \times 4''$ to $7.7'' \times 7.7''$. While a full description of the MRS is given in (Wells et al., 2015), in this section we will outline the optical design of the instrument.

2.3.1 Coordinates

There are three primary coordinate systems in use with JWST/MIRI-MRS, of which two will be relevant for this thesis, with the detector and local MRS coordinates described in Fig. 9 (Argyriou et al., 2020).

The detector coordinate grid is formed by counting x/y pixels, as well as the slice number. Each of the two MRS detectors is an array of 1032×1024 pixels, though only 1024 are photosensitive in the horizontal direction. Each image slice from the IFU appears as a curved stripe on the detector, though neighbouring stripes on the detector do not correspond to neighbouring slices of the image.

The local MRS coordinate system is described in terms of α, β and λ . The continuous α coordinate is the along slice direction, while β is perpendicular and discrete, corresponding to the slice number. λ is the wavelength. Both α and λ are fit by a third order polynomial to account for along and across slice distortion (Wells et al., 2015). Each detector sub array has its own mapping to α, β, λ space, due to the differences in FoV, slice count, distortion and spectral resolution.

Channel	Sub-band	Band	Detector	λ Range [μm]	FoV [as]	$\lambda/\Delta\lambda$
1	Short	1A	SW	4.83 - 5.82	3.46×3.72	3500
	Medium	1B		5.62 - 6.73	3.46×3.72	3500
	Long	1C		6.46 - 7.76	3.41×3.72	3300
2	Short	2A	SW	7.44 - 8.90	4.16×4.76	3000
	Medium	2B		8.61 - 10.28	4.16×4.76	3000
	Long	2C		9.94 - 11.87	4.12×4.76	3000
3	Short	3A	LW	11.47 - 13.67	6.00×6.24	2700
	Medium	3B		13.25 - 15.80	5.96×6.24	2300
	Long	3C		15.30 - 18.24	5.91×6.24	2300
4	Short	3A	LW	17.54 - 21.10	7.14×7.87	1700
	Medium	3B		20.44 - 24.72	7.06×7.06	1700
	Long	3C		23.84 - 28.82	6.99×7.87	1500

Table 3: Properties of the MIRI MRS channels (Wells et al., 2015).

The third coordinate frame is the global coordinate system of JWST itself, V₁,V₂,V₃. The V₁ coordinate refers to the symmetry axis of the telescope, V₃ points towards the foldable secondary mirror support structure strut. V₂ completes the coordinate system, being orthogonal to V₁ and V₃. This coordinate system will not be used in this thesis.

2.3.2 Integral Field Spectroscopy

As an integrated field spectrograph (IFS) consisting of 4 integrated field units (IFUs), the MRS provides both spatial and spectral information. This is accomplished by slicing the on sky image, and performing spectroscopy on each of the image slices. Here we will step through some of the key optical systems used to accomplish this, while a more detailed description of the optics is given in section 2 of (Wells et al., 2015).

A series of optics picks off a FoV from the telescope beam, and directs it to the IFU slicing mirrors, where the focal plane is re-imaged. The image slicer consists of an array of thin mirrors at unique angles, in order to separate different spatial slices of the on-sky image. The across slice width is equal to the FWHM of the Airy pattern at the shortest wavelength of the given IFU. There are a total of 4 image slicers, one for each of the MRS channels. Each slice is then collimated, and directed to a diffraction grating. Each channel has 3 separate gratings, each covering approximately a third of the wavelength range of each channel. Thus it requires 3 total exposures to cover the wavelength range of a channel. Channels 1 and 2 are each projected onto separate halves of a single detector, as are channels 3 and 4 as seen in Fig. 10. When reconstructed, the PSF is an

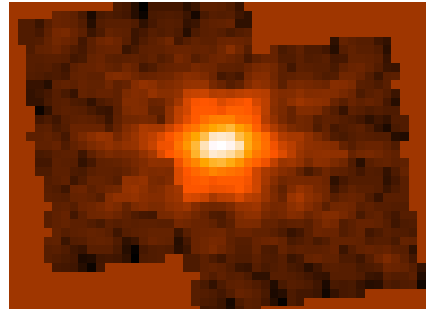


Figure 11: The reconstructed JWST PSF as imaged by the MRS, using a 2-pattern dither.

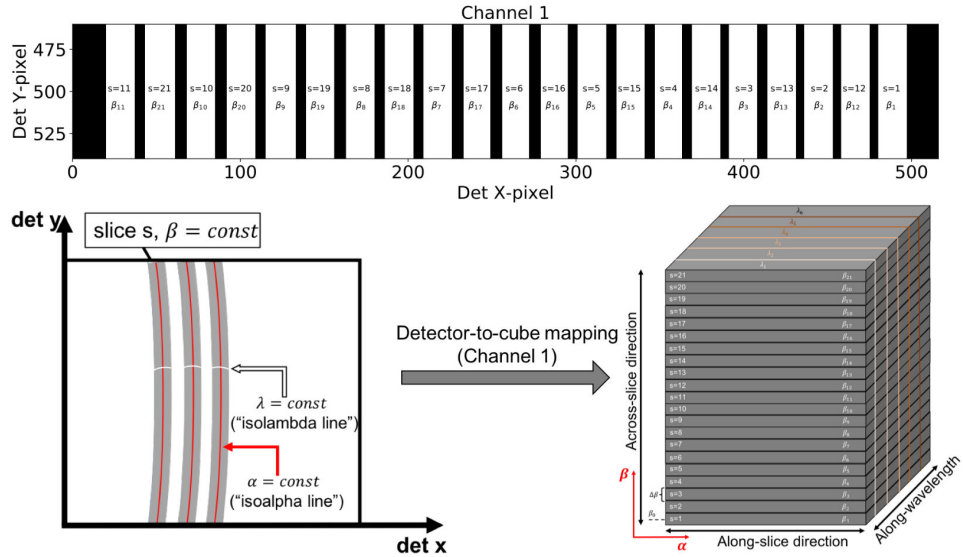


Figure 9: Description of the MRS detector (x, y, s) coordinate system to the local MRS (α, β, λ) cube coordinates. **Top:** Detector coordinates. Note that the consecutive stripe numbers s_i, s_{i+1} correspond to neighbouring image slices. **Bottom:** Description of the (invertible) detector-to-cube transformation (Argyriou et al., 2020).

undersampled image of the JWST PSF, though dithering can be used to improve the spatial sampling. As such, multiple wavelength ranges are imaged simultaneously, and it requires only 3 exposures in order to cover the entire MRS wavelength range.

2.3.3 Detectors

MIRI uses three arsenic-doped silicon (Si:As) impurity band conduction (IBC) detectors descended from those used in the Spitzer Space Telescope. Each detector uses a 1024×1024 pixel format. One detector is used for the imaging and LRS modes, while the remaining two detectors are used in the MRS. The full technical details of the detectors are described in (Rieke et al., 2015c).

Si:As IBC detectors are ideal for mid-infrared measurements. Each detector is built onto a high resistivity transparent contact. A 25–35 micron thick, heavily arsenic-doped layer acts as the absorption layer, with an electric field maintained across the layer in order to transport the generated photoelectron. A transparent contact layer provides a connection to the detector electronics, where the signal is amplified and read out. A schematic of the layers in the detector is provided in the context of the fringing effect in Fig. 13. These detectors have a quantum efficiency that is wavelength dependent, and provides a fundamental limitation on the sensitivity. Precise measurement of this photon-to-electron conversion efficiency is critical for photometrically calibrating observations. The efficiencies are shown for each sub-band of the MRS detectors in Fig. 12.

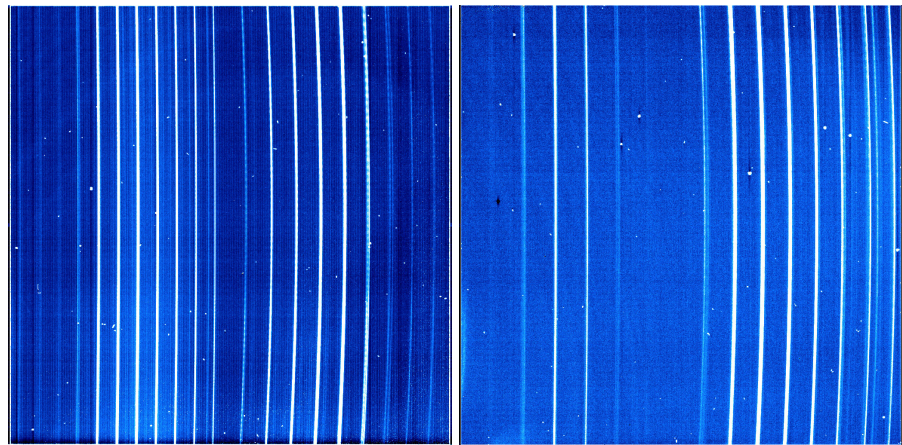


Figure 10: Level 2 detector images of the FM calibration source for channels 1 and 2 (left), channels 3 and 4 (right) - note that channel 4 is on the left half of the long wavelength detector, and displays significantly lower sensitivity compared to the other 3 channels.

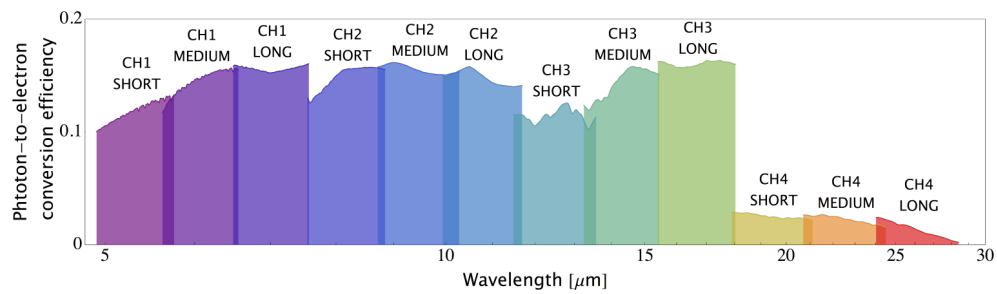


Figure 12: Average photon-to-electron conversion efficiencies for the MIRI MRS detectors.

Readout Modes

The MRS has two primary readout modes, which can be selected for different observing strategies.

- FAST - A 2.78 s integration with a single sample per pixel. Higher noise, but more suited for bright targets.
- SLOW - a 24 s integration, with 9 samples per pixel. A lower noise mode, but can saturate on bright sources.

2.4 OBSERVATIONS

The observations in this work are based on proposed exoplanet observations for the ERS and GTO programs. The observing parameters have been checked using the JWST Exposure Time Calculator in order to ensure sufficient SNR. Several of the observations make use of a dithering procedure, described below.

2.4.1 Dithering

The MIRI PSF is spatially undersampled in the MRS in order to allow for wider wavelength coverage and increased throughput. This design choice was made in order to reduce the weight of components that would be necessary in order to provide a fully sampled PSF while meeting the spectroscopic requirements. In order to fully sample the PSF, observations are dithered: that is, multiple telescope pointings are used, and the exposures from each pointing combined into a single observation. An optimal dithering strategy for each channel has been designed in order to fully sample the PSF in a minimum of observations. For a point source, it will be typical to use a 2 or 4 point dither pattern.

2.4.2 Exposure time calculations

The JWST Exposure time calculator (ETC) is a publicly available tool that can be used to estimate outcomes of a given set of observational parameters on a specified target. This can be used to estimate the SNR in different wavelength bands, optimize observing and check for detector saturation. All observations in this work were checked using the ETC in order to prevent saturation and ensure sufficient SNR. However, we did not attempt to optimize the observing strategy for our targets, and instead used the parameters specified in the ERS and GTO observing proposals.

3

FRINGING EFFECTS IN MIRI

Understanding optical and instrumental effects is critical for creating accurate simulated observations and for characterizing systematics. These systematics and uncertainties in turn impact the potential science results from any instrument by biasing measurements, reducing the signal to noise ratio of measurements or by injecting non-physical signals and correlations. The aim of this chapter is to examine fringing in the MIRI detectors and how this effect is modeled in the instrumental simulator (MIRISIM). We will examine the current status of fringe modeling and correction before discussing the modifications made to the MIRI instrumental simulator in order to model point source fringing effects.

In order to quantify the effect of fringing on a spectrum, we examine the effect of fringing on a cross correlation between the extracted spectrum from the instrument and a known template. This provides a measure of the extent to which the signal has been degraded. In addition we examine the impact of this on the science case of molecular mapping, where cross correlations between a cube of IFU data and a molecular spectral template are used to identify the presence of a given species in an observed object.

3.1 FRINGING

Thin film interference occurs when light is coherently reflected at the internal boundaries between two layers and interferes with the incident light. This is the principle on which Fabry-Pérot interferometers function. As we wish to determine the effect of fringing on the amplitude of the signal received by the detector as a function of wavelength, we are effectively interested in the transmittance of a series of Fabry-Pérot interferometers. Assuming an ideal plane-parallel optical cavity with a reflectance R at both boundaries, thickness D , and an angle θ at which the light enters the cavity, we can compute the transmittance as:

$$T_c = \frac{1}{1 + \frac{4R}{(1-R)^2} \sin^2\left(\frac{\delta}{2}\right)}. \quad (1)$$

Where the phase δ at half a wavelength ($\phi = \pi$), with wavenumber σ is:

$$\delta = 4\pi\sigma D \cos\theta - (\phi - \pi). \quad (2)$$

Systems with a spacing on the order of micrometers to millimeters produces significant interference for infrared light (Lahuis and Boogert, 2003).

The detectors of the MRS consist of several layers, as shown in Fig. 13, with a characteristic thickness of tens of micron, which results in significant (10%-30%) ‘fringing’ in a spectrally flat signal - visible in Fig. 10. The geometric thicknesses of the detector layers are given in table 4.

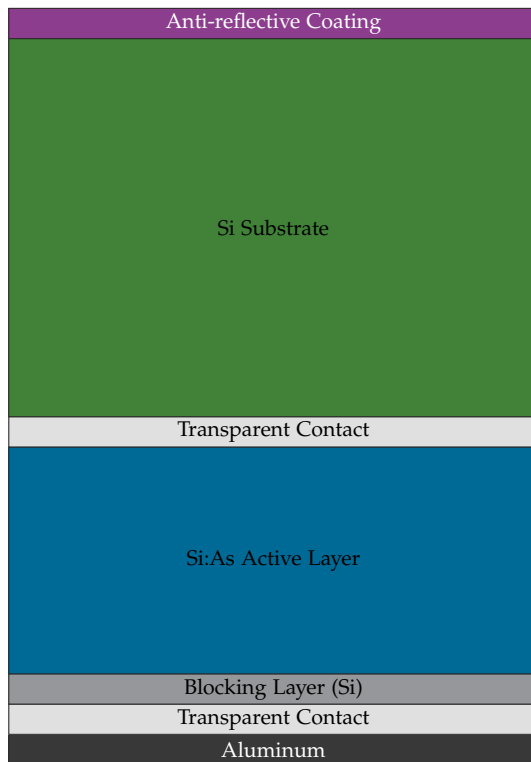


Figure 13: Layers of the MIRI MRS detectors. Note that thicknesses are not to scale (Rieke et al., 2015c).

While this is typical for infrared detectors such as those in the Spitzer Space Telescope (Lahuis and Boogert, 2003) or in the Space Telescope Imaging Spectrograph on board HST (Malumuth et al., 2003), the sensitivity and spectral resolution of the MRS increases the significance of this issue. The MIRI consortium has stated that the error budget for all detector effects must be 3.3% or less. Present fringing corrections result in a 5% deviation from a photometrically accurate signal, and can introduce correlated noise which will degrade any measured spectrum. Therefore it is critical to examine the impact of fringing on a signal, the parameters that influence the fringing strength and phase, and possible solutions for fringe correction. If all of the geometric and optical parameters were known, this would be sufficient to numerically solve for the fringing pattern within MIRI using eqn 1. Unfortunately, uncertainties in the thickness in the detector layers, variations in the layer deposition thickness, and the uncertainty of transmittance and reflectance of the materials used at cryogenic temperatures prevents the implementation of such a numerical model. Instead, we will turn to calibration data taken to empirically characterize the fringing pattern.

While a more complete treatment of proposed fringe correction can be found in (Argyriou et al., 2020) and (Lahuis and Muller, 2018), this work will examine the implementation of fringing into the MIRI instrumental simulator and address the current state of fringe correction in the JWST Data Calibration Pipeline. We will discuss the architecture and usage of MIRISIM, along with the modifications we have made in order to model point source fringing.

Layer	Material	Depth [μm]	Comments
Anti-Reflection Coating	ZnS	0.66	Optimized for $\lambda = 6 \mu\text{m}$.
Substrate (raw wafer)	Si	460	Inactive layer.
Bottom Transparent contact	?	?	Not transparent, negative applied bias voltage.
Active layer	Si:As	35	Photoelectric absorption layer.
Blocking layer	Si	4	Inactive layer.
Top transparent contact	?	?	Not transparent. Positive applied bias voltage.
Pixel metalization	Al	semi-infinite	Forms metallized electrical contact with top transparent layer.

Table 4: Detector layer compositions and mean geometric thicknesses.

3.1.1 Current Status of Fringing Correction

Three test campaigns have been run in order to characterize MIRI: the Flight Model (FM) in 2008-09, the Cryogenic Vacuum (CV) in 2015-16, and the Optical Telescope element/ Integrated Science (OTIS) tests in 2017. Fringing was a major subject of both the FM and CV campaigns. The first fringe model is fit to a spectrally flat, spatially extended source based on the FM test data. This is used to derive a ‘fringe flat’, and example of which is presented in [15](#). The extended source fringe flat is used both in MIRISIM to model the effect as well as in the JWST pipeline to correct for it.

This basic correction is insufficient to properly correct for fringing, and in the worst case can add additional fringing effects to the data. Therefore an additional iterative correction is used to attempt to remove fringing frequencies in Fourier space (Lahuis and Boogert, [2003](#); Lahuis and Muller, [2018](#)). Unfortunately, this can also remove real signals from the data. (Argyriou et al., [2020](#)) proposes a novel method for fringe correction based on modeling sources as a collection of point sources, leading to a sum of overlapping point source fringe patterns. They show that this improves fringing correction to sub-percent levels, with mostly uncorrelated residuals.

Due to the dependence of fringing on the incident angle of the light, a single extended source model of fringing is insufficient to describe the full effect. In this work, we implement a more realistic fringing model based on point source FM data and the concepts described in (Argyriou et al., [2018b](#)). Data at various points across the detector is used to apply a unique position dependent fringe flat. We will quantify how this changes the extracted spectra after processing in the JWST pipeline, and examine to what extent present correction methods can remove the point source fringing.

3.2 MIRISIM

The MIRI instrument has been simulated in python as a program known - perhaps unsurprisingly - as MIRISIM (Consortium, [2018](#)). This program takes in an astronomical ‘scene’ along with some configuration parameters to output a detector data product, similar to what will be produced by the actual instrument. MIRISIM is relatively full-featured simulator, modeling

the instrumental PSF, various noise sources and distortions, among other effects. While MIRISIM is functional for all of the MIRI sub-instruments, this report will only deal with the Medium-Resolution Spectrometer (MRS) sub-instrument, described in section 2.3. The objective of this section is to describe the implementation and testing of an updated optical model of the ‘fringing’ effect - an optical effect caused by thin film interference from the multiple layers of the detector.

3.2.1 Architecture

While the full documentation for MIRISIM is available in (Consortium, 2018) and with python documentation in (Cossou, 2018), in this section we will outline the procedure for generating a simulated detector image. In particular, we will emphasize the parameter choices made in the setup for our simulations.

A MIRISIM simulation begins by setting up a **scene** using the `skysim`. This represents the view that the telescope will have of some astrophysical system. In general, a scene can be built from nearly anything: a fits file of an actual observation, models of galaxies and more. Built in are tools for producing simple point source and extended source objects. An SED of arbitrary spectral resolution is then attached to the object from an external file, with units of micron for the wavelength and μJy for the incident flux on the detector. There are also built in tools for blackbody SEDs, and individual lines of arbitrary position and depth. All of our SEDs are generated using `petitRADTRANS` from (Mollière et al., 2019), and attached as an external spectrum. Further details of the spectrum generation can be found in Chapter 4. A background can be applied, representing both astrophysical emission sources as well as thermal emission from the telescope itself. We chose not to include a background term, as background subtraction is using a simple model and image-from-image subtraction will result in an ideal correction.

For our observations, we only consider a single point source within the field of view. While this is an oversimplification, particularly in the case of close in planets, it is not the purpose of this thesis to explore the procedures for extracting a companion spectrum in a contrast limited regime. Instead, we assume that the spectral extraction will be adequate, though our simplification provides somewhat of a best case scenario.

The scene is then processed using a set of instrument and detector simulators `obssim`, `scasim` and `specsim`. These make use of the calibration data products (CDPs) in order to model optical distortions and detector effects. The output of this simulation is a set of uncalibrated data files, similar to what will be produced with on-sky observations. From the scene, an illumination model is produced. This transforms the on sky image using telescope and instrument optics in order to produce the intensity pattern incident on the detector itself. As our observations make use only of the MRS, they are then processed using `specsim`, which makes use of the `pySpecSim` module. This module is where most instrumental effects are applied, including detector sensitivities and fringing. These are applied by multiplying the illu-

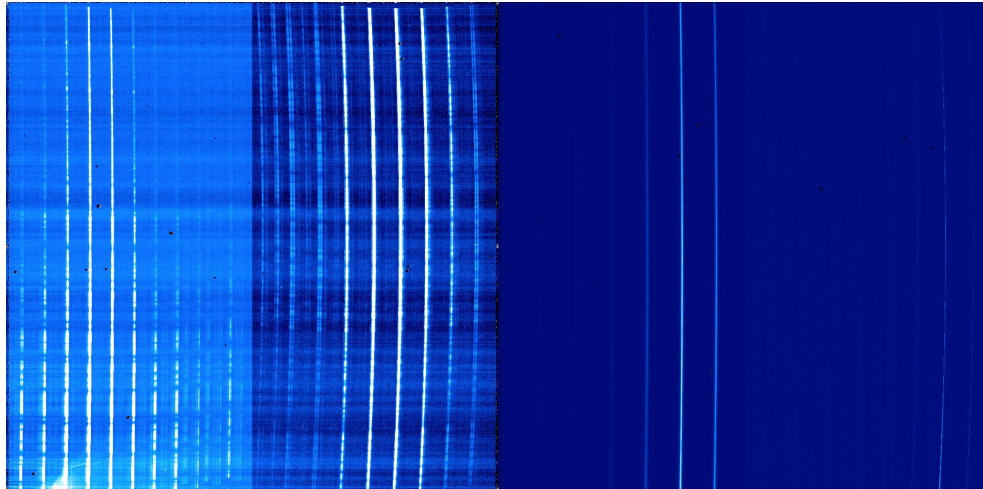


Figure 14: **Right Panel:** Channel 1 (left) and Channel 2 (right). **Left Panel:** Channels 3 (right) and 4 (left). Observation of WISE 0855 using the SHORT disperser. Fringing has been disabled for this particular observation. The color scale is in $\text{sqrt}(\text{DN})$ to highlight faint features.

mination model by the CDPs. The set of fringe CDPs covers each of the MRS sub-bands, and contains a fringe flat. This is a 2D array of multiplicative factors used to apply the fringe pattern to the illumination model, an example of which is given in Fig 15. Presently, these are derived from extended source CV data, CDP version 07.02.05. Once detector effects are applied, and the incident flux is converted into DN counts, a detector image is produced and stored in a fits file. A raw detector image for WISE 0855 is shown in Fig. 14

When running a simulation, the user must set the observation parameters. This includes setting the instrument used (MRS), dither pattern, readout mode, and further MRS parameters. Our parameter selections are based on the parameters used in the JWST ERS and GTO proposals for our target objects, described in more detail in 4.3 and summarized in table 6.

3.2.2 Data Products

All of the CDP files are derived from test campaign data, and represent the best empirical knowledge of the instrument. The primary CDPs of interest for this project are the photometric calibration data products and the fringe flats. The PHOTOM files map the sensitivity of each detector pixel in order to represent the varying sensitivity of the detectors with wavelength. They convert from an incident flux to detector counts based on measured efficiencies. Recently the PHOTOM files were modified from being divided into the illumination model to being multiplied in. This, along with other

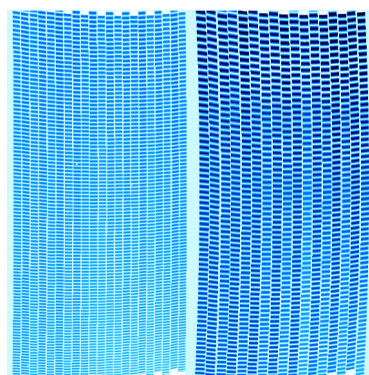


Figure 15: Fringe flat derived from FM data for the SW detector, in the SHORT sub-band v07.02.00. Color scale is linear.

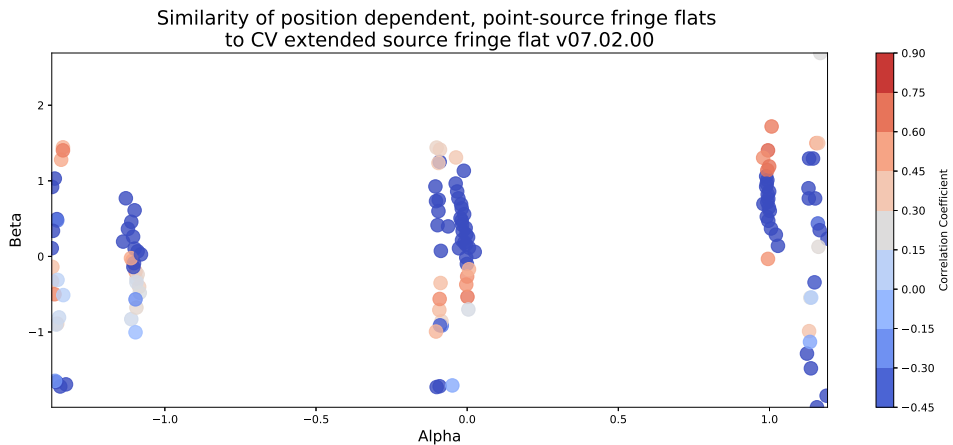


Figure 16: Spatial variation of the point source fringe flats as compared to the extended source model.

issues, has led to inconsistencies between the input flux and output of the JWST pipeline. To best correct for this, we ensure that we are using the most up-to-date PHOTOM files (v8B.04.00) in both MIRISIM and the JWST pipeline. Even still, there remains residual fringing and absorption features present in the PHOTOM CDP files, leading to errors in the extracted spectrum. Notably there is a large spike in channel 2A, and significant high frequency modulation in channel 2C.

The FRINGE CDP files contain fringe flats which are multiplied into the illumination model. Presently, these are based off extended source CV data (v07.02.05). However, for point source observations this produces results very different than is measured (Argyriou et al., 2018b). Thus we attempt to improve the fringing model by using a set of fringe flats derived from point source FM data. In principle, a complete set of fringe flats that cover point sources located at each position in the detector plane would reproduce an extended source fringe flat. Indeed, at the center of the PSF, the extended source fringe flat models the point source fairly well, with discrepancies increasing towards the PSF wings (Argyriou et al., 2020). Due to this variation of the fringe pattern, there is a spatial variation in the similarity of the point source fringe flat as compared to the extended source, which we demonstrate in Fig. 16, where the correlation coefficients between each point source spectrum and the extended source spectrum are plotted. In order to fairly compare our improvements, we will also compare to an older version of the fringe CDPs (v07.02.00) which is based on FM extended source data.

3.2.3 Fringing Model Implementation

Ultimately the data collection from the FM campaign produced a series of fringe flats of an almost point like at various position across the detector and in each channel. We implemented a new routine into the pySpecSim module of MIRISIM to read in the location of point sources within a scene, and apply the nearest available position dependent fringe flat.

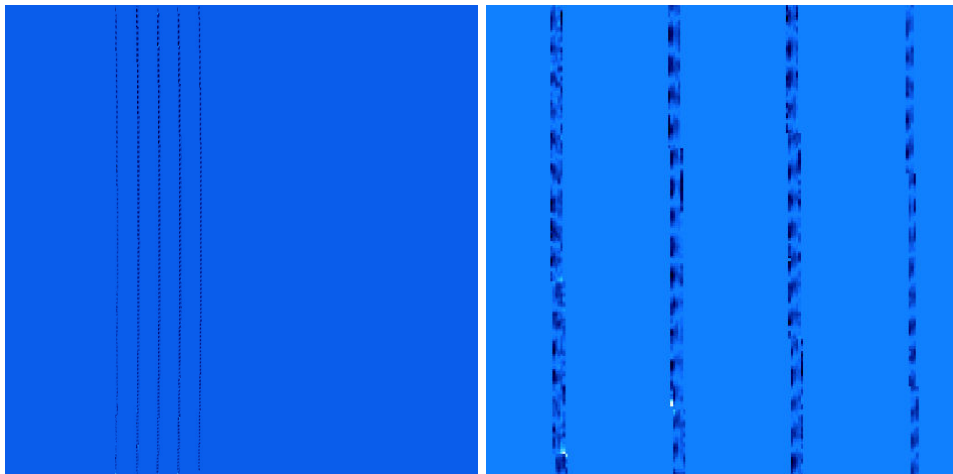


Figure 17: Fringe flat derived from FM data for a point source in channel 1A at $\alpha = 1.001$, $\beta = 0.602$. Colour scale is linear, right is a closeup for detail.

Dithered observations are accounted for, with unique fringe flats being applied to each exposure. A new dithering strategy was designed, such that the locations of each exposure correspond to the locations of the nearest fringe flat to the standard dither offsets.

This implementation comes with several caveats: namely that the fringing model is not yet fully developed, so it can only be considered accurate for point sources located at the same (α, β) location as the source used to produce the fringe flat. Additionally, the source used to generate the data is not a true point source, nor are there fringe flats produced for the full MRS wavelength range. We stress that the goal of this testing is to demonstrate the significance of this effect to justify the need for a more complete model along with additional calibration data to constrain the detector layer parameters.

3.3 JWST PIPELINE

The JWST Pipeline is used for reducing all data from the telescope, and is currently under development by the Space Telescope Science Institute. The latest version of the pipeline (vo.15a) is used for all processing within this work (Bushouse et al., 2015). It is broken into several stages. Stage one is applied to all telescope data, and corrects for detector level effects. Stage two provides photometric calibration, with separate pipelines for imaging or spectroscopic data. Stage three, which is unused in this work, will provide high level science products for end users.

3.3.1 Stage 1 Processing

The raw data files read from MIRISIM (or eventually the MIRI instrument itself) are a series of *exposures*, each made up of set of *integrations* containing a some number of *groups* or frames. Each group is a non-destructive read-out of the detector arrays, providing a series of increasing counts known

as ramps in DN (digital number per second). The first stage of the JWST pipeline takes these raw files, applies a series of steps and outputs a single file for each input exposure in units of count-rate. During this stage, several data quality checks are performed, looking for saturated pixels or jumps in the data, which can be used to correct for cosmic rays. Dark current correction is also applied. Finally, the set of frames in an integration are fit with a linear slope in order to calculate the count rate in DN/s. This procedure is applied to all MIRI data. We used default pipeline settings to apply this procedure, and applied all steps applicable to the MIRI instrument. The particular calibration procedures for MIRI MRS data is described in (Labiano-Ortega et al., 2016).

Currently there are issues either in the production of uncalibrated data files in MIRISIM, or in the ramp step in the JWST pipeline. Unsaturated observations (according to ETC calculations) are treated as saturated, leading to incorrect slope calculations, particularly near the center of the PSF. This leads to a significant loss of flux in the final data products. In order to correct for this, we divide our input spectra by a factor of 10 to prevent any saturation, and multiply the final retrieved flux by the same factor.

3.3.2 Stage 2 Processing

For the second stage of processing we use the Stage 2 Spectroscopic Processing pipeline, and apply the steps individually to maintain control over parameters. The second stage pipeline applies instrument specific corrections that result in a photometrically calibrated exposure. For the MRS, this involves the following series of steps, some of which will be described in further detail below.

1. `assign_wcs` Assign a World Coordinate System (WCS) to each exposure.
2. `flat_field` Flatten photometric variation from differences in gain and dark current.
3. `srctype` Assign whether the target is a point or extended source based on input from the raw data files or observation parameters.
4. `straylight` Remove known stray light component.
5. `fringe` Divide by an extended source fringe flat.
6. `photom` Photometrically calibrate the exposure based on known pixel sensitivities and areas.
7. `cube_build` Transform from a (set of) 2D detector images to a 3D IFU cube in (α, β, λ) .

Photometric Calibration

Photometric calibration is the process of removing detector and optical biases to ensure that the measured output corresponds to the true flux incident onto the telescope. This process occurs in the PHOTOM step of the JWST

pipeline, and uses reference files which store per-pixel photon-to-electron conversion efficiencies along with pixel areas in arcsec to transform the count rate data product to a surface brightness measurement. This corrects for the wavelength dependent bias shown in Fig. 12.

However, this step remains under development, and does not produce absolutely calibrated images. In particular, even using the most up to date reference files (v8D.04.00) there remains discontinuities between channels, and poorly calibrated spectral slopes. In particular there remains a significant high frequency modulation in channel 2C, and a large spike in the flux in channel 2A. Corrections for these issues are planned for a forthcoming CDP release. Fringing effects appear in most PHOTOM CDP files, adding an additional fringing component that is not removed during standard fringing correction. While we expect the photom files should not affect the output spectrum as they are simply multiplied in and divided out, these effects that are visible within the CDP files remain present in the extracted spectrum. This is a substantial limitation for spectral extraction, and must be rectified prior to analysis of on sky data.

Fringing correction

Fringing correction within the JWST pipeline is accomplished by dividing a known fringe flat into the detector image. This fringe flat is based of extended source CV data, and a unique flat is used for each detector/sub-band configuration.

Residual Fringe Correction

While not a part of the JWST pipeline, we also examined the use of Residual Fringe Correction (RFC) (Lahuis and Boogert, 2003; Lahuis and Muller, 2018) to remove fringing from photometrically calibrated data products. This is an iterative procedure that fits 20 sinusoids of varying frequency and amplitude to each iso-alpha contour in order to detect and remove fringing patterns. We applied this procedure to on axis point source fringe data in order to provide a comparison to using the standard fringe correction procedure using an extended source fringe flat. There is currently a conflict between the `dark_current` step in the JWST pipeline and the RFC, and therefore this step was not applied to data using the RFC.

Cube Building

In order to extract the spectrum measured by the MRS, the detector image is converted into an IFU Cube in (α, β, λ) space, using the transformation which was outlined in Fig. 9. A set of transformations for each band maps each detector pixel to a spaxel in cube space, accounting for optical distortions. These transformations produce an irregular grid that samples the on-sky intensity, which can then be combined into a regularly spaced grid of spaxels. Each spaxel filled by a weighted sum of points, with the weight decreasing exponentially with distance from the spaxel. This should also account for changes in the MIRI PSF with wavelength, however issues with the cube building prevent use of the `miripsf` weighting scheme. Instead, the

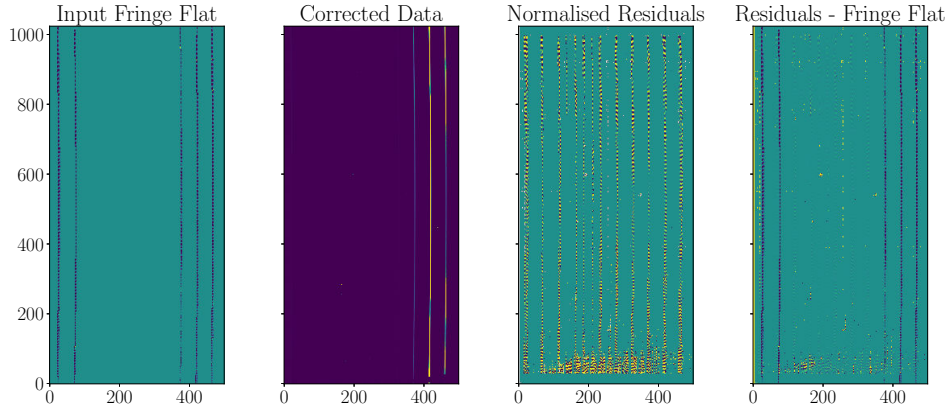


Figure 18: An example of the results produced using residual fringe correction.

flux-conserving Shepards method is used, setting the weighting parameter to 'emsm'. It should be noted that this procedure introduces correlations between the spaxels, which is not accounted in the error on each spaxel.

Aperture Photometry

Once the data from the pipeline has been transformed into a spectral cube, we can perform aperture photometry using the photutils package to extract a 1D spectrum of the source. For each frame in each sub-band the coordinates of the spaxel at with the peak flux is detected using photutils `find_peaks`, which provides the location for the center of a circular aperture. A radius of 5 spaxels is used to encompass the entire PSF for a point source. The input file must be photometrically calibrated, with units of surface brightness in mJy/as². Using the `aperture_photometry` function, we sum all of the contributions within the central aperture. Via a set of additional apertures, we measure and subtract the median background surface brightness. This measurement is then converted into flux units by multiplying by the spaxel area in as². The standard deviation of the background measurements is used to define the error on the flux measurement. In order to remove outliers, we consider a window of 40 points on either side of a measurement, and determine that any point that is greater than 7σ outside the median of this window to be an outlier. Outliers are set to the median value of the window, with the error on the point increased to 1/2 the value of the point. While optimal extraction techniques exist, given our known input signal and background, this procedure is adequate for producing a spectrum in each sub-band, which can then be combined into a single spectrum for all measured sub-band.

Unfortunately, due to the issues described above with the PHOTOM step of the JWST pipeline, the spectrum built using aperture photometry does not accurately reflect the input spectrum in slope or absolute photometry. Therefore, we correct the extracted spectrum channel by channel. We fit a fifth order polynomial template spectrum and the extracted spectra. The fit to the extracted spectra is subtracted from the data, and the fit to the

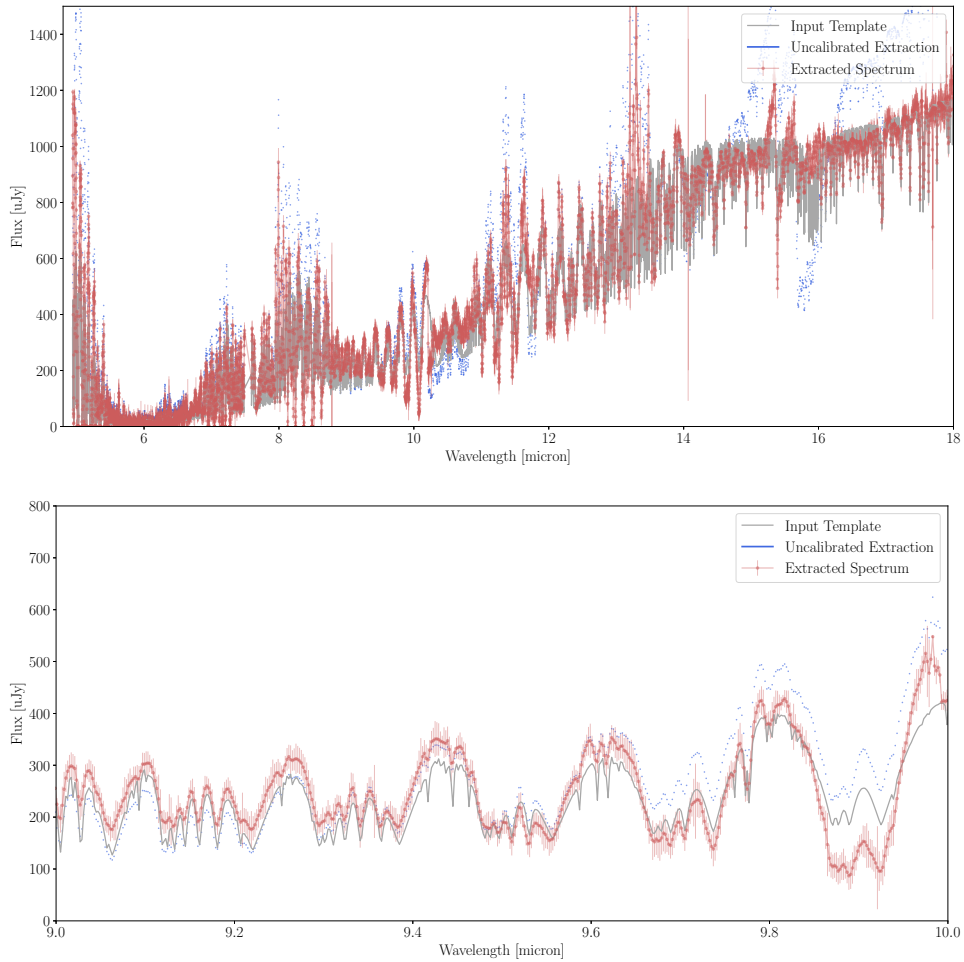


Figure 19: **Top:** Comparison of an input spectrum generated using petitRadTrans and the empirically calibrated output spectrum after extraction using aperture photometry from the cube produced by the JWST pipeline. **Bottom:** Close up around between $9\text{-}10\mu\text{m}$ to highlight small features.

template is added. In order to justify this fit we consider the reduced chi square of the fit to the data: if the fit is not good ($\chi^2/\text{DoF} > 5$), we simply use a median filter to center the data around zero, before applying the fit to the template spectrum. This ensures that poor fits do not significantly alter the spectral shape. Thus this procedure corrects the slope and median flux value, but does not affect high frequency noise or signals. In practice, both curve fitting and median subtraction produce similar results, but it is important to note that this procedure cannot be applied to real data where the ground truth is not known, but is only a method used to correct for current issues with the simulation and data reduction software. Fig. 19 shows an example of the results of this procedure. We believe that this is a justified measure, as the errors with photometric calibration in the pipeline should be resolved after commissioning of the telescope. Examples of the extracted spectrum for each target are included in appendix A.1

3.4 CROSS CORRELATION

To quantify the similarity of the spectrum output by the JWST pipeline to the input into MIRISIM, we rely on the technique of cross correlation. Originally used in a spectroscopic context by (Simkin, 1974) in order to compute galaxy velocity dispersions, cross correlations have become a popular technique used to quantify exoplanet parameters (I. Snellen et al., 2014).

For two arbitrary, complex-valued functions $f(t)$ and $g(t)$, we can compute the cross correlation as a function of the shift τ between the functions (typically in time or velocity space):

$$(f \star g)(\tau) \equiv \int_{-\infty}^{\infty} f^*(t)g(t + \tau)dt \quad (3)$$

Our signals of interest are astrophysical spectra, measured in a finite number of discrete wavelength bins. For such a signal with M bins:

$$(f \star g)[n] \equiv \sum_{m=0}^{M-1} f^*[m]g[m + n] \quad (4)$$

Care must be taken when cross correlating signals, as differences in normalization can result in changes in the correlation coefficient. Our procedure takes in two spectra. The first is an emission spectrum produced by the petitRADTRANS program (Mollière et al., 2019), which provides our forward model with which we compare our data spectrum. Our data is the result of passing the template spectrum through MIRISIM, and extracting it from the resulting detector image using the JWST pipeline. We then rebin the high-resolution input spectrum to the same wavelength bins as the data spectrum, using the `spectres` package (Carnall, 2017). Prior to normalization, we remove any outliers from the spectrum (due to binning errors or instrumental effects) by setting any data points separated by more than 10 standard deviations from the mean to the median value of the spectrum. We then apply a median filter with a window of 55 datapoints, which we then subtract from the unfiltered spectrum. A window size of 55 was in order to remove the continuum of the spectrum, without affecting larger scale features. We compared the use of a median filter to a Savitsky-Golay polynomial filter, and found no significant changes to the results. This removes the continuum emission from the spectrum, and centers it around 0. We then renormalize the spectrum by dividing by the maximum absolute value such that the range is in [-1,1]. This procedure removes the continuum which would introduce an overall slope to the cross correlation, but preserves the relative line depths and positions.

The cross correlation between the forward model and itself is computed, excluding the region of interest around 0 offset. This ‘autocorrelation’ is subtracted from the cross correlation between the forward model and the data spectrum in order to remove secondary peaks. Finally, we normalize the cross correlation by the standard deviation of the cross correlation (excluding the central peak), giving an output measured as a signal to noise ratio.

3.4.1 Residual Statistics

In addition to computing the cross correlation between the forward model and the data spectrum, we also examine the residuals between the two spectra. Here we can see any unexpected variations between the two (periodic signals, offsets or other features). We can also examine a histogram of the residuals, normalized by the standard deviation of the data spectrum. This provides us with a distribution which should have a mean of 0 and unit width if the data are unbiased and share a distribution with the true input spectrum.

3.4.2 Molecular Mapping

Cross correlations are used to identify the presence of a given molecular species in the spectrum of an atmosphere (Haffert et al., 2019; Hoeijmakers et al., 2018). By extending our iterating over each spaxel from the MRS cube and using a molecular template rather than the input spectrum, we can examine the impact of fringing on such an analysis.

We use petitRADTRANS to generate a single-species atmosphere in order to generate the molecular emission spectrum templates. We chose to use VHS1256b as our template for this study, and all other atmospheric parameters remain the same, as described in table 5. A mass fraction abundance of 1% was used for each species. The emission spectrum for each of these species is shown in Fig. 20. This is of the same order as the most abundant species, and ensures that molecular features will be strongly present in the normalized spectrum. In Fig. 23 we vary the abundance of a single species to demonstrate its impact on the cross correlation. Using the same normalization procedure described in section 3.4 for each spaxel, we take the peak cross correlation value from within a narrow window around the expected peak at 0 offset between the template and measured spectra. This was repeated for each of the fringing cases and each of the molecular templates. We also compare the cross correlation as computed sub-band by sub-band to the full wavelength range used.

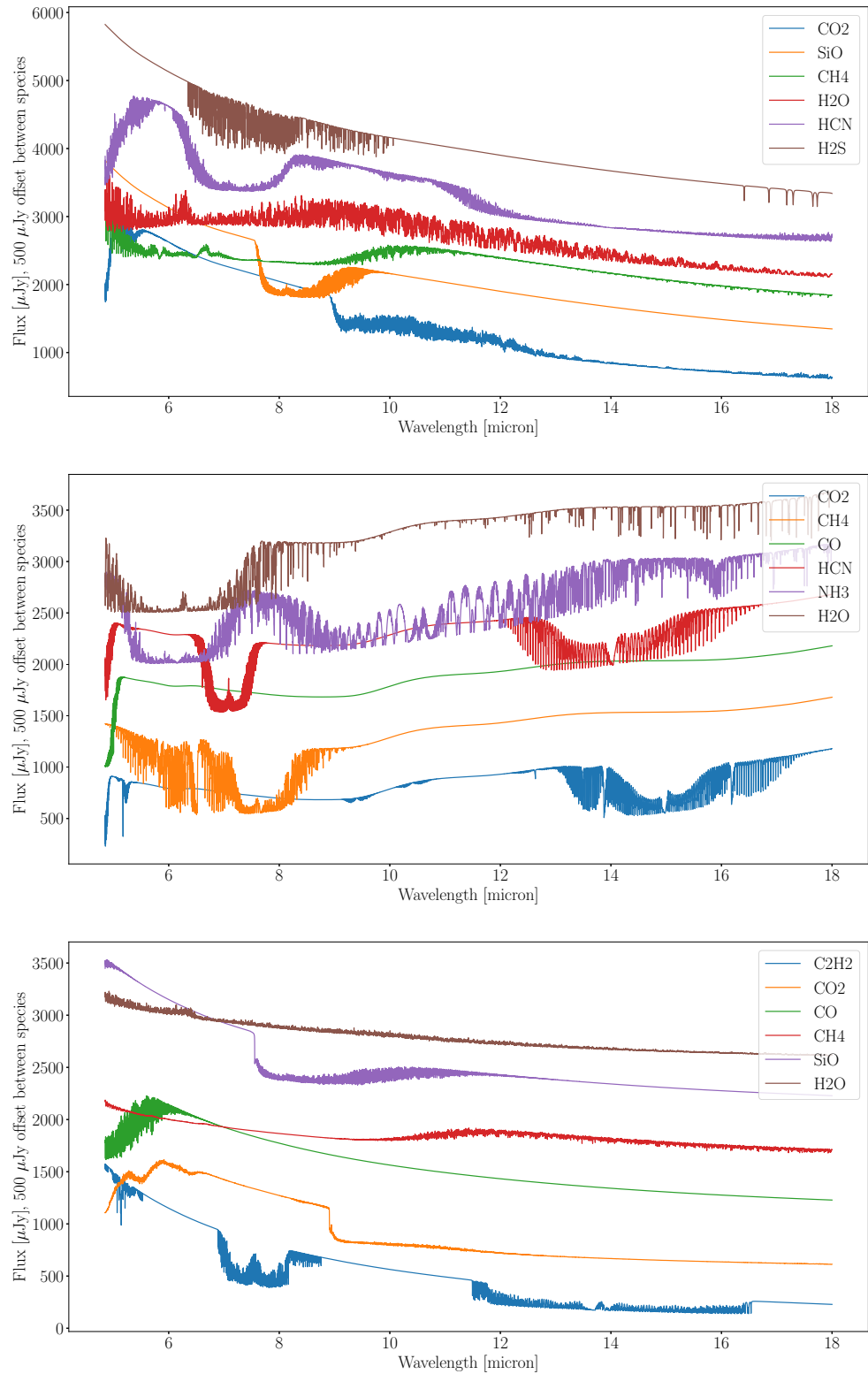


Figure 20: **Top:** Species templates for VHS1256b. Each species emission spectrum is computed using petitRADTRANS with a single species atmosphere with Jupiter-like abundances of H₂ and He and a 1% mass fraction for the remaining species. There is a 500 μJy offset between each species. **Center:** The same, but using WISE 0855 parameters. **Bottom:** The same for 2M1207b.

3.5 RESULTS

We examined the cross correlation between the input template and the extracted spectrum for each of our three targets across 5 cases:

1. No fringing applied in MIRISIM, no correction
2. Extended source fringing, corrected with an extended source fringe flat
3. On axis point source fringing, corrected with an extended source fringe flat
4. Off axis point source fringing, corrected using an extended source fringe flat.
5. On axis point source fringing, corrected using residual fringing correction for each iso-alpha contour

In addition, we compare the extracted spectrum to a set of molecular templates computed in petitRADTRANS, using the atmospheric parameters for each target, but only a single species other than hydrogen and helium at a 1% abundance.

Here we take VHS1256b as our template for analysis. Fig. 21 shows the results of cross correlating the extracted spectra with the input template spectrum for channel 1 of the MRS. Point source fringe flats are only available for channel 1, hence we restrict our analysis of the fringing variation to this channel alone. We show the spectrum normalized to the range [-1,1], along with the residuals from subtracting the extracted spectrum from the template. Note the fringing present in the residuals of the spectrum with point source fringing: dividing by an extended source fringe flat does not properly correct for point source fringing. When compared to leaving the point source fringing uncorrected, applying the extended source flat reduces the SNR by 21%. By examining the distribution of the residuals, we can also see that the widths of residuals varies, with off axis point source producing the widest distribution. Importantly, this corresponds directly to the reduction in SNR of the cross correlation, as shown in the bottom plot.

The cases with no fringing and with an extended source corrected by an extended source fringe flat show nearly identical SNRs of 22.4. This is expected, as using the same fringe flat for both the production and correction of fringing should result in an optimal correction. The point source fringing corrected by an extended source fringe flat fares slightly worse, with an SNR of 19.5. If the point source is off axis, and thus has a different fringe pattern, the SNR worsens to 17.4. Finally, the RFC applied to point source fringing provides a slight improvement in the SNR, increasing to 21.6. These results are similar for each of our targets. Fig. 22 shows the cross correlation results for each target and each examined fringing case for channel 1. Cross correlation plots for each targets are included in appendix A.1.

We also examined the effect of varying the wavelength coverage on the SNR. By including all 3 channels, we found that the SNR increased by a factor of 1.3-1.5 for each case. However, note that the fringing variations

are only in the Channel 1 region of the spectrum, and the extended source fringe flat was used for the remainder of the spectrum where applicable. Thus in a realistic case, we would expect a less significant improvement in the SNR, as the point source fringing will result in a worse correction across the spectrum.

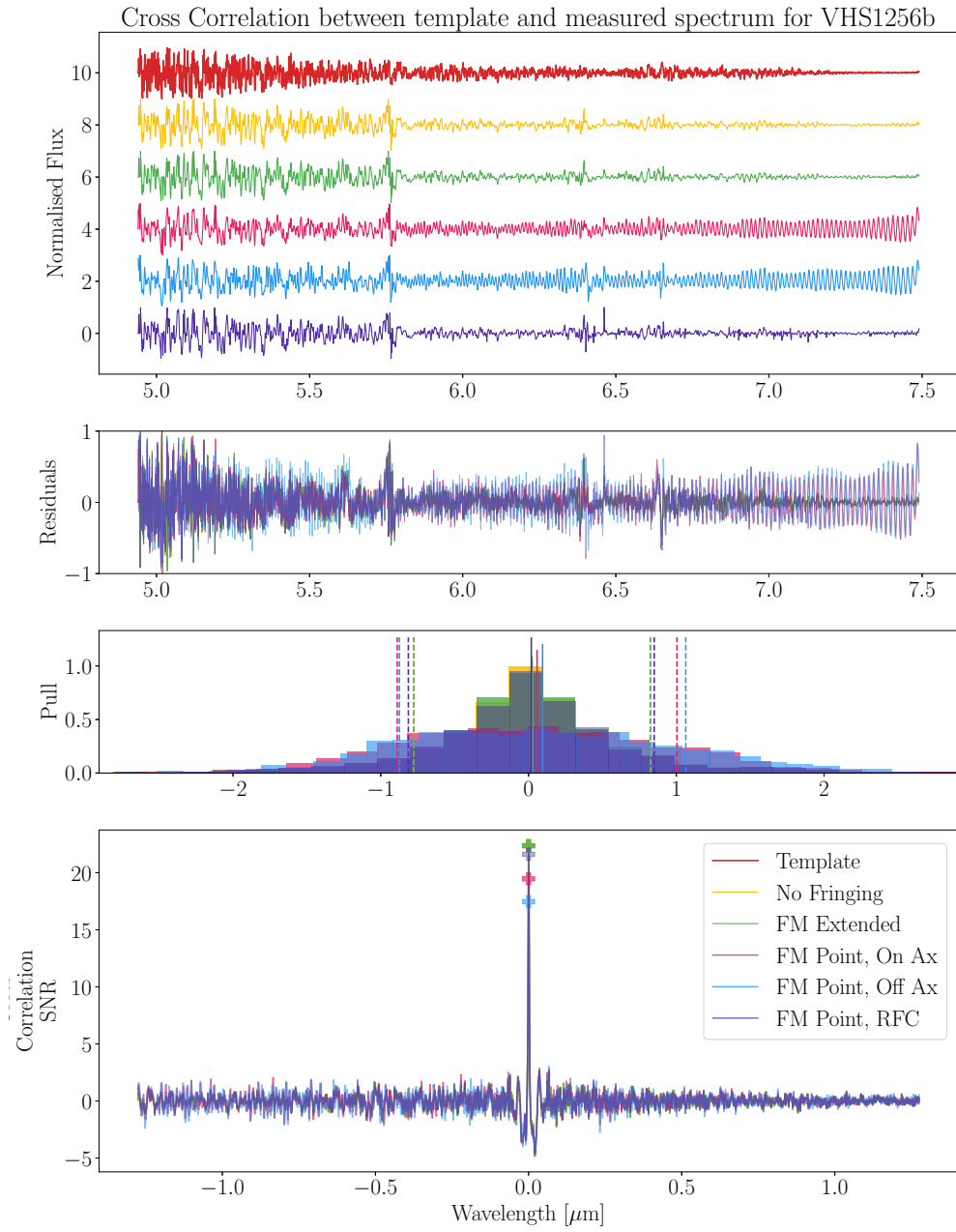


Figure 21: **A.** Normalized CH1 spectra of VHS1256b. **B.** Residuals found from subtracting the extracted spectra from the input template. **C.** Histogram of residuals. Note the difference in the distribution widths due to fringing. **D.** Cross correlation between the extracted spectra and the template. The no fringing, extended source and on axis peaks overlap.

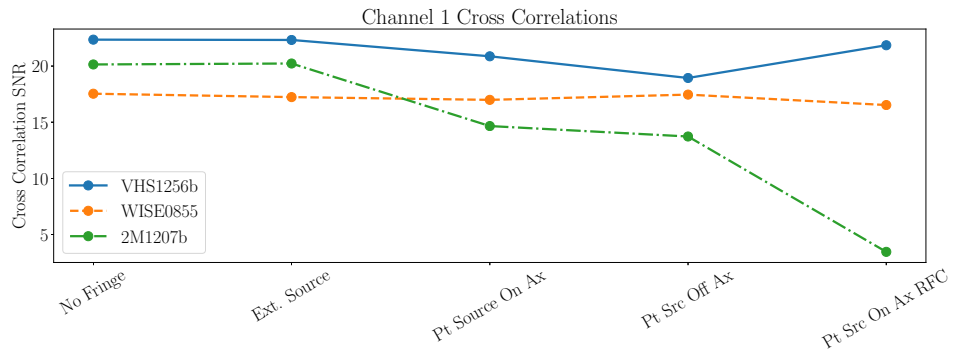


Figure 22: CH1 Cross correlation SNRs for each target and each fringing case. Cross correlations are between the input template and the extracted spectrum.

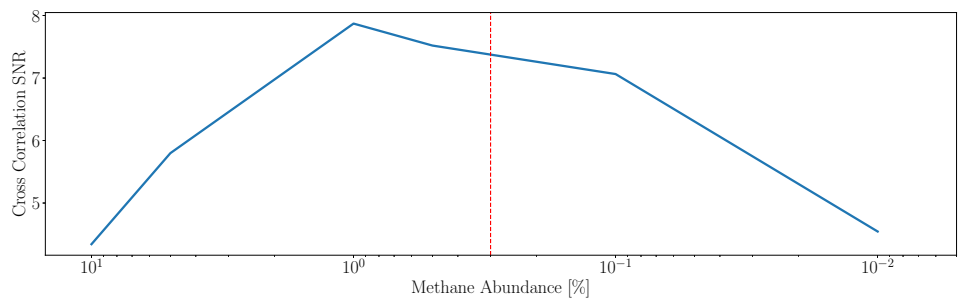


Figure 23: Dependence of the cross correlation on the abundance of a methane species template. The true abundance in the full atmosphere is marked with the red dashed line.

3.5.1 Molecular Mapping

Species Detection

In order to best identify any molecular species present in the atmosphere, we cross correlate the 1D spectrum extracted through aperture photometry with the molecular templates in order to maximize the available flux. Following the procedure for cross correlating the extracted spectra with the full input template, we show the results of cross correlating the extracted Channel 1 and full wavelength spectra with the molecular templates in Fig. 24 for VHS1256b. The SNR values reasonably trace the input abundances of each species, 5σ detections for each of the three most abundant species in water, methane and CO, with mass fraction abundances of 1×10^{-3} , 3×10^{-3} and 1×10^{-5} respectively. Although carbon dioxide has the same input abundance as CO, it was not detected at the 5σ level. However, the detection of CO required the use of the full 5–18 micron spectrum, while both water and methane were detectable in a single channel. Notably however, methane is detected as less abundant than water. This may be due to suppression of the methane features due to strong water and CO lines. As visible in Fig 20, the relative line depths at a 1% abundance are deeper for water than for methane, which could also lead to a more significant cross correlation. We examined the dependence of the cross correlation on the abundance of a given species by varying the abundance of methane from 0.1% to 10%, shown in Fig. 23.

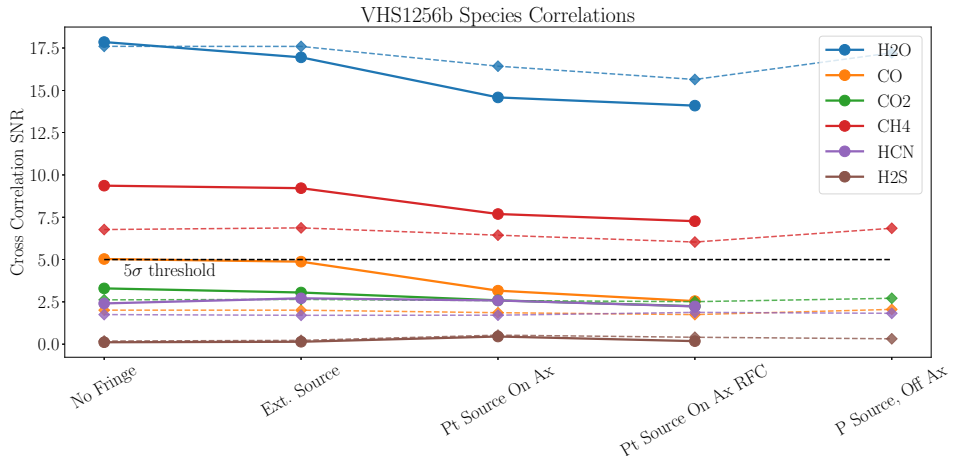


Figure 24: Channel 1 Cross correlations for each molecular species against the extracted spectra for VHS1256b. The input abundances of each species are given in table 7. Solid lines indicate the full wavelength range was used, while dashed lines are for channel 1 only.

We see that within an order of magnitude of the true value, the cross correlation is relatively constant, but drops off at significantly higher or lower concentrations.

Another feature seen in Fig. 24 is the variation in the SNR due to the different fringe correction methods. The poor correction for point source fringing results in a moderate decrease in the SNR, while the RFC provides effective correction.

Figs. 25 and 26 show similar results for 2M1207b and WISEo855 respectively. For CO, the increase in coverage results in a shift from a marginal to a strong detection. Note that this comparison is limited, as point source fringing is only available for channel 1, and the remainder of the spectrum uses extended source fringing. We observe significant decreases in SNR when point source fringing is used. The SNR for water is reduced by half, while CO drops below the 5σ detection threshold. This demonstrates the necessity of improved fringe correction if detections of even relatively abundant species are to be made. In particular, we found that the RFC was not effective for 2M1207b. This is likely due to the relatively weak input signal without strong molecular lines, resulting in significant degradation of the spectrum by the procedure.

WISEo855 demonstrates the necessity of examining specific wavelength regions of interest for each species. NH₃ is the most abundant species within its atmosphere, but due to strong absorption in Channel 1 it requires the full spectrum for a strong detection. This target also demonstrates the possibility of false positives from the cross correlation technique. CO is present only at the 10^{-15} level within the WISEo855 atmosphere, but achieves a 5σ detection. Examination of the spectral template in Fig. 46 (included in the appendix) shows that the CO template lacks significant spectral coverage, and the cross correlation does not result in a significant peak amidst the noise.

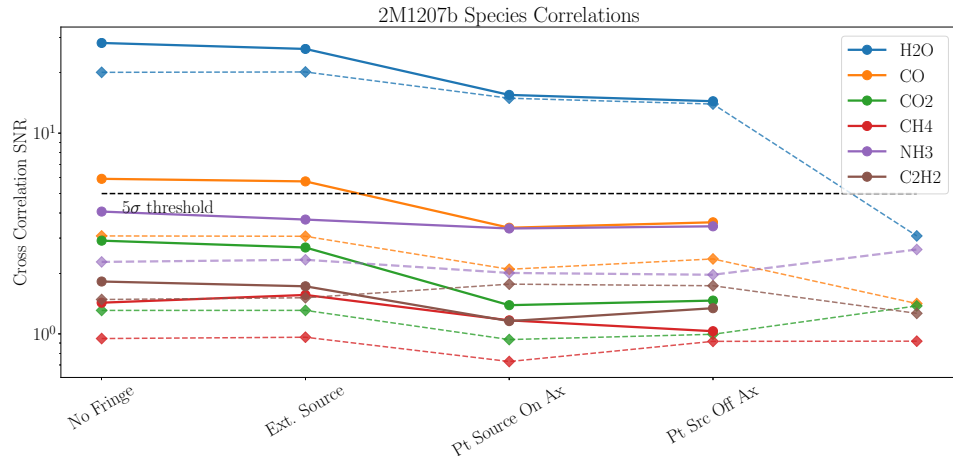


Figure 25: Cross correlations for each molecular species against the extracted spectra for 2M1207b. Solid lines indicate the full wavelength range was used, while dashed lines are for channel 1 only.

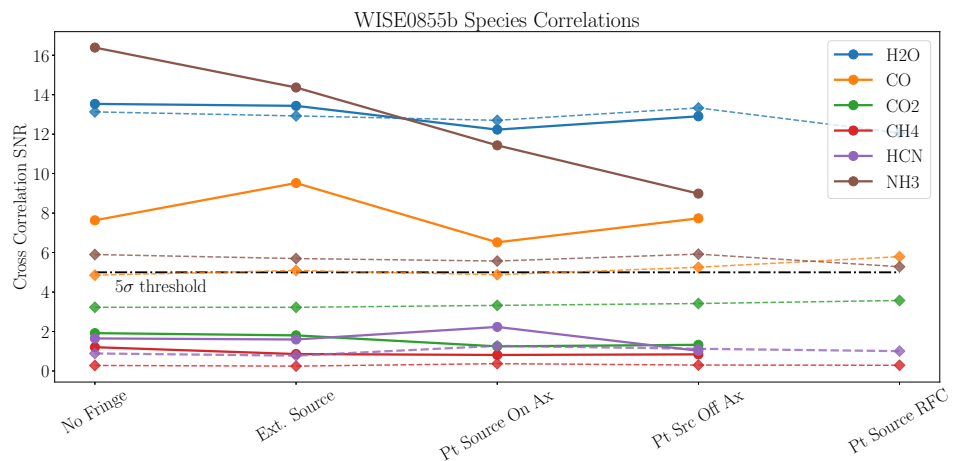


Figure 26: Cross correlations for each molecular species against the extracted spectra for WISE0855. Solid lines indicate the full wavelength range was used, while dashed lines are for channel 1 only.

Object Detection

In addition to detecting the presence of a given species in a known planet, we can use molecular templates to identify the presence of an object. In practice, this would involve iterating through a grid of single species spectral templates, and cross correlating with each spaxel in the IFU cube. Using species known to be present or absent from the target atmospheres, we aim to demonstrate that this technique is effective for MRS data.

Fig. 27 illustrates the ability of the MRS to identify a point source from the presence of a species in the atmosphere. The cross correlation was performed on a spectrum from each spatial location in the IFU cube with a single species atmospheric template, with similar parameters as used in the full atmospheric model. This extends the 1D cross correlation used to infer the presence of a species to the full spatial coverage of the MRS. However,

note that this the spectrum extracted from the data does NOT have the same corrections applied as in the 1D case, but is rather the raw data in MJy/sr. As noted in the section on aperture photometry, these spectra depart significantly from the input templates, and are not yet reliable. Following continuum subtraction and normalization, a cross correlation should still provide a robust metric of similarity in the case that the relative line depths and positions are well represented by the spectrum.

We compare highly abundant species on the left, to species with low or no presence on the right for each of our targets, in the case that there is no fringing. For highly abundant targets, the cross correlation traces the JWST PSF. The peak value of the SNR in 2D is not expected to be equal to the SNR of the 1D cross correlation, which contains significantly more flux than in any individual spaxel.

For each of our targets, the highly abundant species are detected with a high SNR using only Channel 1 data, and trace the PSF of the object. The normalization procedure emphasizes faint features, and thus the SNR is approximately constant across the PSF, regardless of the sampled intensity. For 2M1207b, the lack of strong molecular features results in a lower cross correlation signal when compared to VHS1256b or WISE0855.

3.5.2 Discussion

We have examined different fringing correction methods, and compared a realistic point source fringing model to the simplified extended source model used in MIRISIM. We find that the point source fringing significantly reduces the SNR in a cross correlation. Apart from marginal detections, this will likely not be the limiting factor in determining the presence of a given species. Residual fringing correction as used in the Spitzer Space Telescope can reduce the impact of fringing on an extracted spectrum, but also has the potential to degrade the spectrum. The results of this procedure should be examined closely to ensure that it has been correctly applied, and it will likely prove more useful for bright targets than for faint sources.

This analysis is limited by the development status of both MIRISIM and the JWST pipeline. Calibration is an ongoing process, and the CDP files available as of March 2020 still leave significant residual effects present in the extracted spectrum. Photometric calibration must be done in an empirical, ad hoc fashion that cannot be applied to real data without ground truth photometry. Until these issues are resolved, spectral extraction of real data using the MRS will be extremely limited.

Cross correlations provide a useful tool for quantifying the similarity of two spectra, identifying the presence of molecular species and identifying variation between different data processing methods. However, a cross correlation does not retrieve an actual abundance. For that we must use an atmospheric retrieval, as described in Chapter 4. This does provide a useful tool for guiding which species should be included as free parameters in an retrieval, as well as for identifying the presence of a companion given the variation in the spectra between the host star and the companion.

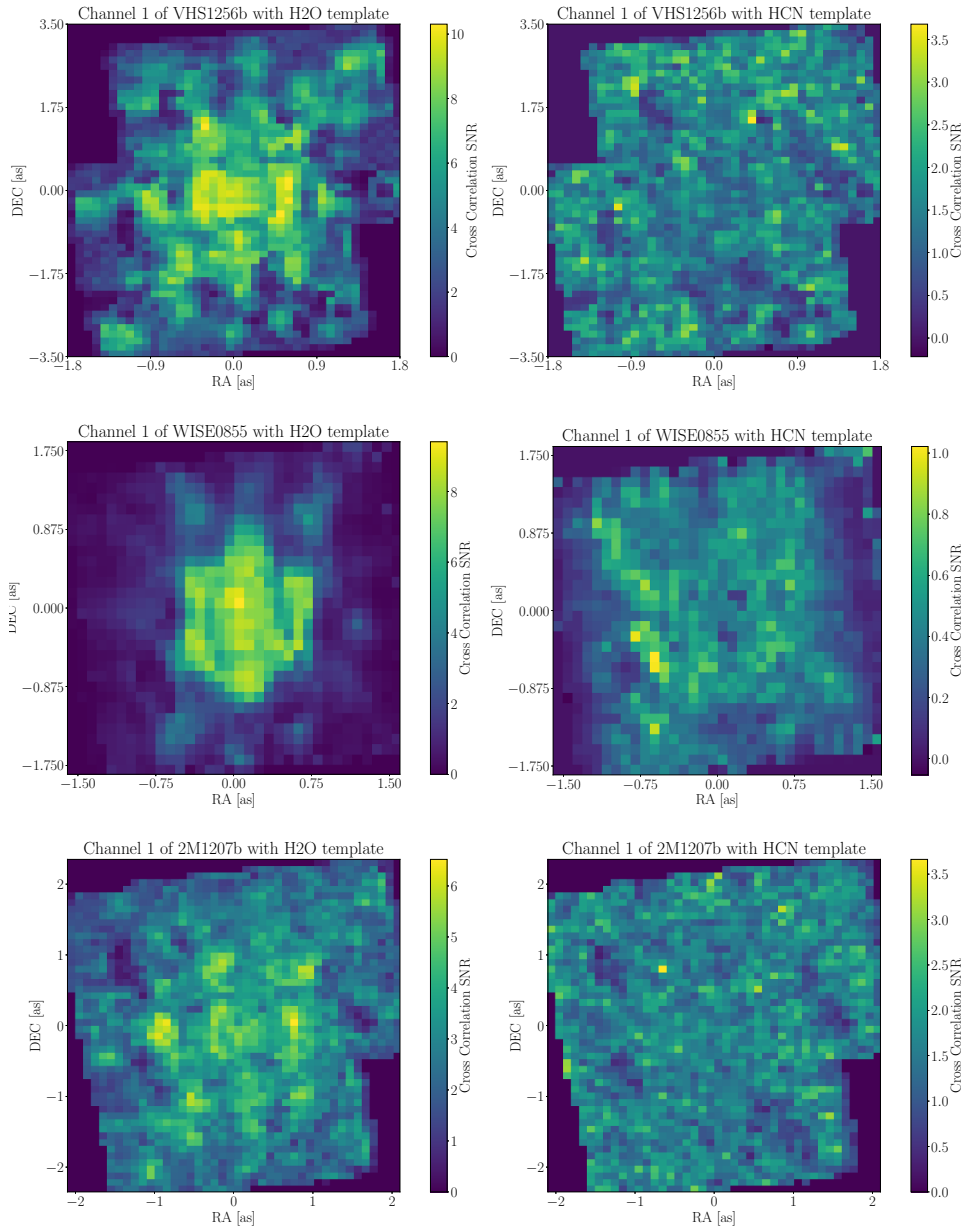


Figure 27: Cross correlations for each of the targets with a selection of molecular templates, with no fringing applied. On the left is H₂O, on the right is HCN. Due to the normalization the cross correlation exaggerates low-flux features, tracing the JWST PSF. From top to bottom: VHS-1256b, WISE0855 and 2M1207b.

4

ATMOSPHERIC RETRIEVALS

Every photon of light that we receive from an exoplanet will interact with its atmosphere, and will therefore provide us with a hint of what that atmosphere may look like. An atmospheric retrieval is the process of reconstructing the atmosphere of an object based on an observed spectrum. This process relies heavily on having accurate models which can be parameterized by the physical quantities we are interested in: generally the temperature, pressure and composition (Madhusudhan, 2018). As these models cover a very large parameter space (>10 parameters, each covering several orders of magnitude), it is necessary to have an efficient method for sampling this space, computing a model and comparing this model to the data (Benneke and Seager, 2012; Benneke, 2013). Currently, atmospheric retrieval methods have been used for both exoplanets and brown dwarfs to identify water, methane, CO, CO₂ and other species (Barman et al., 2015; Konopacky et al., 2013), along with clouds being a universal feature (Line et al., 2017; Morley et al., 2018; Schlawin et al., 2018)

This chapter will outline the process of an atmospheric retrieval from modeling to marginalization of posteriors, and will examine the impact that the instrumental effects described in Chapter 3 have on the retrieved parameters. Additionally, this will provide an example of how the MIRI MRS can be used to explore exoplanet and brown dwarf atmospheres, and what observational parameters should be considered when studying these objects, following similar studies from (Batalha et al., 2018; Schlawin et al., 2018) for NIRSpec and LRS observations and (Feng et al., 2018) for future reflected light missions.

Atmospheric Modeling

Atmospheric modeling is the task of creating spectra based on the physical properties of the atmosphere. This is a broad task that can range from a 3D Global Circulation Model (GCM) which accounts for self-consistent atmospheric chemistry (Chen et al., 2019) to a 1D model based around an empirical temperature-pressure profile (Mollière et al., 2019). The choice of model depends largely on the requirements for accuracy and computational cost. Considering the potentially millions of possible atmospheres that must be examined in a retrieval problem, whatever model is used must be computationally efficient while still maintaining a close approximation of reality.

4.1 PETITRADTRANS

For this work we chose to use the petitRADTRANS package due to its user-friendly python implementation, high speed computation for retrieval use and extensive high-resolution, line-by-line spectral library for generating

Property	Description
Temperature	Parameterized, e.g. (Guillot, 2010)
Abundances	Parameterized, e.g. vertically constant
Scattering	Cloud scattering, transmission spectra only
Clouds	Power law and condensation clouds
Cloud particle size	f_{SED} and K_{ZZ} or parameterized
Particle size distribution	log-normal, variable width
Cloud abundance	Parameterized
Wavelength spacing	R=1000 (c-k), 10^6 (lbl)
Valid emission spectra	Clear, from NIR and longer

Table 5: Description of the parameters available in petitRADTRANS. For cloud particles, f_{SED} is the mass-averaged ratio of the cloud particle settling speed and mixing velocity. K_{ZZ} is the atmospheric eddy diffusion coefficient (Ackerman and Marley, 2001)

planetary spectra (Mollière et al., 2019). It is a 1D, radiative transfer package with many parameters options, described in table 5. PetitRADTRANS can compute both emission and transmission spectra, with an output spectral resolution of R=1000 in correlated k mode, or R=1 000 000 in line-by-line mode.

Note that much of the following sections applies to many other similar 1D radiative transfer atmospheric modeling programs such as ATMO (Goyal et al., 2019), Planetary Spectrum Generator (Villanueva et al., 2018), HELIOS (Malik et al., 2017, 2019) and others. Many (or even most) of these programs rely on the same set of high-resolution molecular line lists, including HITRAN/HITEMP (Gordon et al., 2017; Rothman, 1981; Rothman et al., 2010), ExoMol/ExoCross (Tennyson and Yurchenko, 2017; Tennyson et al., 2016; Yurchenko et al., 2018) and others.

4.1.1 Radiative Transfer

In order to compute the emission spectrum an initial featureless black-body spectrum $B(T_{int})$ is passed through multiple discrete layers of the atmosphere, parameterized by their temperature, pressure, and the opacities of each of the species present in a given layer. Modeling each layer as plane parallel, the intensity is computed as in (P. G. Irwin et al., 2008; Mollière et al., 2017, 2019)

$$I_{top} = B(T_{int})\mathcal{T}^{atmo} + \frac{1}{2} \sum_{i=0}^{N_L-1} \left[B(T^i) + B(T^{i+1}) \right] (\mathcal{T}^i - \mathcal{T}^{i+1}). \quad (5)$$

N_L is the number of layers in the atmosphere, and \mathcal{T} is the transmission from a given layer to the top of the atmosphere. All quantities are averaged per wavelength bin in c-k mode, while they are evaluated at each wavelength point in line-by-line mode.

In order to compute the temperature structure of the atmosphere, a modified Guillot model (Guillot, 2010) was used, as in (Mollière et al., 2017, 2019). The temperature structure is defined as

$$T(P) = \left\langle T_{Guillot}(P) \left(1 - \frac{\alpha}{1 + P/P_{trans}} \right) \right\rangle_p . \quad (6)$$

As denoted by $\langle \rangle_p$, this profile is boxcar-smoothed over $\log(P)$, with bin widths of 1.25 dex (Mollière et al., 2019). The modified Guillot profile is defined as

$$T_{Guillot}(P) = \frac{3T_{int}^4}{4} \left(\frac{2}{3} + \delta P \right) \quad (7)$$

$$+ \frac{3T_{eq}^4}{4} \left[\frac{2}{3} + \frac{1}{\gamma\sqrt{3}} + \left(\frac{\gamma}{\sqrt{3}} - \frac{1}{\gamma\sqrt{3}} \right) e^{-\gamma\delta\sqrt{3}P} \right], \quad (8)$$

with the second term accounting for irradiation of the upper atmosphere. The opacity parameters $\delta = \kappa_{IR}/g$ and $\gamma = \kappa_V/\kappa_{IR}$ are defined such that the optical depth $\tau = \delta \cdot P$. T_{int} is the internal temperature of the planet, and is equivalent to the effective temperature of the planet, that is the temperature of a blackbody with the same luminosity as itself. T_{eq} is the equilibrium temperature of the planet, based on the temperature of the host star and separation of the planet. For an isolated, free floating object this temperature goes to 0. The remaining free parameters α , P_{trans} simply modify the shape of the temperature structure according to the pressure.

4.1.2 Opacity Sources

To compute the emission spectra of an atmosphere, petitRADTRANS accounts for various opacity contributions including absorption and emission lines, collisionally induced absorption, cloud opacity and scattering and Rayleigh scattering cross sections. These sources are described in detail in (Mollière et al., 2019), summarized in tables 2 and 3. For this work we consider only the case of a cloud-free atmosphere due to the complexity of realistic cloud modeling.

Line-by-line

In its high resolution line-by-line mode, petitRADTRANS computes emission spectra with $R=10^6$. These spectra are computed using opacity sources for molecular and atomic lines from ExoMol/ExoCross library (Yurchenko et al., 2018). Pressure broadening is taken into account using the coefficients from HITRAN/HITEMP (Rothman et al., 2010, 2013) or from (**Sharp2007**) (Eqn. 15). The line opacities are computed from 80-3000 K, and from 0.3-28 μm in high resolution mode.

Correlated K

The low resolution mode of petitRADTRANS uses the correlated-k (c-k) method of computing line opacities (Fu and Liou, 1992; Goody et al., 1989; Lacis and Oinas, 1991). This method for calculating emission and absorption

features assumes that the opacity distribution functions between differing species are uncorrelated, which permits simple computation of overlapping features. While petitRADTRANS implements a c-k method with a spectral resolution of 1000, in principle it is accurate to much higher resolutions. However, the principle utility of the c-k method is in the dramatic reduction in computational cost for computing a spectra such that petitRADTRANS can be used as the foundation for an atmospheric retrieval code requiring hundreds of thousands or millions of models to be generated. (Mollière et al., 2019) discusses the variations between the results of the line-by-line method and the c-k method, finding discrepancy of at most 6%. Typical variation is much lower, as seen in Fig. 2 of (Mollière et al., 2019).

Clouds

While clouds are a seemingly universal feature in exoplanets and brown dwarfs (Faherty et al., 2018; Line and Parmentier, 2016; Morley et al., 2014), they remain a difficult problem for retrieval studies. Clouds form when a species condenses out of the gas phase, typically around a small nucleus. This creates a layer of particles at a reasonably well defined altitude in the atmosphere, and prevents the observation of deeper atmospheric layers. While a simple model of clouds may be a ‘gray’ cloud deck that acts uniformly across wavelength, a more complex model will account for differing IR and visible opacities, as well as particle scattering and other complex microphysics. From experience on Earth and within the solar system, cloud systems are highly complex and variable, with shifting cloud coverage and structure. The mid infrared in particular may allow for an observational window to probe deeper atmospheric layers and begin to characterize cloud composition. In current retrieval codes, clouds are generally designed from a simple model based on a given particle distribution (Ackerman and Marley, 2001), or simply as a gray cloud deck at a specified pressure level. Both of these models are implemented in petitRADTRANS. These models do not agree well with microphysical models, and lead to substantial difficulties in the interpretation of retrieved spectra. This remains an open problem for atmospheric retrievals, and we do not attempt to examine cloud effects in this work, instead choosing the simple, though unrealistic case of a clear atmosphere. (Schlawin et al., 2018) examines potential impacts of clouds on atmospheric retrievals with the MIRI LRS.

4.2 BAYESIAN INFERENCE

An atmospheric retrieval is the process of extracting information about physical parameters from a measured spectrum. In general this procedure involves comparing the data to a series of template spectra with known parameters and identifying the best fit model. Unfortunately for astronomers, atmospheres are complicated: typical one 1D models still require many (>15) parameters to generate a somewhat realistic model. This results in a very large parameter space in which to search for the correct set of properties that describe our measurement.

Monte Carlo methods, including Nested Sampling, are used to effectively search this large space using the Bayesian evidence as a goodness-of-fit metric. Here we will follow (Speagle, 2019) to provide a brief overview of Bayesian inference.

To measure the likelihood of a given model, we turn to Bayes' Theorem:

$$P(\Theta_M | \mathbf{D}, M) = \frac{P(\mathbf{D} | \Theta, M) P(\Theta | M)}{P(\mathbf{D} | M)}. \quad (9)$$

In our notation, Θ is the set of parameters that describe a model M , that is fit to the data \mathbf{D} . Bayes' theorem asks what is the probability that the parameters Θ are true given the data and model. The distributions for each parameter are the **posterior** distributions.

This is then related to the **likelihood** $P(\mathbf{D} | \Theta, M)$ of measuring the data given the model, the **prior** probability $P(\Theta | M)$ which describes our degree of belief in our model and the **evidence** $P(\mathbf{D} | M)$, which is marginalized over all possible Θ and quantifies how well the model describes the data. To simplify notation, we adopt the following convention for Bayes' theorem:

$$\mathcal{P}(\Theta) = \frac{\mathcal{L}(\Theta) \pi(\Theta)}{\mathcal{Z}}. \quad (10)$$

In general, the goal of an atmospheric retrieval is to find the best fit model by maximizing the evidence \mathcal{Z} , and as a by product finding the marginalized posterior distributions for each parameter. This comes with many challenges, especially when dealing with large numbers of parameters. Selection of the priors and model will determine the extent to which a result can be interpreted, while sampling large parameter spaces and computing likelihoods introduces substantial numerical challenges. The Nested Sampling method described below attempts to solve the challenges of exploring a large parameter space.

4.2.1 Nested Sampling

Nested sampling attempts to address several of the shortcomings of Markov Chain Monte Carlo (MCMC) methods while simultaneously improving computational efficiency (Skilling, 2004). A particular strength of the method is in the sampling of highly multimodal distributions, removing the problem where an MCMC approach may get stuck in a single local maximum. MCMC methods generate samples ‘proportional to’ the true posterior distributions, which lead to difficulties in computing the evidence \mathcal{Z} (Speagle, 2020). In contrast, nested sampling puts the evidence first and provides estimates of the posterior distributions from the importance weights of the final set of samples. First described in (Skilling, 2004), nested sampling has been adopted as the sampling algorithm of choice within the astrophysics community (Buchner et al., 2014; Feroz et al., 2009; Feroz et al., 2019; Speagle, 2020).

With the goal of parameter estimation, nested sampling attempts to estimate the evidence \mathcal{Z} rather than directly sampling the posteriors (Skilling, 2004). This is done by integrating over the entire parameter space of Θ

$$\mathcal{Z} = \int_{\Omega_\Theta} \mathcal{L}(\Theta) \pi(\Theta) d\Theta. \quad (11)$$

This is difficult.

Rather than attempting to directly solve the entire multidimensional integral, nested sampling transforms this into an integration over the *prior* volume X :

$$\mathcal{Z} = \int_{\Omega_\Theta} \mathcal{L}(\Theta) \pi(\Theta) d\Theta = \int_0^1 \mathcal{L}(X) dX. \quad (12)$$

This is now a contour integral over isocontours $\mathcal{L}(X)$ which bound the prior volume

$$X(\lambda) = \int_{\Omega_\Theta: \mathcal{L}(\Theta) \geq \lambda} \pi(\Theta) d\Theta, \quad (13)$$

which is the fraction of the prior where the likelihood of the data given the model is above some threshold λ . The integration is now simplified into a 1D integration over X , given proper prior selection.

Method

Consider a parameter space with D dimensions. We will describe this space as a unit hypercube, where each parameter runs from 0 to 1. Priors are thus transformations from this space to a physical parameter space. Often the prior is a uniform distribution, which simply scales the space, but it may also be an informative prior such as a normal distribution centered at an expected physical value. In order to sample this space, N_L ‘live points’ are generated, each of which provides a set of parameters Θ . N_L must be greater than $D + 1$, and typically values on the order of $50 \times D$ are used (Feroz et al., 2009). Using a likelihood function $\mathcal{L}(\Theta)$, the evidence \mathcal{Z} can be computed by comparing the model to the data. Having computed the evidence at each point, the live points are then sorted and the point with the lowest evidence is discarded. A set of ellipsoids is drawn around the remaining points. The procedure for computing these ellipsoids is given in (Feroz and Hobson, 2008; Feroz et al., 2009). By using a set of ellipsoids, multiple modes in the parameter space can be encompassed. Once the ellipsoids bounding the remaining points are drawn, a new sample is drawn from within the restricted sample space. The evidence for the new point is computed, and it is accepted if the evidence is greater than the minimum evidence of the previous remaining set of points. The entire procedure is repeated until some convergence criteria is satisfied, with each iteration resulting in a smaller volume being encompassed by the ellipsoids, nested within the previous volume.

This procedure can be improved in many ways, including importance nested sampling (Feroz et al., 2019) and dynamic nested sampling (Speagle, 2020).

4.2.2 Multinest

For our implementation of an atmospheric retrieval code, we chose to use the Multinest algorithm (Feroz et al., 2009) using the pyMultinest wrapper (Buchner et al., 2014) and using importance nested sampling to improve the accuracy of the Bayesian evidence calculation (Feroz et al., 2019). This particular implementation of nested sampling is commonly used in atmospheric

retrieval codes due to its fast Fortran implementation, though it was initially developed for cosmological problems.

Using the pyMultinest package, we implemented the required log-prior function which transforms the unit hypercube to physical parameter space and the log-likelihood function used to compare the model to the data. The full code is available at <https://github.com/nenasedk/petitRetrieval>, and is based of the emission spectrum retrieval described in (Mollière et al., 2019). Retrievals were typically performed using 500 or 1000 live points, with the convergence criteria

$$\Delta \ln \mathcal{Z} = \ln Z_i - Z_{i+1} \quad (14)$$

set to 0.3 for parameter estimation and 0.8 for model comparison, as suggested in the pyMultinest documentation.

4.3 OBSERVATIONS

The targets used in our retrieval study are guided by the JWST ERS and GTO programs. This allows us to use well-defined observing strategies for each object, and present a clear case for the science that can be accomplished with these observations. While all three were discussed in Chapter 1, we will now outline the proposed observing strategies and science cases for each target.

VHS-1256B

VHS-1256b is a young (0.2Gyr), high mass ($11.2 M_{Jup}$) planet at a distance of 12.7pc (Bowler, 2016). The wide separation of 8" makes it an easy target for observation with the MRS, as its host star will fall outside of the FoV. It has a J-band magnitude of 16.662, and a late L spectral type (Miles et al., 2018). As an object of interest for the JWST ERS program 1386, it will be observed with the NIRCam imager, along with both the NIRSpec and MRS spectrometers (Hinkley et al., 2019). Using the MRS, VHS-1256b will be observed using a SLOW readout pattern, using 30 groups per integration, with one integration per exposure using a 2 point dither pattern. This results in a total exposure time of 1433.395s in each of the MRS sub-bands, and will cover the full wavelength range of the MRS. It will be simultaneously imaged using the MIRIM instrument. An additional background only exposure will be taken using the same exposure parameters, but without dithering, for a total of half of the science exposure time.

Methane spectral features have been detected in the L-band spectrum of VHS-1256b (Miles et al., 2018), but mid infrared spectroscopy will allow the use of methane and other molecules to characterize atmospheric properties such as dis-equilibrium chemistry and vertical mixing (C. A. Beichman et al., 2019c).

2M1207b

2M1207b is a 1600K, $10 M_{Jup}$ object at wide separation from its brown dwarf primary (TWA 27) and a distance of 52.4pc (Bowler, 2016). In com-

Parameter	VHS-1256b	2M1207b	WISE 0855
ObsDate	0.0	0.0	0.0
Path	SHORT/LONG	SHORT/LONG	SHORT/LONG
Dither	2 point	4-point	None
Disperser	ALL	ALL	ALL
Detector	SW/LW	SW/LW	SW/LW
MRS Mode	SLOW	SLOW	FAST
Exposures	1	1	1
Integrations	1	1	1
Groups	30	76	180
Cosmic Rays	None	None	None

Table 6: Observing parameters for each selected target. Observation parameters are based on JWST proposals, and set in order to cover channels 1 through 3. For the disperser, ALL implies running a simulation for each of the SHORT/MEDIUM/LONG sub-bands. A total of 6 simulations are necessary to cover the entire wavelength range. Cosmic rays are turned off due to issues with MIRISIM.

parison to VHS-1256b, 2M1207b has a relatively small separation of 0.77'', which is more characteristic of currently known objects. As one of the first directly imaged exoplanets, it provides a template for characterizing young, hot objects, and will be observed in the JWST GTO program 1270 (Birkmann et al., 2019). This observation will use the NIRSpec IFU, MIRIM and the MIRI MRS.

Using the MRS, 2M1207b will be observed using a FAST readout to prevent detector saturation, using 76 groups per integration, and one integration per exposure. It will use a 4 exposure dither pattern, for a total integration time of 843.612s per sub-band, covering the full wavelength range of the MRS. Combined with the NIRSpec observation, this will provide a continuous spectrum over the entire JWST wavelength range. The host star of 2M1207b is faint, allowing for good enough contrast for a straightforward observation (C. A. Beichman et al., 2019c).

WISE 0855-0714

Although it is a Y-type brown dwarf, WISE 0855 is the most similar known object to Jupiter outside our solar system that has been directly observed (Luhman, 2014). At 250K, WISE 0855 is very faint, with an H-band magnitude of 25, but its proximity at 2pc makes it an ideal target for characterization. The JWST GTO Program 1230 will observe WISE 0855 using NIRCam, NIRSpec and the MIRI MRS (Oliveira et al., 2019). It will use a FAST readout, with 180 groups per integration, and one integration per exposure for a total of 999 s of integration time for each sub-band. No dithering will be used.

As a cold object, WISE 0855 provides the best known extra-solar template for older planetary mass objects. With the improved sensitivity and long wavelength coverage of JWST, it is hoped that more low mass and colder exoplanets may be directly imaged. Understanding the atmosphere of WISE 0855 will provide a great deal of insight for the challenges of such exoplan-

Parameter	VHS-1256b	2M1207b	WISE 0855
Radius [R _{Jup}]	1.29	1.5	1.17
Distance [pc]	12.7	52.4	2.23
log <i>g</i>	4.25	3.2	4
T _{int} [K]	900	1600	250
T _{equ} [K]	3.4	10	3.4
κ _{IR}	0.01	0.01	0.01
γ	0.3	0.4	0.3
Abundances			
H ₂	0.898	0.74	0.73
He	0.102	0.24	0.25
H ₂ O	1 × 10 ⁻³	5 × 10 ⁻³	5 × 10 ⁻⁴
CO	1 × 10 ⁻⁷	1 × 10 ⁻²	1 × 10 ⁻¹⁵
CO ₂	1 × 10 ⁻⁵	1 × 10 ⁻³	1 × 10 ⁻¹⁴
CH ₄	3 × 10 ⁻³	1 × 10 ⁻⁶	3 × 10 ⁻⁴
NH ₃	1 × 10 ⁻⁵	1 × 10 ⁻⁷	3 × 10 ⁻³
C ₂ H ₂	1 × 10 ⁻⁸	1 × 10 ⁻⁹	...
HCN	1 × 10 ⁻¹⁰	1 × 10 ⁻⁹	1 × 10 ⁻⁹
TiO	...	5 × 10 ⁻⁷	...
SiO	1 × 10 ⁻⁶

Table 7: Input parameters to generate spectra using petitRADTRANS. High resolution line-by-line mode was used. κ_{IR} and γ are the infrared opacity and ratio of visible to IR opacities respectively. The values chosen for these parameters are based on (Mollière et al., 2019). The mass-fraction abundances chosen are arbitrary values chosen to encompass a wide range of compositions and to test the ability of the retrieval code to recover small abundances. Where possible, values were chosen to qualitatively reflect known species present (Miles et al., 2018).

etary atmospheres. Clouds are suspected to be present (Faherty et al., 2018), a feature which will be better understood using mid infrared observations.

Science Goals

Atmospheric retrievals are currently the best tools for characterizing the composition and structure of exoplanet atmospheres. Parameters such as the C/O ratio may trace the formation history of planets, and may be able to settle the debate between gravitational instability and core accretion formation models (Madhusudhan, 2012; Moses et al., 2013). From solar system observations, along with our own experience on Earth, we know atmospheres are constantly changing, and time series observations will open the door to investigation of dynamics and variability. Understanding the composition and chemistry of these atmospheres will also provide insight into the diversity - and similarity - between these systems. Clouds are poorly understood within our own solar system, and are certain to be present in the atmospheres of other worlds. Perhaps the most interesting prospect is uncovering novel features that have not yet been predicted, and will open the door to new avenues of exploration.

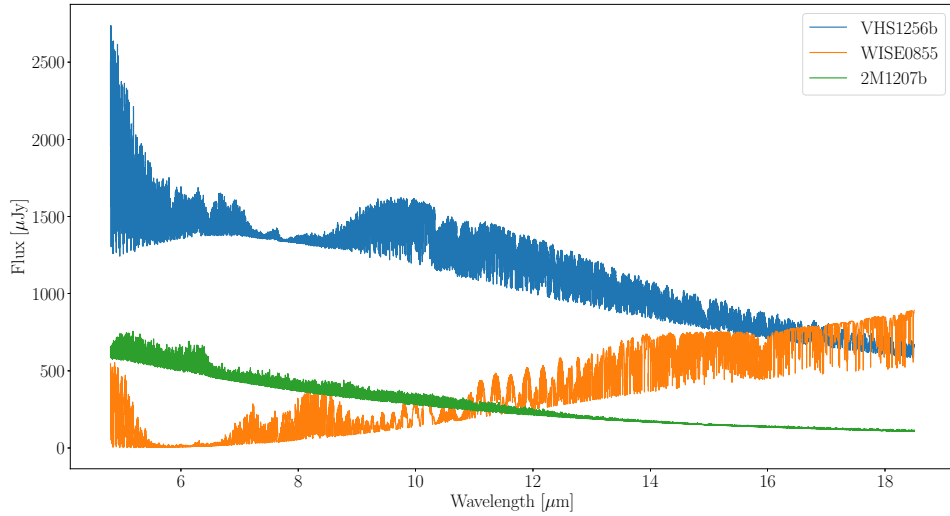


Figure 28: High resolution spectra generated by petitRADTRANS for each of the simulated targets.

For this work, we are primarily concerned with constraining the ability of the MRS to retrieve known input parameters. With simulated spectra from petitRADTRANS providing a ground truth, we can compare the results of retrievals over a range of fringing cases.

4.4 METHODS

Here we will outline how we generated our input spectra, and the procedure we used to perform our atmospheric retrieval.

4.4.1 Spectra Generation

We used petitRADTRANS in high resolution, line-by-line mode in order to calculate a spectrum that can be passed as input to MIRISIM. All three input spectra used are shown in Fig. 28. The parameters chosen for each target are given in table 7. All spectra cover a range of 4.8-18.5 micron in order to fully cover channels 1 through 3 of the MRS. Channel 4 is ignored due to photometric calibration issues and lack of sensitivity to faint sources.

The spectra generated by petitRADTRANS are in terms of the emitted flux and are in units of $\text{erg cm}^{-2} \text{ m}^{-2} \text{ s}^{-1} \text{ Hz}^{-1}$. MIRISIM requires the flux incident on the detector in units of μJy , so we convert the as

$$F_{inc}[\mu\text{Jy}] = 10^{29} \times F_{em} \times \left(\frac{R_{pl}}{d_{pl}} \right)^2. \quad (15)$$

The wavelength grid produced by petitRADTRANS is log-spaced, and we use the `spectres` python package (Carnall, 2017) in order to convert to a linear spaced grid with $R=12000$ at $4.0 \mu\text{m}$. This ensures the input spectrum will oversample the instrumental spectral resolution by a factor of at least 4 across the whole wavelength range.

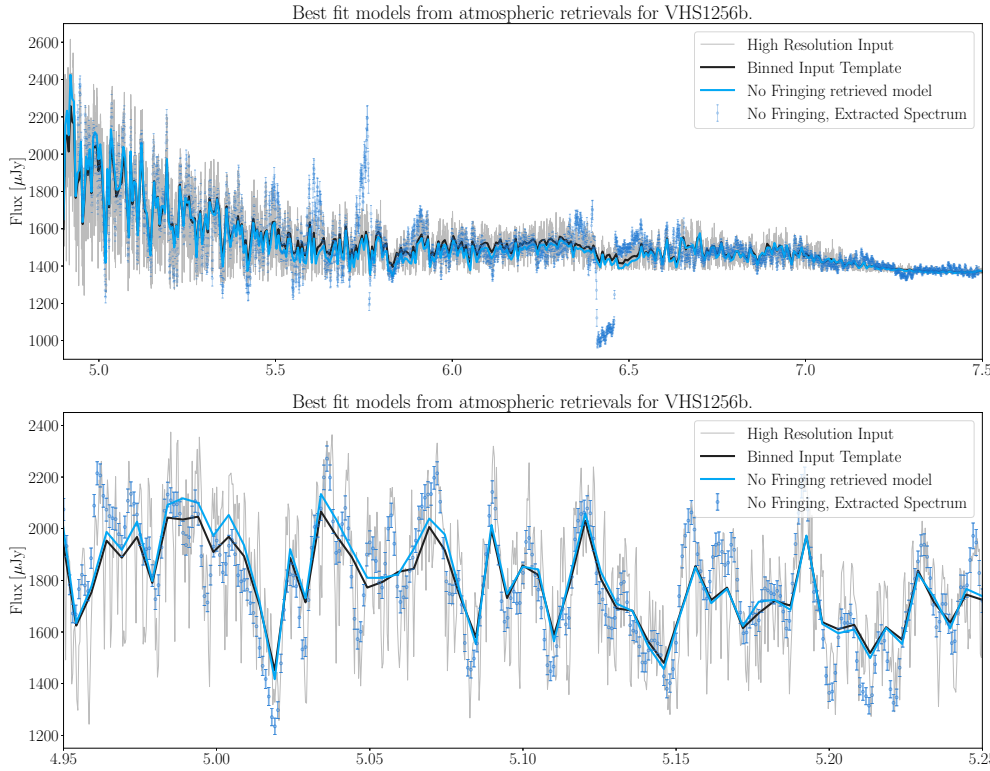


Figure 29: The extracted 1D spectrum for VHS1256b with no noise and no fringing applied compared to the input template and the best fit model from a Channel 1 atmospheric retrieval. This spectrum demonstrates the ability of the retrieval to accurately fit the data. It also shows several significant systematic effects at 5.7 and 6.4 micron, which are present at some level in all of the extracted spectra.

While it is possible to add a background term to a spectrum using MIRISIM, we chose not to use any background in order to improve our spectral extraction after processing with the JWST pipeline, with the understanding that errors from background subtraction will be negligible in actual data.

4.4.2 Atmospheric Retrieval Setup

Prior choice

The choice of priors is a consistent challenge when using a Bayesian framework. When performing a free-retrieval, uninformative priors must be chosen to allow the data to drive the posterior distribution. This can lead to unphysical solutions or combinations of parameters. The alternative is to use physically motivated priors, at the risk of missing unexpected phenomena.

We based our prior selection on the choices made in (Mollière et al., 2019). We use an uninformative uniform distribution on the temperature parameters, as well as on the log of abundance, gravity and pressure parameters. Uniformly drawing from the log of the parameters allows for better coverage of the very large parameter space (from 10^{-15} to 10^0 in each of the fractional

Parameter	Prior	Constraints
$\log \gamma$	$\mathcal{N}(0, 2)$	
T_{int}	$\mathcal{U}(0, 3500)$	
R_{pl}	$\mathcal{U}(0.01, 2.0)$	
κ_{IR}	$\mathcal{U}(0, 1)$	
$\log g$	$\mathcal{U}(1.8, 4.8)$	
$\log P_0$	$\mathcal{U}(-6, 2)$	
$\ln(X_i)$	$\mathcal{U}(-18, 0)$	$\sum X_i < 1$

Table 8: Prior choices for atmospheric retrievals using the standard Guillot profile. $\mathcal{U}(a, b)$ is a uniform distribution from a to b . $\mathcal{N}(\mu, \sigma)$ is a normal distribution. T_{int} corresponds to the effective temperature of an object in K, while R_{pl} is the planet radius in Jupiter radii. For free floating objects, T_{equ} is fixed to 2.7K. Pressures are in bar.

abundances). For the opacity parameters γ, δ and α we use a normal distribution centered around the expected value.

Trial runs showed that the posterior distributions for these parameters are not driven by the priors. Our prior choices and the ranges over which they cover are given in table 8.

Validation

We ran a retrieval with all of the noise and nonlinearity sources turned off in MIRISIM in order to validate our retrieval tools and to demonstrate the results of an ‘ideal’ correction. This was performed using VHS1256b as the input template, and only Channel 1 was used. While the retrieved abundances remained, the best fit model provides a much closer match to the input spectrum. This is shown in Fig. 29, with the best fit model plotted over the input model as well as the extracted spectrum. The best fit model closely follows the binned input spectrum across Channels 1A and 1B, and produces a significantly improved log-evidence of -6.99×10^3 . In Channel 1C however, it begins to deviate from the input model. This allows us to be reasonably confident that the retrieval is being performed accurately, and the Bayesian evidence provides a useful goodness-of-fit metric.

Name	Live	Wlen [μm]	Fringing	T_{int} [K]	R_{pl} [R_j]	C/O in	C/O ret
VHS-1256b	1500	5–7.5	No	684 ± 0.1	1.80 ± 0.0004	2.95	0.565 ± 0.003
	1500	5–7.5	Yes	833 ± 1	1.44 ± 0.004	2.95	3.17 ± 0.18
	10000	5–18	No	734 ± 0.3	1.65 ± 0.001	2.95	0.55 ± 0.03
WISE0855	1500	5–7.5	No	235 ± 1	1.24 ± 0.004	0.565	0.554 ± 0.03
	400	5–7.5	Yes	218.4 ± 0.02	2.5 ± 0.0003	0.565	0.40 ± 0.04
	400	5–18	No	234 ± 1.15	1.05 ± 0.02	0.565	0.20 ± 0.37
2M1207b	800	5–7.5	No	1186.9 ± 0.3	0.083 ± 0.0002	0.647	0.87 ± 0.7

Table 9: Summary of atmospheric retrievals.

4.5 RESULTS

Numerous atmospheric retrievals were run in order to examine the effects of fringing on parameter retrieval, as well as to better understand how to use the MRS to study atmospheres. We will discuss the findings for each of the three targets of interest individually before discussing the effects of fringing on the outcome of the study. The full posterior distributions are included in appendix A.3.

4.5.1 VHS-1256b

We ran a set of three retrievals for VHS-1256b. Two of these used data only from Channel 1, either with point source fringing or no fringing applied. The third retrieval was covered the full wavelength range from 5–18 micron, but no fringing was applied to the data. These retrievals also varied in the number of live points used, as summarized in table 9. We found that the number of live points did not significantly impact the precision with which the parameters of interest could be retrieved. However, the sampling density was improved at the cost of an approximately linear increase in computational time with the number of live points used.

All of the retrievals significantly underestimated the internal temperature of VHS1256b and overestimated the radius, with posteriors shown in Fig. 30. As expected from the Stephan-Boltzmann law the temperature and planet radius are strongly anti-correlated, though both parameters are biased from their true values. The full posteriors for the structure parameters for the Channel 1 case without fringing are shown in Fig. 32. Contours are set at the 50%, 95% and 99% coverage levels for all marginal plots. As many of these parameters are not physical in nature, their absolute values are not relevant, and the pressure-temperature profile itself provides a better figure of merit for the success of the retrieval. Fig. 31 shows the retrieved pressure-temperature profiles as compared to the input profile. The computed error on the retrieved profiles are smaller than the line width. The input profile is computed using the standard Guillot profile, and is isothermal from about 0.1 bar due to the choice of κ_{IR} and absorption from abundant species such as water and methane in the infrared. This is successfully retrieved if the standard Guillot profile is used, albeit at a lower internal temperature. An inversion is found if the modified profile is used in the retrieval, rather than simplifying to the standard profile. The simplest physically motivated

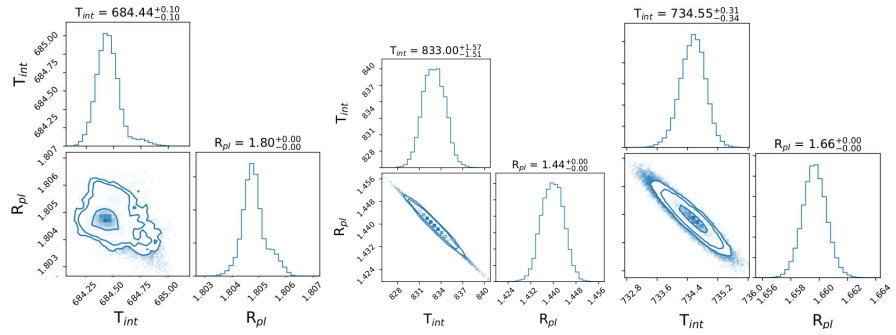


Figure 30: Interior temperature and planet radius posteriors for VHS-1256b. As expected, these parameters are highly anti-correlated: a higher temperatures and larger radii both result in increases in the overall luminosity of the planet. The true value of both parameters (900 K, $1.29 R_J$) falls outside the displayed distributions. **Left:** Channel 1 only, with no fringing applied. **Center:** Uncorrected point-source fringing was applied. **Right:** Full spectrum without fringing.

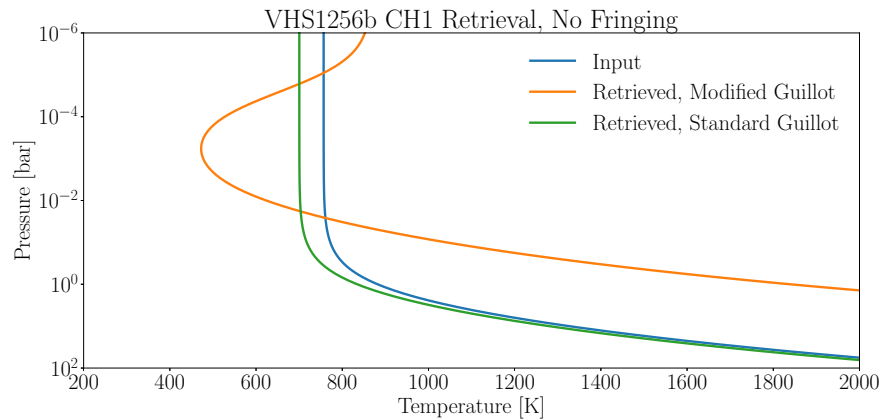


Figure 31: Pressure-Temperature profile for VHS-1256b, using the CH1 spectrum with no fringing or correction applied. Using different P-T profiles for the retrieval results in significant differences from the input profile. In the case where the underlying profile is unknown, multiple profiles should be compared.

pressure-temperature profile should be used in future retrievals, so as not to identify unphysical features in the atmospheric structure. Note that this may not be the Guillot profile and that other parameterizations should be considered.

To retrieve the atmospheric composition we retrieved abundances for 8 species for VHS-1256b: CO, H₂O, CH₄, NH₃, CO₂, H₂S C₂H₂ and TiO. These cover the primary components of the input atmosphere, while H₂S was included to examine how the retrieval would treat a species that isn't present. Figures 33, 34 and 35 show the posterior distributions for the Channel 1 without fringing, Channel 1 with fringing and full spectrum cases respectively. The Channel 1 case without fringing was the only retrieval to identify species at the correct abundance to within the computed margin of error. This is due both to bias in the retrieved posteriors and the narrow width of the distributions. However, although outside of the computed error bars, the retrievals

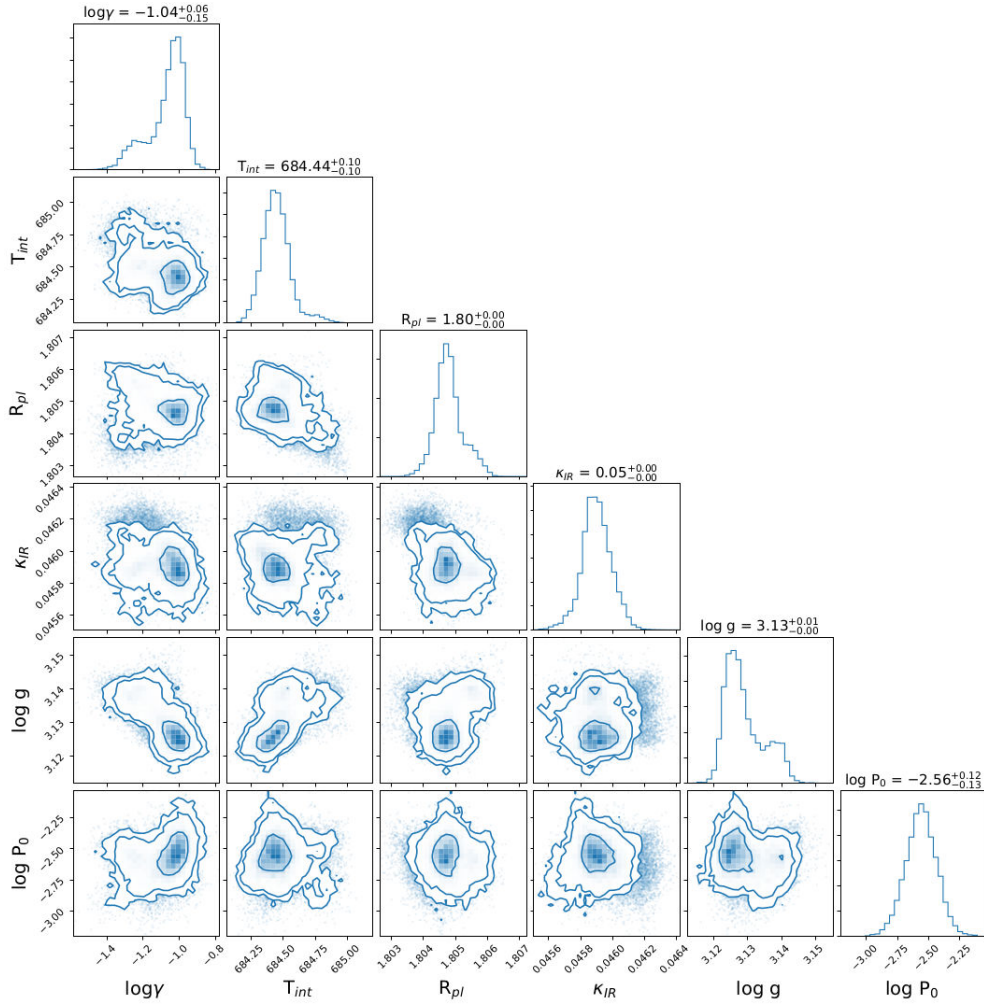


Figure 32: Posterior distributions for the nuisance parameters of VHS-1256b, no fringing case and using the standard Guillot profile, using only Channel 1. As most of these are non physical parameters, the P-T distribution provides a better metric for determining whether the atmospheric structure has been retrieved as opposed to specific parameter values.

produced order of magnitude estimates for water and methane. CO₂ was found to be the most abundant component of the atmosphere, making up 74% of the overall composition in the Channel 1, no fringing case. Only the Channel 1 case with fringing found the CO₂ to within margin of error, though the retrieved value is three orders of magnitude lower than the true value. As it is only a trace gas, a such wide posterior distribution is expected. The results for all of the retrievals are tabulated in table 10.

We find that several species are correlated, including water and methane, water and H₂S and methane and H₂S. Water and methane both share deep absorption features at similar wavelengths, contributing to similarities in the final emission spectrum. Hydrogen sulfide contributes primarily between 6 and 10 micron, where broadband absorption from the other two species is strongest. This likely led to incorrect abundances for all three species, as H₂S was found to contribute over 1% of the atmospheric composition in all three retrieval cases. Future retrievals should use an self-consistent equilibrium chemistry model in order to verify that such results are physically valid.

H_2S does not cross correlate with the spectral model as shown in Chapter 3, and such methods could provide a cross-check for verifying the presence of a given molecular species.

To summarize the composition and link our results to formation processes, we computed the mass fraction C/O ratio for each of our retrievals, shown in table 9. The error on the C/O ratio was found by using the 1σ errors on each of the retrieved abundances, and adding the relative C and O errors in quadrature. For VHS1256b we found that we could not accurately retrieve the input C/O ratio. This is likely due to the large abundance of H_2S affecting the retrieved abundances for water and methane, in turn impacting the C/O ratio. Although not explored in this work, it is possible to parameterize petitRADTRANS using the C/O ratio and metallicity as opposed to single species abundances, which will likely produce more accurate results when searching for this quantity.

With the structure and composition identified we can now compare the best fit retrieved models, as well as the emission contribution function to identify which atmospheric layers we are examining. The log-evidences for each model presented in Fig. 36 are similar: -8.78×10^4 , -9.96×10^4 and -1.09×10^5 for the no fringing, Channel 1 fringing and full spectrum retrievals respectively. While it is difficult to compare the evidence for different data sets, we do note that the no fringing case resulted in a better fit to the data than in the fringing case. At short wavelengths, we find that the Channel 1 fringe-free case fits the data very well, particularly compared to the point source case. However, both of the other retrievals attempt to fit a systematic-induced feature at $6.5 \mu\text{m}$. At longer wavelengths we find that this model deviates from the input spectrum, and that the full spectrum model provides a better fit beyond $10 \mu\text{m}$. All of the model overestimate the flux prior to the $10 \mu\text{m}$ absorption feature, possibly leading to the overestimates in abundance of species such as methane, water and carbon dioxide, all of which have absorption lines around this wavelength. In general, we find that the Channel 1, fringe-free case provides the best fit to observed absorption features, while the full spectrum retrieval provides a better fit to the continuum. The model found in the fringing case displays significant deviation from the input spectrum. The emission contribution function shown in Fig 37 shows the atmospheric pressures probed at each wavelength. The function shown is for the full spectrum retrieval with no fringing. We see that deeper levels of the atmosphere are the emission source between 8 and 12 micron, while strong absorbers raise the photosphere at shore wavelengths. In the case of a cloudy atmosphere, this will provide critical information for probing particle sizes and cloud base altitudes. Even in a clear atmosphere there is no emission from below 1 bar.

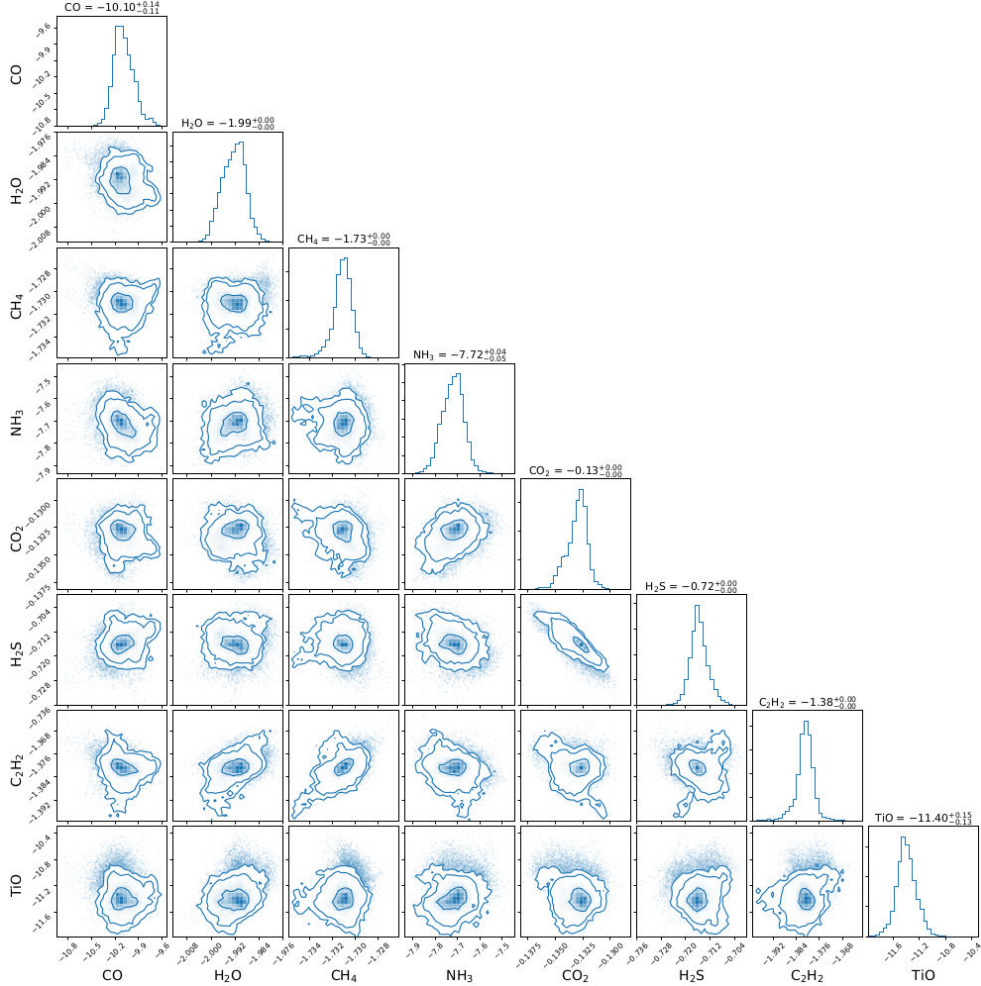


Figure 33: Posterior distributions for species abundances in VHS1256b, in the fringe-free case using CH1 data. While several species were successfully retrieved, the very high abundance of H₂S, which is not present in the atmosphere and whose absorption features fall mostly outside of CH1, demonstrates the need for wide wavelength coverage to correctly identify the presence of a given species. There also exists significant correlation between H₂O and CH₄, with some additional correlation to H₂S, which has led to incorrect abundance measurements.

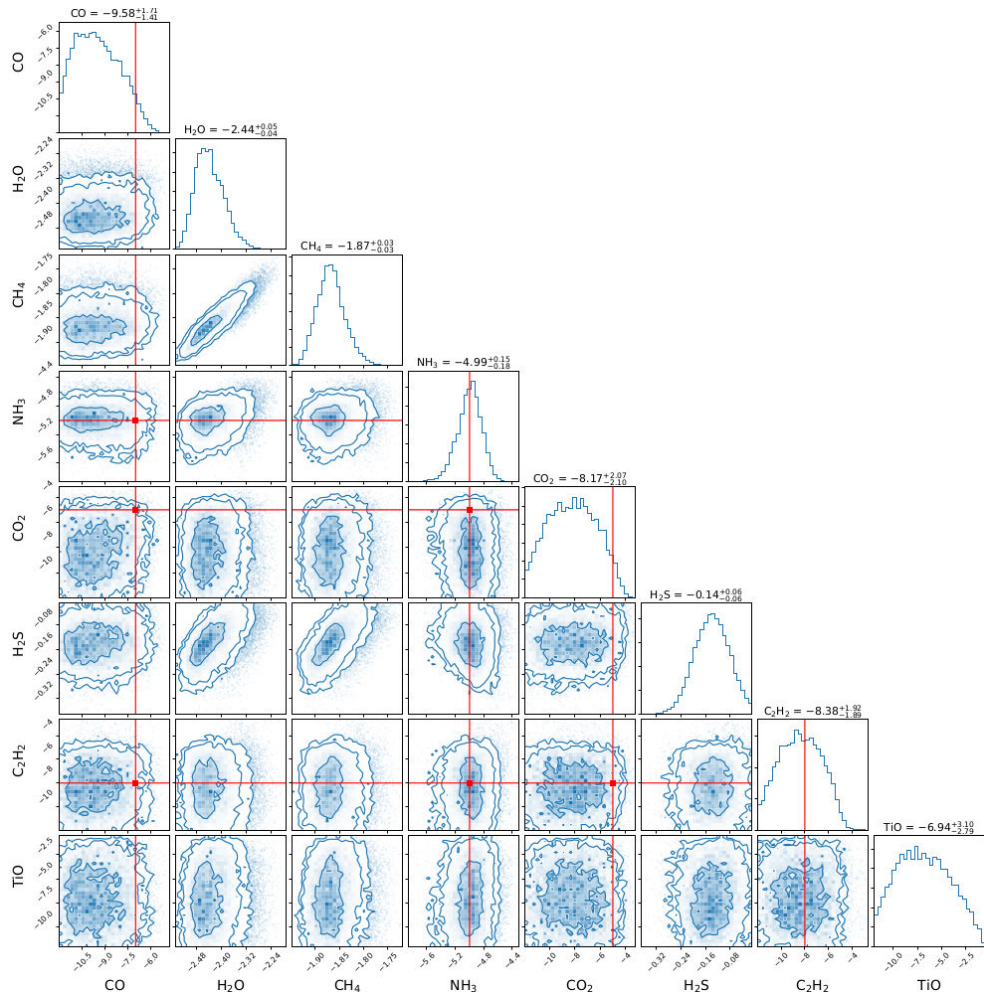


Figure 34: Posterior distributions for species abundances in VHS1256b, in the uncorrected point-source fringing case using CH₁ data.

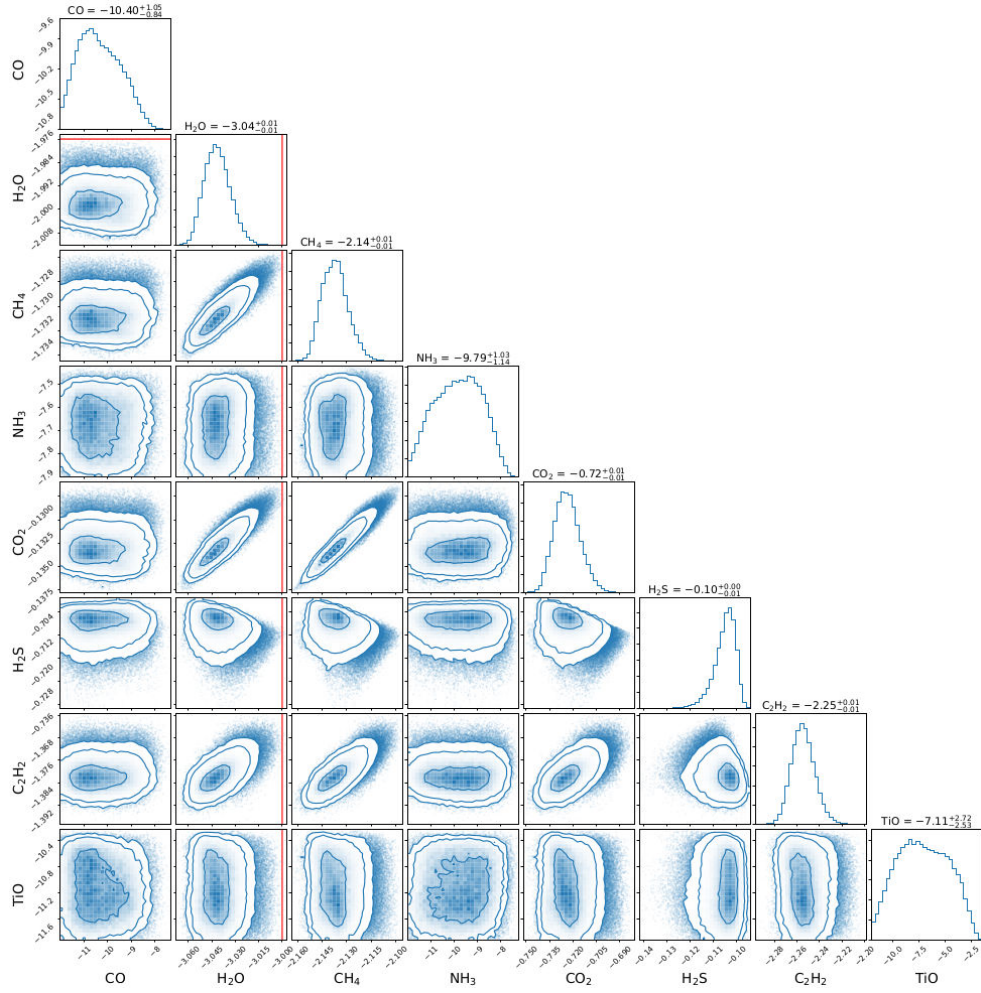


Figure 35: Posterior distributions for species abundances in VHS1256b, in the no fringing case using the full spectrum.

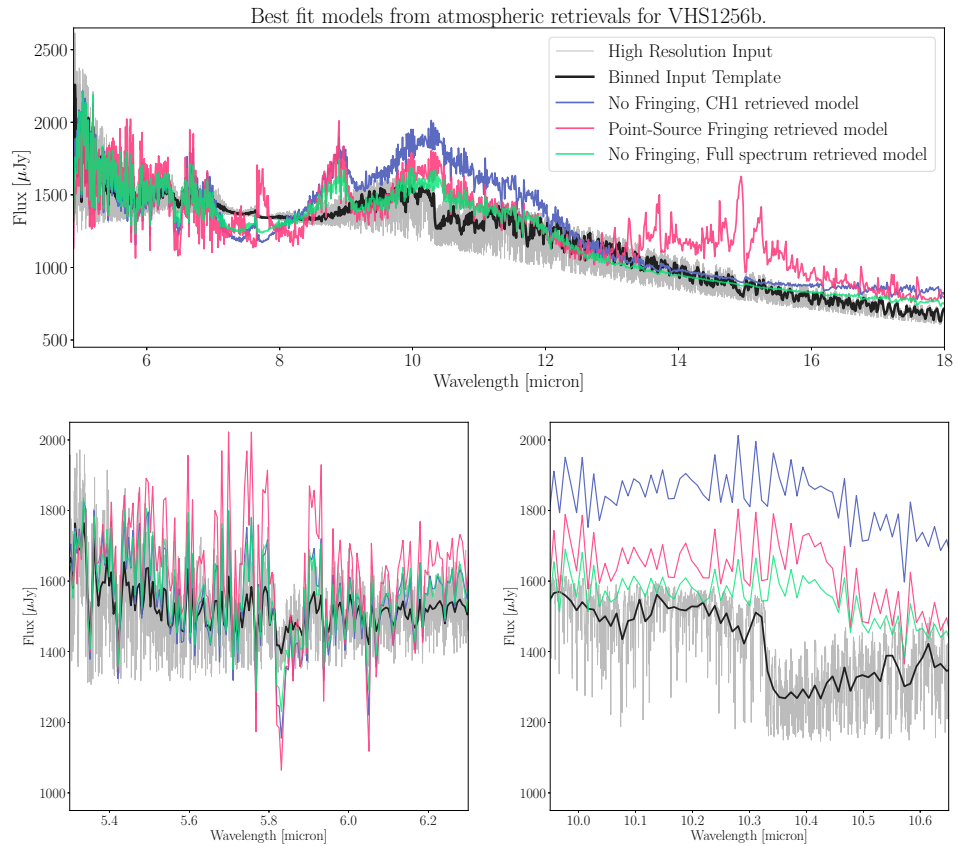


Figure 36: Best fit models for VHS-1256b in three different wavelength regimes.

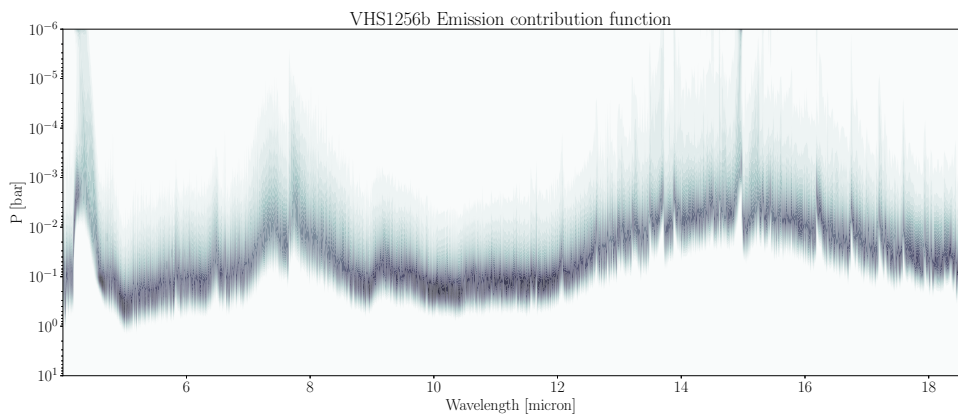


Figure 37: Emission contribution function for the retrieved spectrum of VHS-1256b, using the full spectrum without fringing.

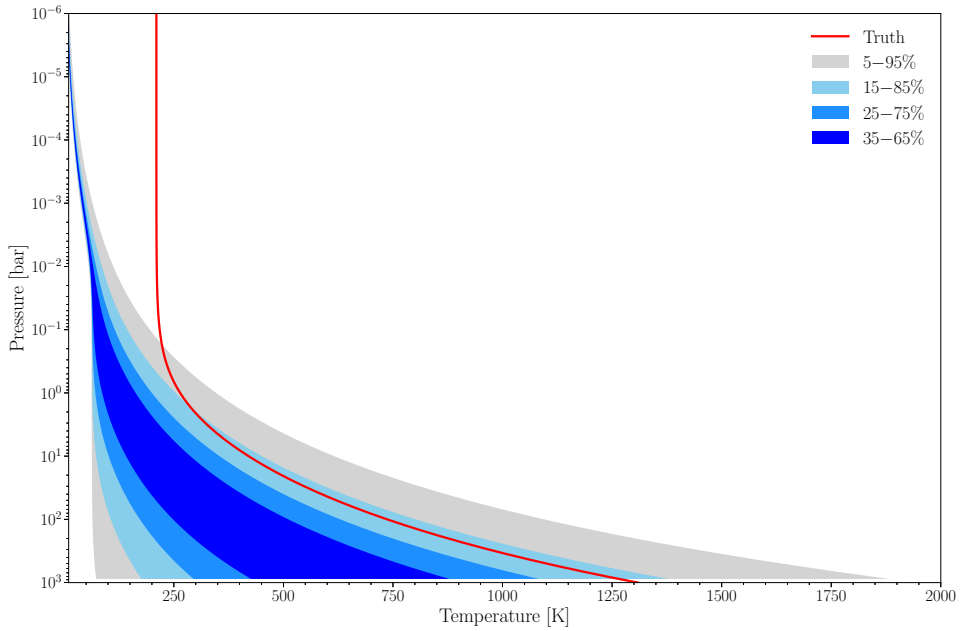


Figure 38: Pressure-temperature profile for WISE o855.

4.5.2 WISE 0855

The cold temperatures and prominent molecular features make WISEo855 an excellent candidate for a retrieval study in the mid infrared. We performed a series of three retrievals on WISEo855, following a similar setup as for VHS1256b. We again consider two retrievals for Channel 1, both the fringing and non-fringing case. The third case is the non-fringing, full spectrum retrieval. We will focus our discussion on the Channel 1, no fringing case. The full spectrum and fringing retrievals were performed with only 400 live points, leading to less accurate parameter retrieval and highly correlated abundances. In the fringing case several of the posteriors were limited by the priors, and do not well reflect the true parameters. The posteriors for the full spectrum retrieval and the retrieval including fringing are included in appendix A.3.

With strong molecular features, the retrieval performed better for WISEo855 than for the other two targets. Posterior widths and errors computed by the retrieval present a more realistic picture of the uncertainty in measurements of the parameters. Consider the pressure-temperature profile in Fig. 38. A modified Guillot profile was used for the Channel 1 retrieval. From 0.01 bar to 10 bar the true P-T profile falls within the 15%–85% confidence interval. As the pressure decreases, the profiles diverge, and the retrieval did not identify the isothermal temperature structure. We note that the input profile is not a realistic model of a brown dwarf atmosphere, and the retrieved profile likely presents a better model of a self-luminous object. The parameters retrieved in order to compute this profile, shown in Fig. 39, match with expectations. The α parameter is centered at 0, thus reducing the modified Guillot profile to a standard profile. This also makes P_{trans} uninformative with no impact on the profile, and this is reflected in the uniform posterior distribution. While the remaining parameters, including the temperature

and radius, exclude the true values to within 2% due to narrow posterior distributions, they fall within 10% of the expected value.

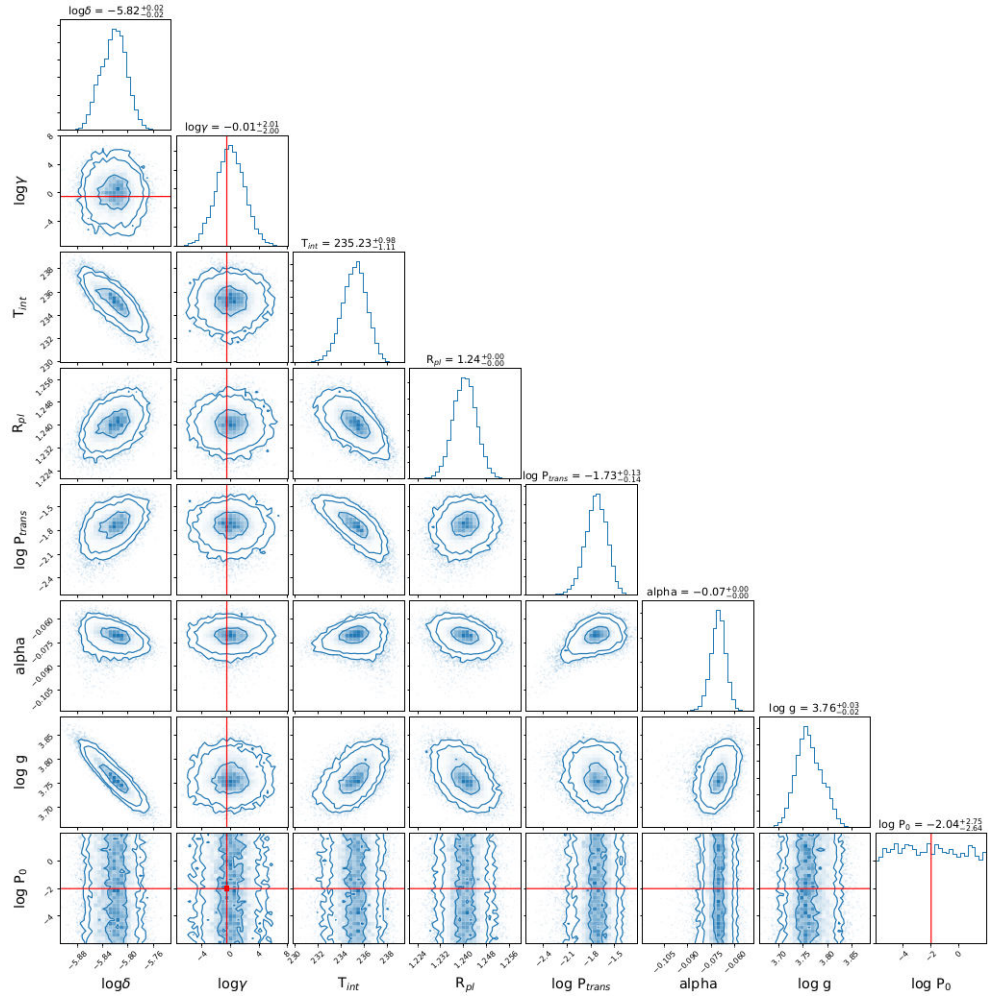


Figure 39: Nuisance parameter posterior distributions for WISEo855 in the Channel 1, no fringing case.

The composition of the atmosphere is also well retrieved. Ammonia creates the strongest absorption features, and is retrieved to within the margin of error at a mass fraction of 0.0026 ± 0.0001 . Other strongly present species including water and methane are found to be the next most abundant molecules. Carbon monoxide presents a false positive detection though, as it is present only at the 10^{-15} level in the atmosphere, but is measured at $10^{-4.67}$. A similar false positive was found using the cross correlation technique in Chapter 3. In a cold atmosphere the CO spectrum is largely featureless, and it is not expected to present in large quantities in such an atmosphere in equilibrium. This suggests that physically motivated species selection, or self consistent modeling is necessary to validate the presence of any given measured species. As carbon and oxygen are equally present in CO, this did not affect the C/O ratio, which was found to be 0.554 ± 0.03 , within 2% of the true value of 0.565. The narrow posterior distributions nevertheless exclude the true value at the 3.7σ level.

Due to the strong ammonia features and well retrieved abundance, the best fit model follows the input spectrum remarkably well. This is reflected

in the log evidence of -1.73×10^4 . Fig. 42 shows that the depth of the emission is strongly dependent on the nitrogen absorption. The pressure is somewhat lower than in the case of VHS1256b, likely due to stronger overall absorption. The large scale features centered around 7 and 14 micron trace the continuum of the CO emission spectrum, and it is possible that this structure is due to the large retrieved abundance.

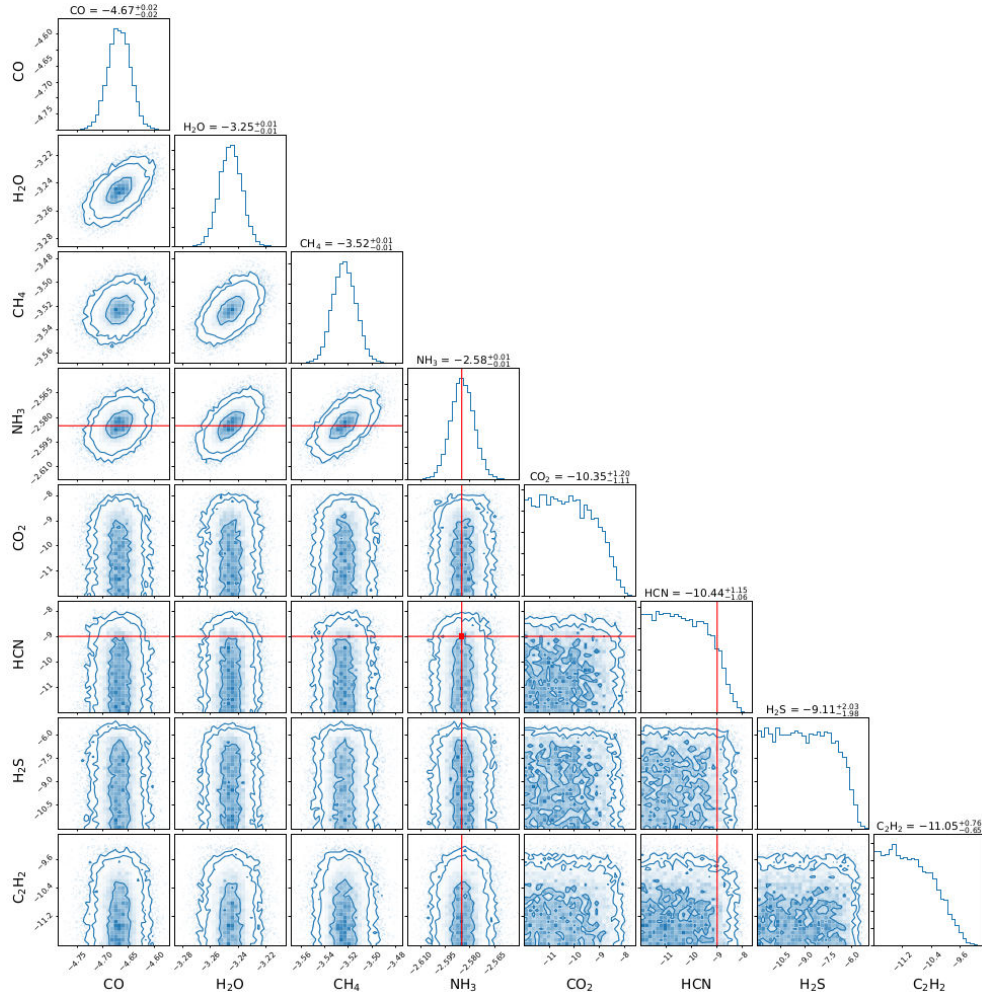


Figure 40: Abundance posterior distributions for WISE0855 in the Channel 1, no fringing case.

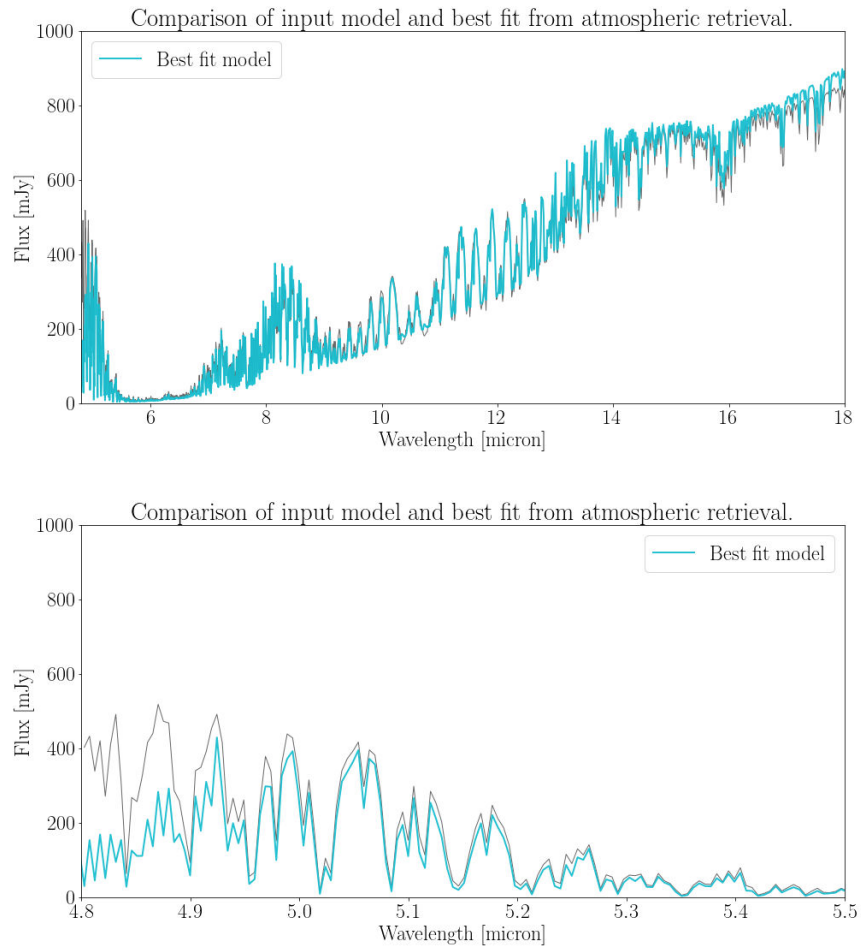


Figure 41: Best fit model for WISE0855. No fringing was applied, and only Channel 1 data was used.

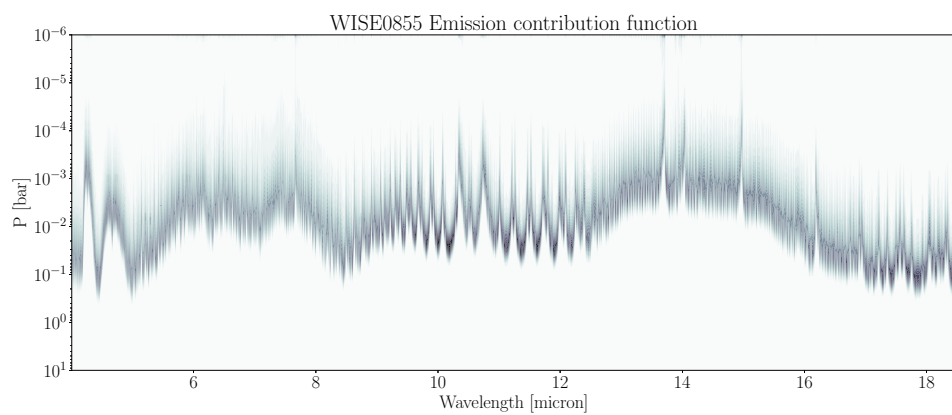


Figure 42: Emission contribution function for WISE0855.

4.5.3 2M1207b

The retrievals for 2M1207b performed the worst out of all trials. We ran the retrieval on Channel one data without fringing. Systematics in the spectrum led to difficulties in fitting models, while the lack of significant absorption features makes identifying species difficult. Many of the retrieved species were very strongly correlated to each other, as well as to the infrared opacity κ_{IR} . The temperature was underestimated at 1186 K, but the radius was even more discrepant at $0.08 R_J$. We present the posterior distribution in Fig. 43 for reference, but cannot make further conclusions from these results.

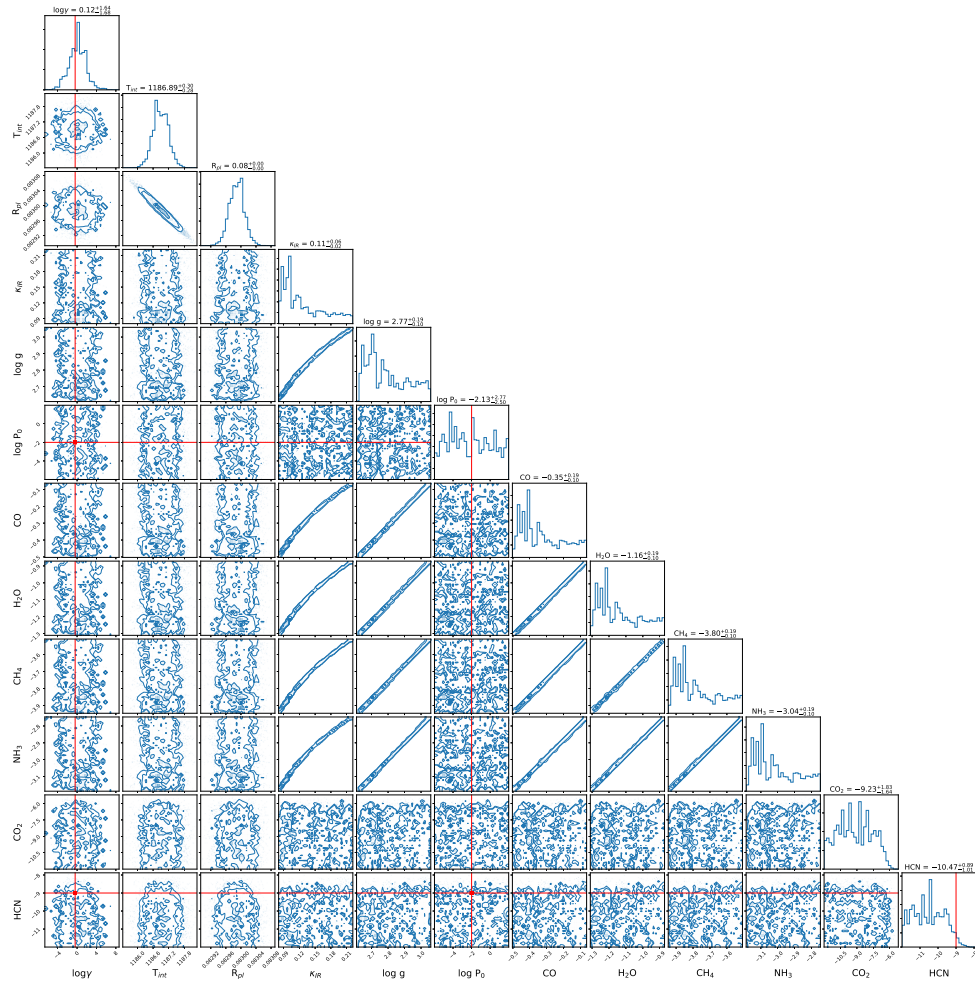


Figure 43: Posterior Distributions for 2M1207b.

Name	Wien [μm]	Fringing	H_2O	CH_4	NH_3	CO	CO_2	H_2S
VHS-1256b	Truth		1×10^{-3}	3×10^{-3}	1×10^{-5}	1×10^{-7}	1×10^{-5}	0.0
	5-7.5	No	$1.02 \pm 0.001 \times 10^{-2}$	$1.86 \pm 0.0002 \times 10^{-2}$	$1.9 \pm 0.2 \times 10^{-8}$	$8 \pm 2 \times 10^{-11}$	$7.4 \pm 0.01 \times 10^{-1}$	$1.9 \pm 0.01 \times 10^{-1}$
	5-7.5	Yes	$3.6 \pm 0.3 \times 10^{-3}$	$1.3 \pm 0.1 \times 10^{-2}$	$1.0 \pm 0.3 \times 10^{-5}$	$0.3 \pm 1.5 \times 10^{-8}$	$0.08 \pm 1 \times 10^{-6}$	$7.4 \pm 0.7 \times 10^{-1}$
WISE0855	Truth		4.6×10^{-4}	2.6×10^{-4}	2.6×10^{-3}	1×10^{-15}	1×10^{-14}	0.0
	5-7.5	No	$5.6 \pm 0.1 \times 10^{-4}$	$3.0 \pm 0.1 \times 10^{-4}$	$2.6 \pm 0.1 \times 10^{-3}$	$2.1 \pm 0.1 \times 10^{-5}$	$0.5 \pm 5 \times 10^{-9}$	$0.7 \pm 7 \times 10^{-8}$
	5-7.5	Yes	$2.1 \pm 0.1 \times 10^{-2}$	$4.7 \pm 0.1 \times 10^{-3}$	$2.07 \pm 0.05 \times 10^{-2}$	$0.25 \pm 1 \times 10^{-8}$	$0.04 \pm 1 \times 10^{-6}$...
2M-1207b	Truth		5×10^{-3}	1×10^{-6}	1×10^{-7}	1×10^{-2}	1×10^{-3}	0.0
	5-7.5	No	$7 \pm 2 \times 10^{-2}$	$1.6 \pm 0.5 \times 10^{-4}$	$9 \pm 4 \times 10^{-4}$	$4.5 \pm 3 \times 10^{-1}$	$0.05 \pm 3 \times 10^{-8}$...
	5-18	No	$9.1 \pm 0.6 \times 10^{-4}$	$7.2 \pm 0.2 \times 10^{-3}$	$0.2 \pm 1 \times 10^{-9}$	$0.4 \pm 1.0 \times 10^{-10}$	$1.9 \pm 0.1 \times 10^{-1}$	$7.9 \pm 0.2 \times 10^{-1}$

Table 10: Retrieved mass fraction abundances for a selection of retrieved species. The log of these values is the retrieved parameter, where applicable the stated error is the 1σ error in log space. This error can result in abundances below zero. For the lower bound the log error in the posterior plots should be used.

4.5.4 Fringing Comparison

We begin by comparing the results of different fringing cases, using VHS-1256b as a template. The first set of retrievals use only Channel 1 data from 4.9-7.5 μm , as point source fringe flats have only been generated for this wavelength range. We compare the case of a retrieval with no fringing added to the spectrum to having an on-axis point-source derived fringe flat applied and an extended-source fringe flat used for correction. The case of an extended source fringe flat was not used, as the correction is near ideal, and it is well represented by the no-fringing case. The effects of residual fringe correction on the retrieval was not examined.

We found that point source fringing did not result in a significant reduction in precision or accuracy of the retrieval results. While it may have an impact, other sources of error led to far greater variation in retrieval results. Parameters were not retrieved to within the computed margin of error. With WISE 0855, the fringing case resulted in a failure of the retrieval, pushing the posteriors to the edges of the priors. For the abundance measurements for VHS-1256b, the point source fringing case provided more accurate estimates than in the no fringing case, as shown in table 10. The retrieved temperature and radius of VHS-1256b were also less discrepant in the fringing case than in the non fringing case. However, we cannot attribute the improved accuracy of the retrieval to the addition of fringing. These results were inconsistent across multiple trials, and the posteriors presented in Fig. 34 represent the best retrieved parameters.

Differences in processing, noise, and choices of retrieval hyperparameters will all significantly impact the results. We cannot conclude that atmospheric retrievals provide a good metric by which to measure the effects of fringing in the MIRI MRS. At the present, fringing is also not the limiting factor in improving the precision of atmospheric retrievals.

4.5.5 Discussion

The three targets chosen represent a relatively diverse selection of substellar objects, yet there are similarities across all of the retrievals. Temperatures are uniformly underestimated and the radii overestimated, regardless of the choice of pressure-temperature profile parameterization. There are correlations between these parameters and the abundances of several species, including water and methane. These abundances are also not retrieved to within the margin of error. The mechanism for these systematic biases is unclear, and should be explored through a series of retrievals examining the impact of individual species on the temperature and radius. Additional structure parameterizations should be explored in order to determine if the temperature and radius offsets are due to the chosen model, or to sampling effects. A similar effect has been noted for transmission spectroscopy in an upcoming study from (MacDonald et al., 2020), though their mechanism is not necessarily applicable to self-luminous objects.

Posterior widths and errors are systematically underestimated. Given that most parameters can be retrieved to within 10% at best, the narrow distributions does not accurately represent the variance in the retrieved parameters.

This is likely due to the small ($\approx 1\%$) errors associated with the extracted JWST data, as well as the very large number of data points. It does not reflect the large systematics that dominate the variance in the spectrum. True error propagation through the JWST pipeline is unlikely to resolve this issue, as the relative errors associated with each spectral point will be of the same order as the photometric errors used in this work. In order to justify such small errors, calibration must be improved such that systematic effects are at the same level or lower as the various noise sources impacting the data.

False detections of species are another common feature to our retrievals. These tend to be species without significant absorption features, and are generally correlated with atmospheric profile parameters, as well as the abundances of common molecules. These species are also not expected at the temperatures and pressures associated with the objects that they are observed in. Due to these false detections and their potential impact on the abundances of other species, we found that the C/O ratio could not be accurately retrieved using retrievals on species abundance. Model parameterization using the C/O ratio and metallicity may be necessary to measure this quantity. For VHS-1256b, the use of a cross correlation on the retrieved species would indicate that the species is not present in the spectrum. A self-consistent model would provide an additional check on such species, but constrains the possible atmospheres that can be measured. Presently disequilibrium models are too slow to be used in a retrieval, but may be necessary to validate the presence of retrieved species. The effect of individual species on the Bayesian evidence should also be examined in order to justify the inclusion of the species in the retrieval. Any single retrieval is insufficient for claiming an understanding of the atmospheric structure and composition. Retrievals using different models must be compared, and the results must be checked to ensure that they are physically valid.

We must also acknowledge that the results presented here will not reflect the observed spectra from these particular JWST targets. Clouds are certain to impact the spectra, and add an additional layer of complication and uncertainty to the retrieval process. These objects will vary in time, and will have 3D features that impact observations. Therefore we caution that this work is very much an idealization, and represents somewhat of a best case scenario for the retrieval process for the MIRI MRS.

5 | DISCUSSION AND CONCLUSIONS

Astronomy is a constantly evolving field. With a new era of infrared observations fast approaching, we set out to examine how instrumental effects will limit our scientific capabilities, and to explore atmospheric retrievals in the mid infrared. Keeping these goals in mind, we characterized the effects of fringing on spectral extraction in the MIRI MRS. We also selected targets from the Early Release Science and Guaranteed Time Observation programs for JWST to perform realistic atmospheric retrievals on emission spectra as observed with the MRS. To accomplish this we developed an analysis pipeline to simulate, process and examine synthetic MRS observations, which can easily be used for future observing proposals or data reductions. We also adapted the current retrieval method using the petitRADTRANS atmospheric modeling code to use the Nested Sampling method. This provides an improvement in the exploration of multimodal posterior distributions and direct computation of the Bayesian evidence for a model, in contrast to the current MCMC methods used.

5.1 SUMMARY OF RESULTS

5.1.1 Fringing in the MIRI MRS

In order to quantify the effects of thin film fringing in the detector layers of the MIRI MRS, we used cross correlations to compare the extracted spectrum with the input template. The current version of the instrumental simulator, MIRISIM, uses a fringe flat derived from a spatially extended source, and the JWST Pipeline uses the same fringe flat to correct for this effect. However, the extended source does not provide a realistic model of fringing for point sources. We implemented a routine to substitute a point source derived fringe flat into MIRISIM, using a large set of fringe flats to cover the detector plane. We then corrected this point source fringing using the extended source fringe flat currently used in the JWST Pipeline, as well as using residual fringe correction to filter out fringing frequencies. We found that the current implementation between MIRISIM and the pipeline provides an optimistic estimate, essentially identical to the case with no fringing. The correction performed less well on point source fringing, decreasing the signal to noise of the cross correlation peak by 10% if the point source is located in the center of the detector plane, and 20% if the source is located off-axis. The residual fringe correction results proved inconclusive, though may depend on the input signal strength. There is an incompatibility between the RFC and the dark current subtraction step in the JWST Pipeline.

To emphasize the importance of the point source fringing effect, we compared the extracted spectrum to molecular templates using the same cross

correlation procedure. As when correlated with the full input template, we showed that the current instrumental model will overestimate the SNR of a detection as compared to the more realistic point source fringe model. The reduction in SNR when using the point source model is substantial enough to move a species from a significant, $>5\sigma$ to a marginal detection.

Moving forward, point source fringing should be added to the instrumental simulator in order to provide users with more realistic synthetic datasets with which to test analysis tools and plan observations. Residual fringe correction requires further development in order to properly correct MRS data, though it has shown success in the past for Spitzer and Hubble. A more robust fringe correction must be developed in order to analyze MRS data. This may require additional calibration or commissioning data with the specific goal of characterizing this feature, but current corrections are inadequate for the science cases presented for JWST.

5.1.2 Effects of fringing on atmospheric retrievals

Fringing was found to not be a limiting factor for the accuracy of atmospheric retrievals. Systematic effects and hyper-parameter variation led to much larger disparity in the results. In the case of VHS-1256b, the retrieval using only Channel 1 data within uncorrected fringing led to the best retrieved parameters. We cannot conclude that atmospheric retrievals provide a useful measure of the impact of fringing in the MRS. Based on the cross correlation results, we recommend that any retrievals run on MRS data either do not attempt to correct for fringing, or use residual fringe correction. Poor fringing correction using an extended source fringe flat results in the largest deviation of the extracted spectrum from the known input.

5.1.3 Atmospheric retrievals with the MIRI MRS

All of the retrieval studies performed demonstrated the opportunities and challenges presented by using the MRS to study atmospheric physics and chemistry. Temperatures were systematically underestimated, and radii overestimated across all trials. In general abundances could not be constrained to within the retrieved margin of error. Retrievals on subsets of the full spectrum data (using Channel 1 only) found different compositions and temperatures than a retrieval over the full wavelength range.

However, while the parameter estimation might not find the correct values to a retrieved margin of error, they do provide insight into the atmospheres under investigation. For VHS-1256b internal temperature estimates ranged from 684 K to 833 K, compared to the true value of 900 K. The radius was overestimated at between 1.44 and $1.8 R_J$, compared to the $1.29 R_J$ input. The inclusion of hydrogen sulfide in the retrieval, but not in the atmosphere demonstrated the importance of validating retrieved atmospheres. It was retrieved at over 10% of the atmospheric composition in all cases, while not being present in the atmosphere at all. However, the estimates for water and methane were consistently within an order of magnitude of the true abundances of 0.1% by mass fraction. The C/O ratio computed from the retrieved

species did not reflect the input ratio. Using a model parameterization based on the C/O ratio and metallicity may provide a more robust estimate for this quantity.

WISE 0855 proved to be an easier target due to the strong ammonia absorption features in the simulated atmosphere. The temperature was consistently estimated at 235 K, while the radius varied from 1.05 to 1.24 R_J . The true values of these parameters were 250 K and 1.17 R_J respectively. The ammonia abundance was one of the few species retrieved to within the computed margin of error, at $0.26 \pm 0.01\%$ by mass fraction. Water and methane were within 20% of their input values. Carbon monoxide was overestimated, but due to a relatively featureless spectrum did not significantly impact the best fit model. Unlike VHS1256b, we were able to correctly compute the C/O ratio of 0.554 ± 0.03 . The comparison between the two objects demonstrates the necessity of having strong absorption features for the retrieval to produce accurate results.

A key finding of this work is the importance of validating the physicality of a retrieved atmosphere. Using self consistent equilibrium or disequilibrium models, the atmospheres must be checked in order to prevent false positive detections such as H₂S in VHS-1256b or CO in WISE 0855. In the case of VHS 1256b, we found that using a cross correlation would rule out the presence of H₂S, though this method did not prove useful for CO in WISE 0855 due to the lack of significant lines.

The variation in the retrieval results across different cases, and the systematic biases in temperature and radius emphasizes the necessity of using multiple tools in order to avoid model dependent effects. While this would not provide a guarantee that the correct parameter estimation will be correct in any individual retrieval, it would provide a more robust case for any repeatable parameter measurement.

5.2 DISCUSSION

5.2.1 Implications for GTO Observations

All of the targets will be observed to sufficient SNR given the proposed observing parameters. The wide spectral coverage of the MRS - particularly when combined with NIRSpec observations - will prove invaluable for constraining atmospheric parameters. However, we found that using the full spectrum did not necessarily improve the accuracy of the retrieval. We propose that retrievals should be performed on subsections of the data, particularly in regions where strong absorption features from a particular species are expected to be present. These should be compared to the retrieval using the full spectrum data. The current limitations of this work will likely be addressed by dedicated calibration, and hopefully will not present systematic issues for the on sky targets.

5.2.2 Caveats and Limitations

The conclusions and recommendations given here must come with certain caveats. All of the software used within this work are at varying stages of development, and are explicitly stated as being unready for public use. Thus there are still many open issues - particularly in MIRISIM and the JWST pipeline. In MIRISIM, there are particular issues with photometric calibration. While several of these effects have been noted and will be fixed in upcoming releases, others will inevitably remain. These effects include unusual spikes or drops across the spectrum, saturating detectors in the absence of a bright source, additional fringing components and potential interpolation issues. The JWST pipeline is also under development, and throughout this work we use version 0.15. Several of the pipeline steps - e.g. `ref_pix`, `jump_step` and `extract_1d_step` - are incomplete or have particular open issues for the MRS. Cube building is another source of concern, and the correlations introduced by this step are poorly understood. The extracted spectrum requires significant ad-hoc adjustment to resemble the input spectrum, a procedure which is not possible for an astronomical source. Atmospheric retrievals in particular rely on accurate spectral extraction, and all of the results presented here are likely to change as development continues.

Beyond software development issues, there are many more fundamental limitations within this work. (Barstow et al., 2020) provides a comparison of various atmospheric modeling and retrieval tools, demonstrating how different retrieval tools can produce different results on the same input. We used petitRADTRANS for both our spectrum generation and our retrieval code, and any inherent issues with this tool will be manifest in the results presented here. It will ultimately be necessary to use multiple tools to perform retrieval studies in order to generate robust results. Further still (Taylor et al., 2020) demonstrates the limitations of 1D models with the quality of data produced by JWST. 2D disk effects, variability and more will all greatly impact the spectra observed with the MRS, and a 1D model cannot capture the full 3D atmospheric physics present in nature. Finally, we ignore the presence of astronomical backgrounds, including the contamination from the host star of an exoplanet - thus neglecting one of the most significant challenges in exoplanet astronomy. Such issues are areas of ongoing research, and will present challenges for all atmospheric retrieval studies in the near future.

5.2.3 Future work

Going forward there are many improvements to be made to this work. Clouds are a universal atmospheric feature, and were neglected from the atmospheric retrieval study presented here. The mid-infrared will allow us to explore novel cloud features, potentially constraining particle size and composition through $10 \mu\text{m}$ observations. Variability studies will also be possible for both brown dwarfs and some exoplanets. The use of the tools developed here could prove useful in designing observations to maximize the capabilities of the MIRI MRS for exoplanet observations.

Extensive validation should be performed on the atmospheric retrieval code used here. From clouds to atmospheric chemistry to parameter selection, there are many significant challenges to overcome before the results of a retrieval are to be fully trusted. Quantitative metrics such as the Bayes' factor should be used to determine whether or not a given parameter should be included in the retrieval. Unfortunately performing a retrieval for each parameter becomes computationally expensive, which is the true limitation of all retrieval codes available today. Nevertheless, computational resources and software will continue to improve, allowing ever more detailed retrieval studies that will provide us the means to explore atmospheres of other worlds.

A

APPENDIX

A.1 EXTRACTED SPECTRA

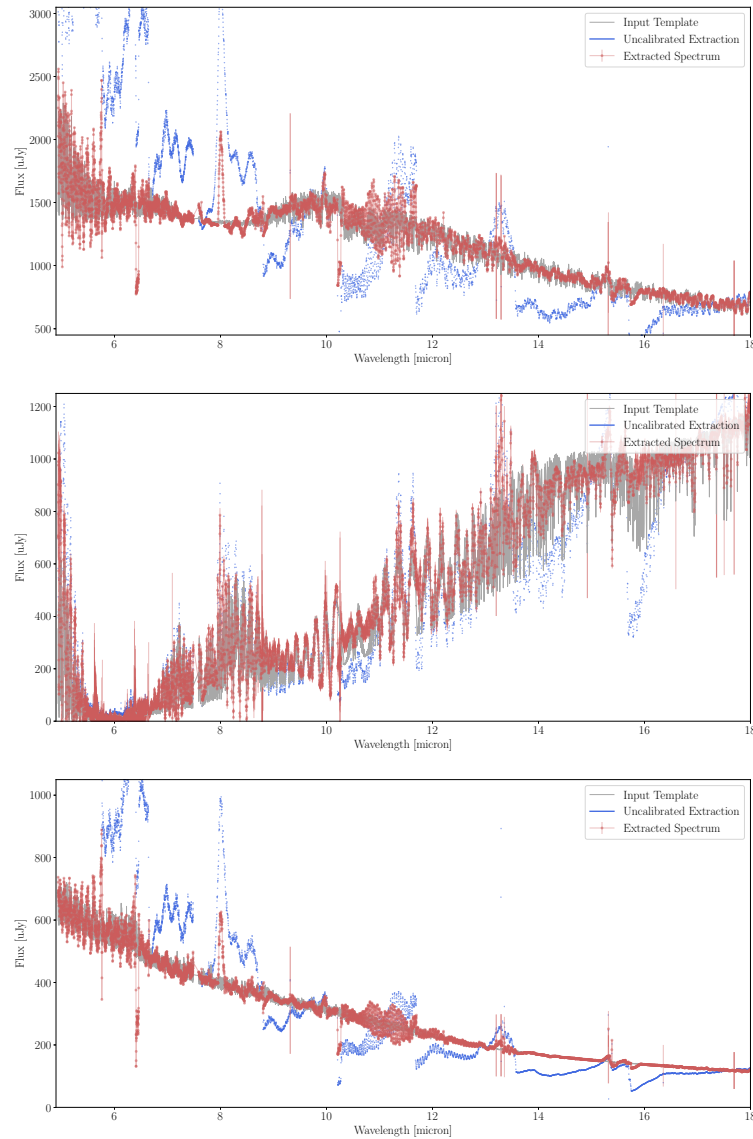


Figure 44: Extracted spectrum without fringing for VHS-1256b (top), WISE 0855 (center) and 2M1207b (bottom).

A.2 CROSS CORRELATIONS

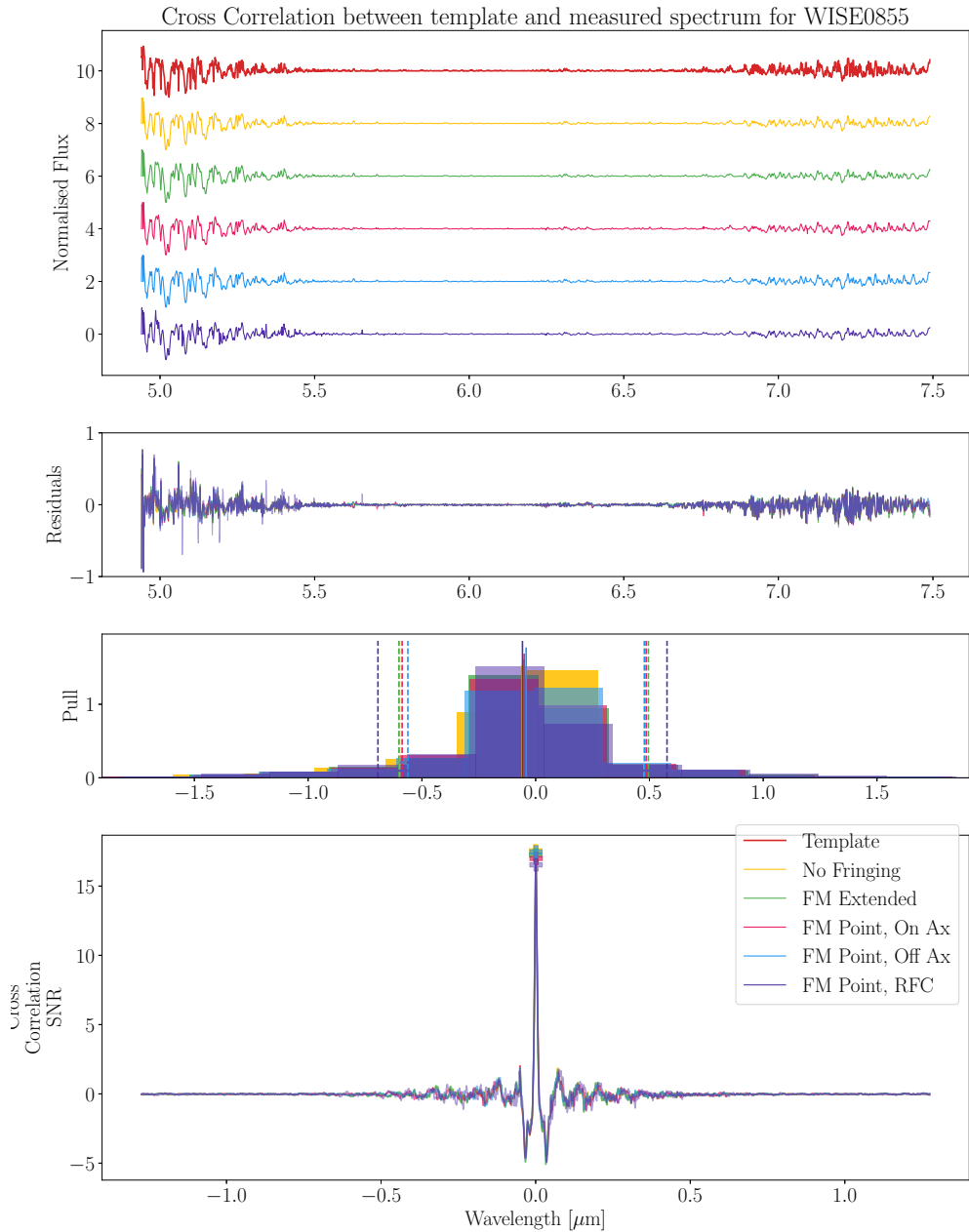


Figure 45: Cross correlation between the input template and the extracted spectra for WISE0855.

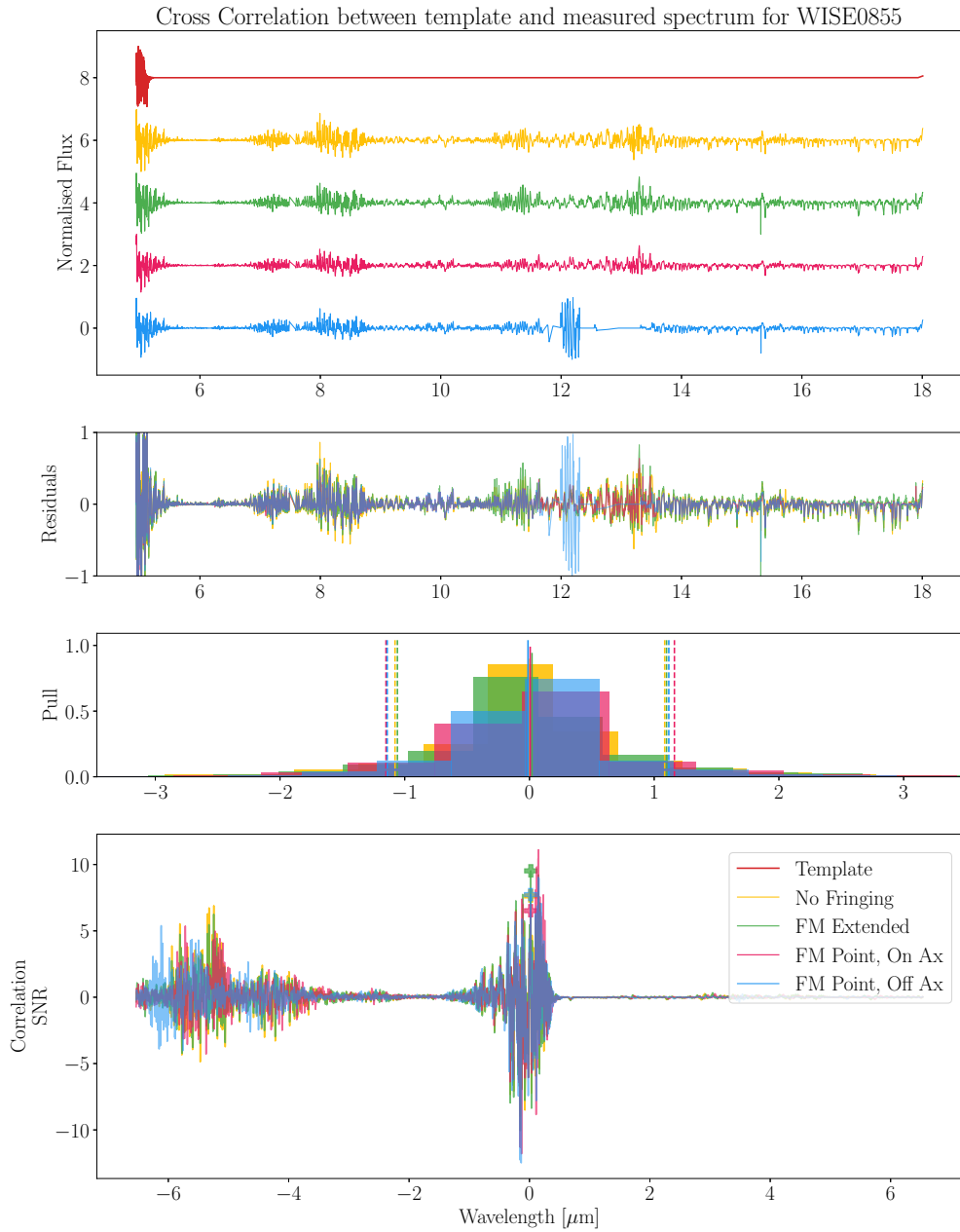


Figure 46: Single species cross correlation between CO and WISE0855. The lack of significant spectral coverage results in a false positive detection.

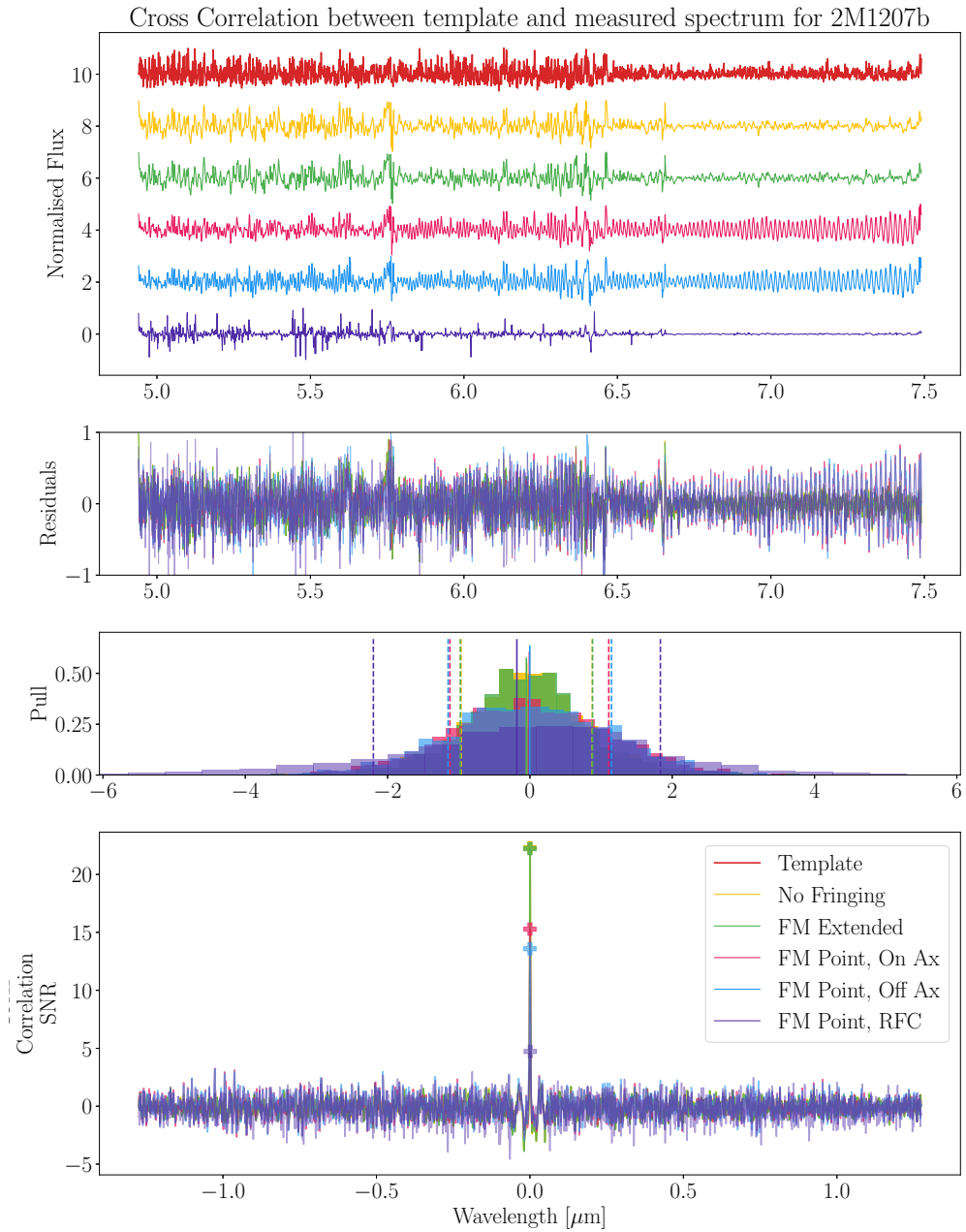


Figure 47: Cross correlation between the input template and the extracted spectra for 2M1207b.

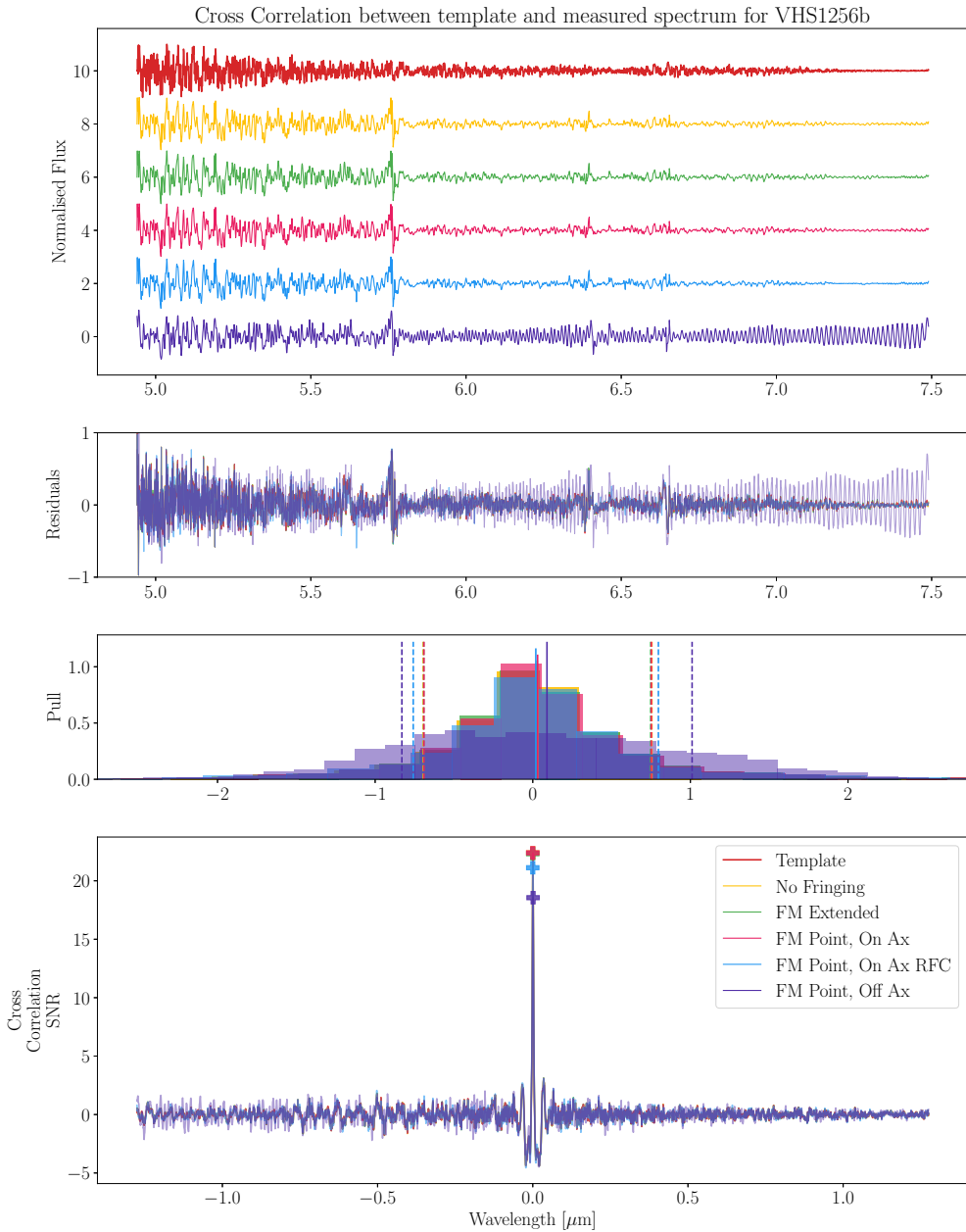


Figure 48: Cross correlation between the input template and the extracted spectra for VHS1256b. In this plot, the on axis point source has not been corrected with the extended source fringe flat, resulting in a higher SNR than with the correction.

A.3 FULL POSTERIOR DISTRIBUTIONS

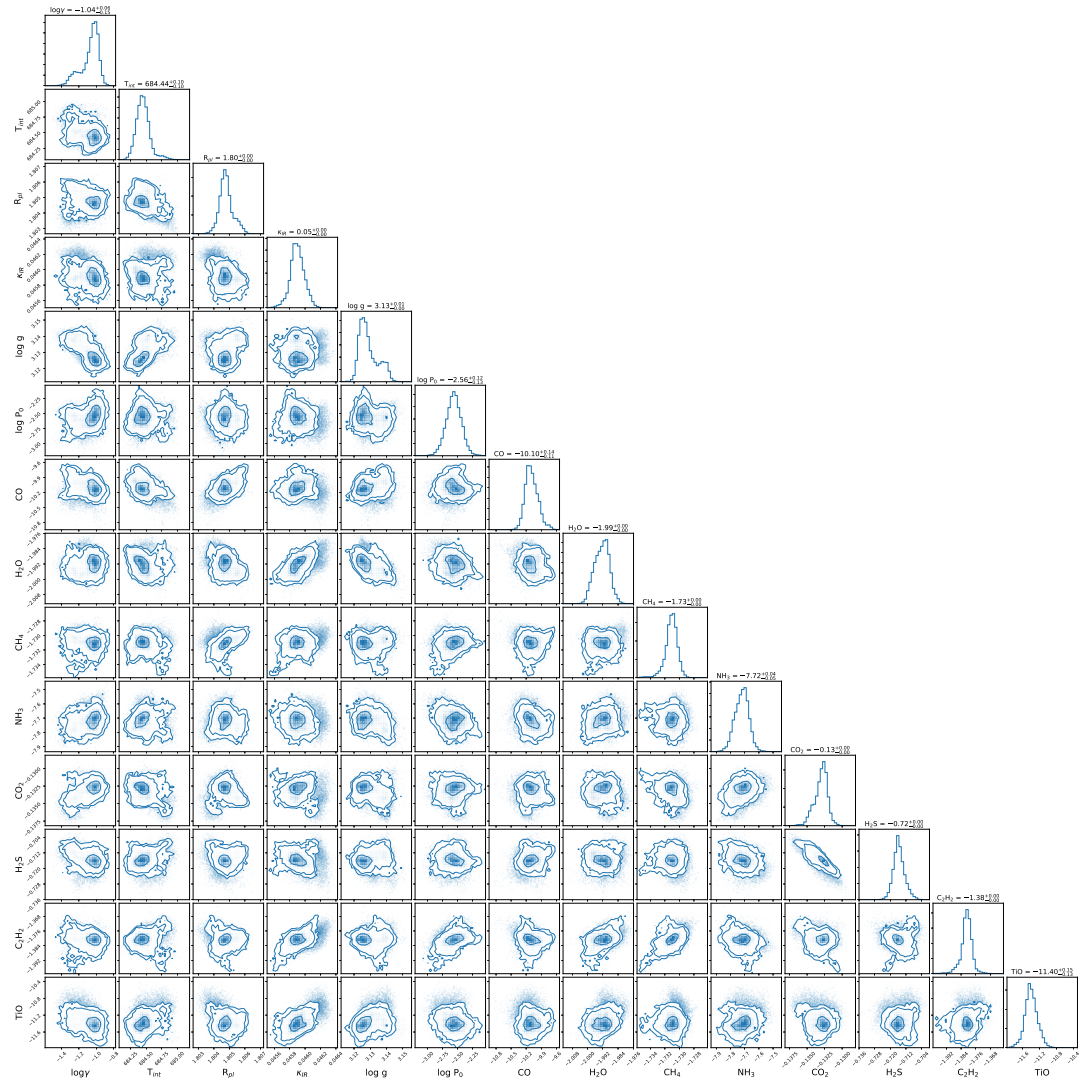


Figure 49: VHS-1256b, no fringing, Channel 1.

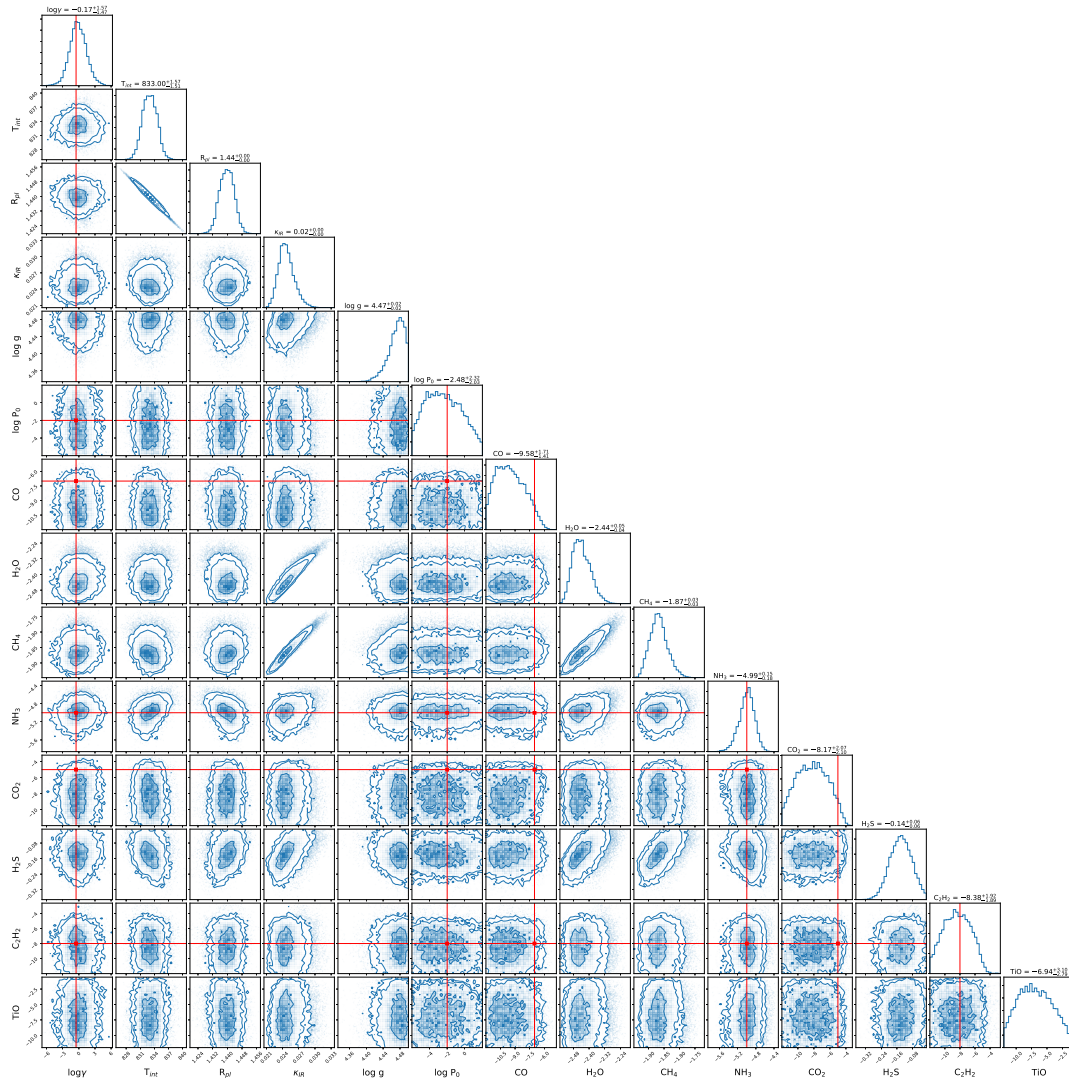


Figure 50: VHS-1256b, point source fringing, Channel 1.

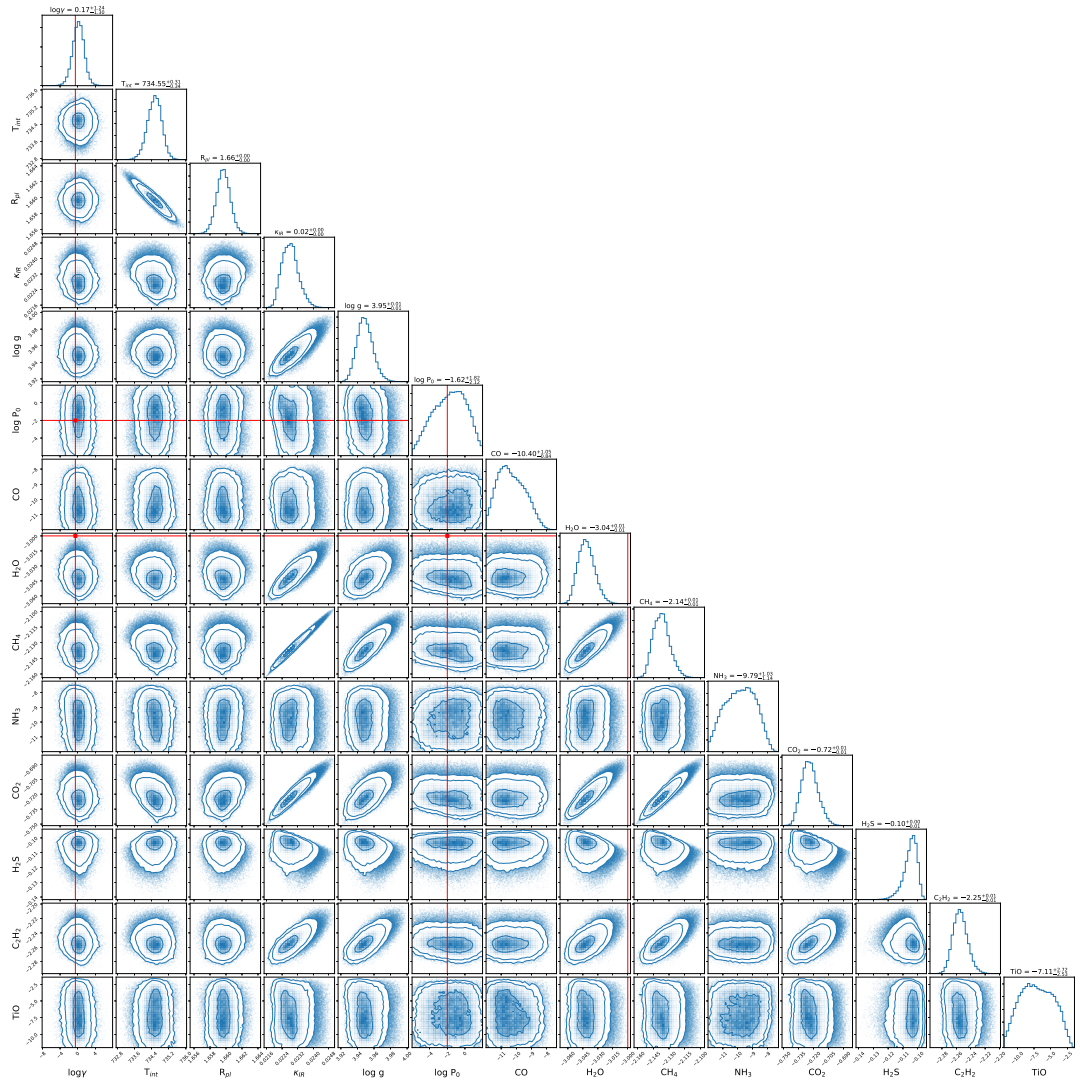


Figure 51: VHS-1256b, no fringing, Channels 1 through 3.

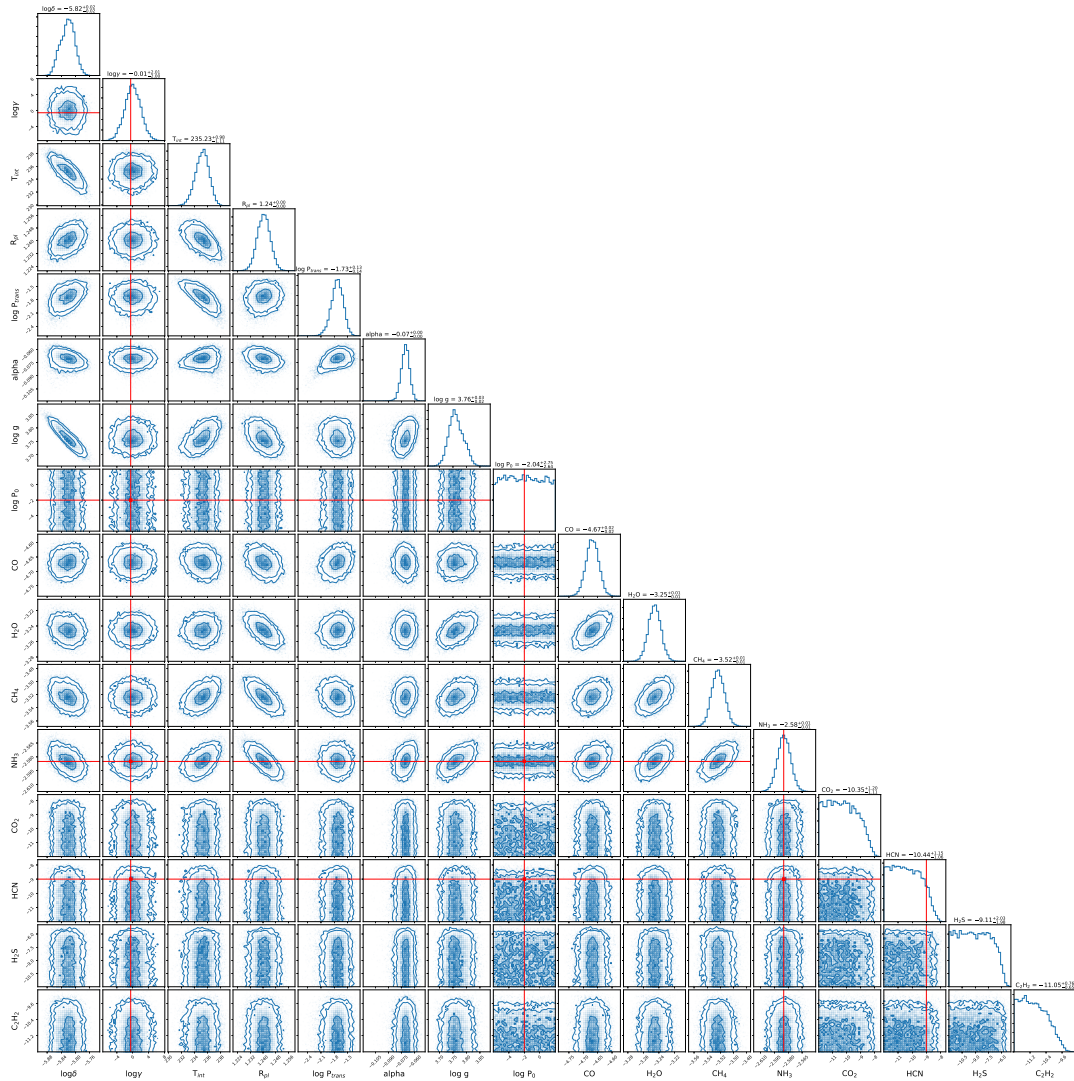


Figure 52: WISE 0855, no fringing, Channel 1.

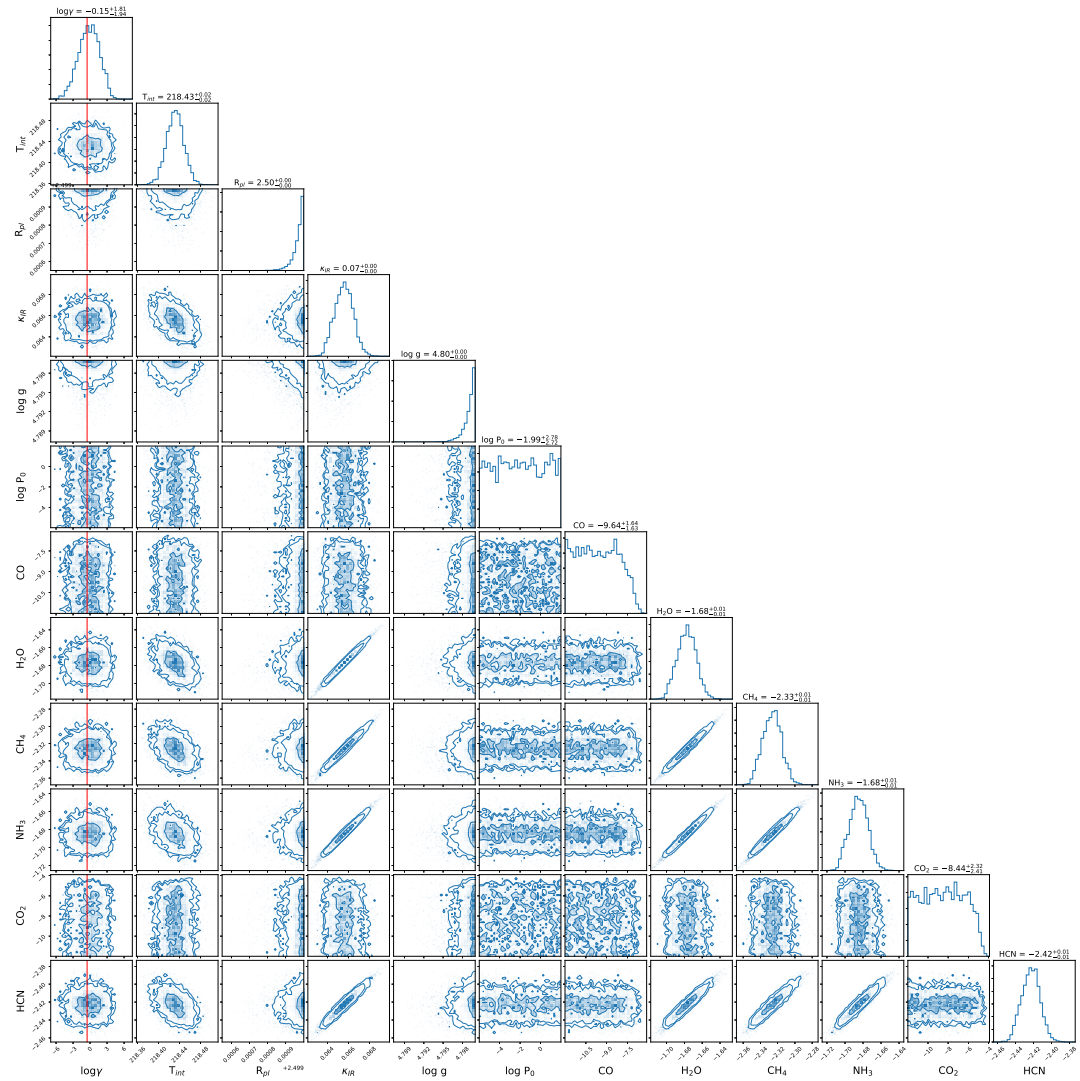


Figure 53: WISE 0855 with point source fringing in Channel 1.

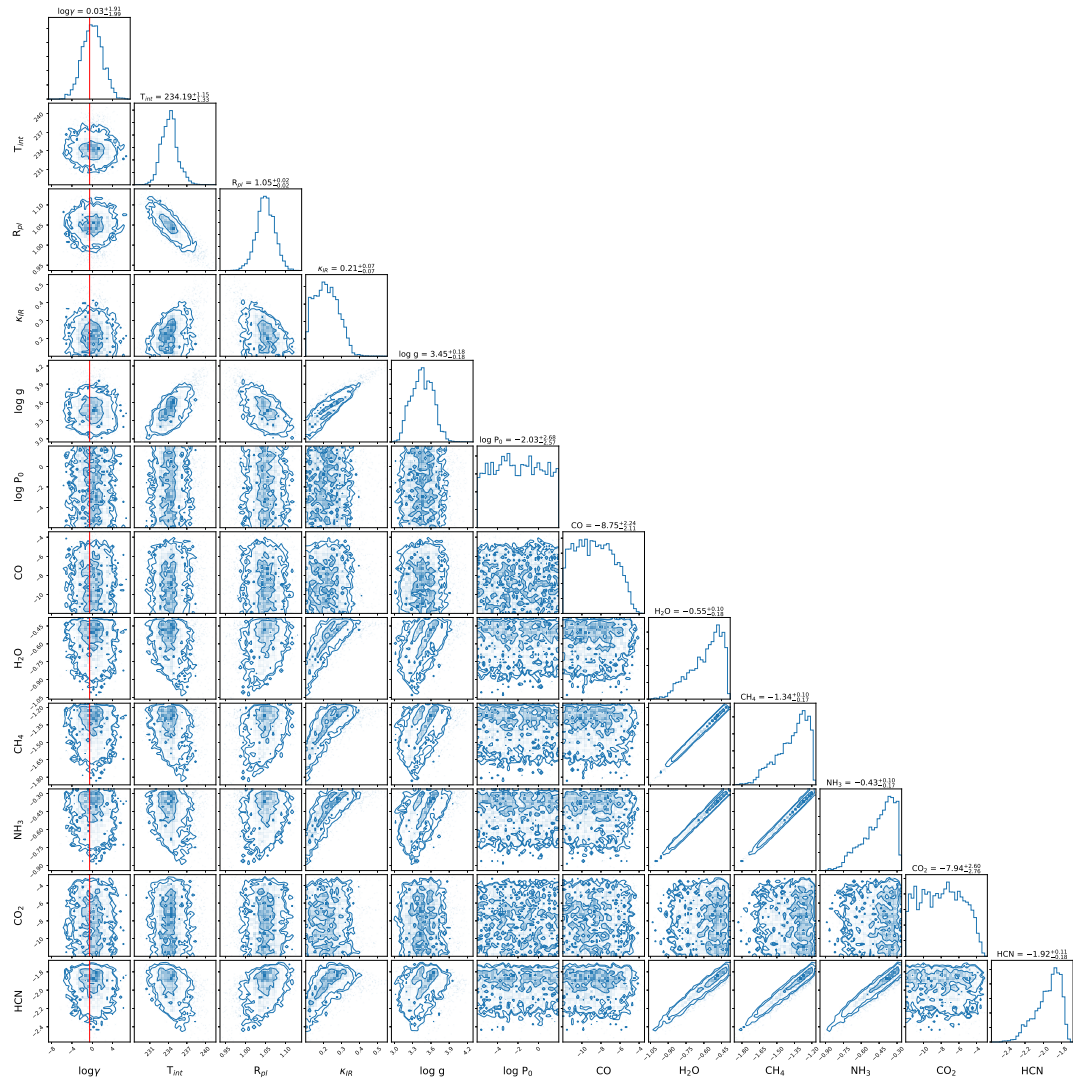


Figure 54: WISE 0855, no fringing, Channels 1 through 3.

A.4 PACKAGE REQUIREMENTS

```
mirisim==2.2rc1
jwst==0.15.1.dev2+g62bab376
astropy==3.2.1
future==0.18.2
json5==0.8.4
jsonschema==3.0.1
matplotlib==3.1.0
mpi4py==3.0.3
mpmath==1.1.0
numpy==1.16.4
pymultinest==2.7
petitradtrans==*
scipy==1.3.0
seaborn==0.9.0
spectres==2.0.0
```

WORKS CITED

- Ackerman, A. S. and M. S. Marley. "Precipitating condensation clouds in substellar atmospheres". *Astrophysical Journal* 596. ISSN: 15384357. DOI: [10.1088/0004-637X/765/1/75](https://doi.org/10.1088/0004-637X/765/1/75) (2001): 872–885. Print.
- Aoyama, Y. and M. Ikoma. "Constraining Planetary Gas Accretion Rate from H α Linewidth and Intensity: Case of PDS 70 b and c". *arXiv eprint*. arXiv: [arXiv : 1909 . 08175v2](https://arxiv.org/abs/1909.08175v2) (2019). arXiv: [arXiv : 1909 . 08175v2](https://arxiv.org/abs/1909.08175v2). arXiv: [arXiv : 1909 . 08175v2](https://arxiv.org/abs/1909.08175v2).
- Argyriou, I., R. Azzollini, and B. Vandenbussche. "Spectrum extraction from detector plane images for the medium-resolution spectrometer of the mid-Infrared Instrument on-board the James Webb Space Telescope." *SPIE*. 2018. 124. Print.
- Argyriou, I., B. Vandenbussche, and M. Wells. "Fringing solution for the mid-infrared instrument on-board the James Webb Space Telescope". *SPIE*. 2018. 127. Print.
- Argyriou, I., et al. "Nature of point source fringes in mid-infrared spectra acquired with the James Webb Space Telescope". *Astronomy & Astrophysics* (2020): 1–13. Print.
- Bailey, V., et al. "HD 106906 b: A planetary-mass companion outside a massive debris disk". *Astrophysical Journal Letters* 780.1. ISSN: 20418205. DOI: [10 . 1088 / 2041 - 8205 / 780 / 1 / L4](https://doi.org/10.1088/2041-8205/780/1/L4). arXiv: [1312 . 1265](https://arxiv.org/abs/1312.1265) (2014): 2–7. arXiv: [1312 . 1265](https://arxiv.org/abs/1312.1265). arXiv: [1312 . 1265](https://arxiv.org/abs/1312.1265).
- Barman, T. S., Q. M. Konopacky, B. Macintosh, and C. Marois. "Simultaneous detection of water, methane, and carbon monoxide in the atmosphere of Exoplanet hr 8799 b". *Astrophysical Journal* 804.1. ISSN: 15384357. DOI: [10 . 1088 / 0004 - 637X / 804 / 1 / 61](https://doi.org/10.1088/0004-637X/804/1/61). arXiv: [1503 . 03539](https://arxiv.org/abs/1503.03539) (2015): 1–10. arXiv: [1503 . 03539](https://arxiv.org/abs/1503.03539). arXiv: [1503 . 03539](https://arxiv.org/abs/1503.03539). Web. <[http://dx.doi.org/10 . 1088 / 0004 - 637X / 804 / 1 / 61](http://dx.doi.org/10.1088/0004-637X/804/1/61)>.
- Barstow, J. K., et al. "A comparison of exoplanet spectroscopic retrieval tools". DOI: [10 . 1093 / mnras / staa548](https://doi.org/10.1093/mnras/staa548). arXiv: [2002 . 01063](https://arxiv.org/abs/2002.01063) (2020). arXiv: [2002 . 01063](https://arxiv.org/abs/2002.01063). arXiv: [2002 . 01063](https://arxiv.org/abs/2002.01063). Web. <[http://arxiv.org/abs/2002 . 01063](http://arxiv.org/abs/2002.01063)>.
- Batalha, N. E., et al. "Strategies for Constraining the Atmospheres of Temperate Terrestrial Planets with JWST". *The Astrophysical Journal* 856.2. ISSN: 2041-8213. DOI: [10 . 3847 / 2041 - 8213 / aab896](https://doi.org/10.3847/2041-8213/aab896). arXiv: [1803 . 07983](https://arxiv.org/abs/1803.07983) (2018): L34. arXiv: [1803 . 07983](https://arxiv.org/abs/1803.07983). arXiv: [1803 . 07983](https://arxiv.org/abs/1803.07983). Web. <[http://dx.doi.org/10 . 3847 / 2041 - 8213 / aab896](http://dx.doi.org/10.3847/2041-8213/aab896)>.
- Baudino, J.-l., et al. "Toward the Analysis of JWST Exoplanet Spectra : Identifying Troublesome Model Parameters". *The Astrophysical Journal* 850.2. ISSN: 1538-4357. DOI: [10 . 3847 / 1538 - 4357 / aa95be](https://doi.org/10.3847/1538-4357/aa95be) (2017): 150. Web. <[http://dx.doi.org/10 . 3847 / 1538 - 4357 / aa95be](http://dx.doi.org/10.3847/1538-4357/aa95be)>.
- Beamín, J. C., et al. "Temperature constraints on the coldest brown dwarf known: WISE 0855-0714". *Astronomy and Astrophysics* 570. ISSN: 14320746. DOI: [10 . 1051 / 0004 - 6361 / 201424505](https://doi.org/10.1051/0004-6361/201424505) (2014): 1–4. Print.

- Bean, J. L., et al. "The transiting exoplanet community early release science program for JWST". *Publications of the Astronomical Society of the Pacific* 130.993. DOI: [10.1088/1538-3873/aadbf3](https://doi.org/10.1088/1538-3873/aadbf3). arXiv: [1803.04985](https://arxiv.org/abs/1803.04985) (2018): 1–20. arXiv: [1803.04985](https://arxiv.org/abs/1803.04985). arXiv: [1803.04985](https://arxiv.org/abs/1803.04985).
- Behmard, A., E. A. Petigura, and A. W. Howard. "Data-driven Spectroscopy of Cool Stars at High Spectral Resolution". *The Astrophysical Journal* 876.1. DOI: [10.3847/1538-4357/ab14e0](https://doi.org/10.3847/1538-4357/ab14e0). arXiv: [arXiv:1904.00094v1](https://arxiv.org/abs/1904.00094v1) (2019): 68. arXiv: [arXiv:1904.00094v1](https://arxiv.org/abs/1904.00094v1). arXiv: [arXiv:1904.00094v1](https://arxiv.org/abs/1904.00094v1).
- Beichman, C., et al. "Wise y dwarfs as probes of the brown dwarf-exoplanet connection". *Astrophysical Journal* 783.2. ISSN: 15384357. DOI: [10.1088/0004-637X/783/2/68](https://doi.org/10.1088/0004-637X/783/2/68). arXiv: [1401.1194](https://arxiv.org/abs/1401.1194) (2014). arXiv: [1401.1194](https://arxiv.org/abs/1401.1194). arXiv: [1401.1194](https://arxiv.org/abs/1401.1194).
- Beichman, C. A., P.-o. Lagage, and M. Ygouf. "1188 - Spectroscopy of Young , Widely Separated Exoplanets". 4. Print.
- Beichman, C. A., et al. "1194 - Characterization of the HR 8799 planetary system and planet search". Print.
- Beichman, C. A. and T. P. Greene. "Observing Exoplanets with the James Webb Space Telescope". *Handbook of Exoplanets* 2009. DOI: [10.1007/978-3-319-55333-7_85](https://doi.org/10.1007/978-3-319-55333-7_85) (2018): 1283–1308. Print.
- Beichman, C. A., et al. "Astro2020 Science White Paper: Direct Imaging and Spectroscopy of Exoplanets with the James Webb Space Telescope". *Astro2020 Science White Paper*. Web. <<https://jwst.stsci.edu/observing-programs/approved-gto-programs.>>.
- Benneke, B. and S. Seager. "Atmospheric retrieval for super-earths: Uniquely constraining the atmospheric composition with transmission spectroscopy". *Astrophysical Journal* 753.2. ISSN: 15384357. DOI: [10.1088/0004-637X/753/2/100](https://doi.org/10.1088/0004-637X/753/2/100). arXiv: [1203.4018](https://arxiv.org/abs/1203.4018) (2012). arXiv: [1203.4018](https://arxiv.org/abs/1203.4018). arXiv: [1203.4018](https://arxiv.org/abs/1203.4018).
- Benneke, B. "Bayesian Atmospheric Retrieval for Exoplanets". PhD Thesis. Massachusetts Institute of Technology, 2013. Print.
- Benneke, B., et al. "Water Vapor and Clouds on the Habitable-zone Sub-Neptune Exoplanet K2-18b". *The Astrophysical Journal* 887.1. ISSN: 2041-8213. DOI: [10.3847/2041-8213/ab59dc](https://doi.org/10.3847/2041-8213/ab59dc). arXiv: [1909.04642](https://arxiv.org/abs/1909.04642) (2019): L14. arXiv: [1909.04642](https://arxiv.org/abs/1909.04642). arXiv: [1909.04642](https://arxiv.org/abs/1909.04642).
- Biller, B. "The time domain for brown dwarfs and directly imaged giant exoplanets: the power of variability monitoring". *Astronomical Review* 13.1. ISSN: 2167-2857. DOI: [10.1080/21672857.2017.1303105](https://doi.org/10.1080/21672857.2017.1303105) (2017): 1–27. Web. <<http://dx.doi.org/10.1080/21672857.2017.1303105>>.
- Biller, B. A. and M. Bonnefoy. "Exoplanet Atmosphere Measurements from Direct Imaging". *Handbook of Exoplanets*. DOI: [10.1007/978-3-319-55333-7_101](https://doi.org/10.1007/978-3-319-55333-7_101). arXiv: [arXiv:1807.05136v1](https://arxiv.org/abs/1807.05136v1) (2018): 2107–2135. arXiv: [arXiv:1807.05136v1](https://arxiv.org/abs/1807.05136v1). arXiv: [arXiv:1807.05136v1](https://arxiv.org/abs/1807.05136v1).
- Birkmann, S., P.-o. Lagage, and P. Ferruit. "1270 - Characterizing the TWA 27 system". Print.
- Blanco-Cuaresma, S. "Modern stellar spectroscopy caveats". *Monthly Notices of the Royal Astronomical Society* 486.2. arXiv: [arXiv:1902.09558v2](https://arxiv.org/abs/1902.09558v2) (2019): 2075–2101. arXiv: [arXiv:1902.09558v2](https://arxiv.org/abs/1902.09558v2). arXiv: [arXiv:1902.09558v2](https://arxiv.org/abs/1902.09558v2).
- Boccaletti, A., et al. "The Mid-Infrared Instrument for the James Webb Space Telescope , V: Predicted Performance of the MIRI Coronagraphs". *Publications of the Astronomical Society of the Pacific* 127.953. ISSN: 00046280. DOI:

- [10.1086/682256](https://arxiv.org/abs/1008.02352). arXiv: 1508.02352 (2015): 633–645. arXiv: 1508.02352. arXiv: 1508.02352.
- Bodis, L. “Quantification of spectral similarity towards automatic spectra verification”. Diss. ETH Zurich, 2007. Web. <<https://doi.org/10.3929/ethz-a-005479205>>.
- Bouchet, P., et al. “The Mid-Infrared Instrument for the James Webb Space Telescope, III: MIRIM, The MIRI Imager”. *Publications of the Astronomical Society of the Pacific* 127.953. ISSN: 00046280, 15383873 (2015): 612–622. Web. <<http://www.jstor.org/stable/10.1086/682254>>.
- Bowler, B. P. “Imaging Extrasolar Giant Planets”. *Publications of the Astronomical Society of the Pacific* 128.968. ISSN: 1538-3873. DOI: 10.1088/1538-3873/128/968/102001 (2016): 1–38. Web. <<http://dx.doi.org/10.1088/1538-3873/128/968/102001>>.
- Buchner, J., et al. “X-ray spectral modelling of the AGN obscuring region in the CDFS: Bayesian model selection and catalogue”. *Astronomy and Astrophysics* 564. ISSN: 14320746. DOI: 10.1051/0004-6361/201322971. arXiv: 1402.0004 (2014): 1–25. arXiv: 1402.0004. arXiv: 1402.0004.
- Buenzli, E., et al. “Cloud Structure of the Nearest Brown Dwarfs II: High Amplitude Variability for Luhman 16 A and B In and Out of the 0.99 μm FeH Feature”. *Astrophysical Journal* 812.2. ISSN: 15384357. DOI: 10.1088/0004-637X/812/2/163. arXiv: 1509.06148 (2015). arXiv: 1509.06148. arXiv: 1509.06148.
- Buenzli, E., et al. “Cloud structure of the nearest brown dwarfs: Spectroscopic variability of Luhman 16AB from the Hubble space telescope”. *Astrophysical Journal* 798.2. ISSN: 15384357. DOI: 10.1088/0004-637X/798/2/127. arXiv: 1411.0003 (2015). arXiv: 1411.0003. arXiv: 1411.0003.
- Burningham, B., et al. “Retrieval of atmospheric properties of cloudy L dwarfs”. *Monthly Notices of the Royal Astronomical Society* 470.1. ISSN: 13652966. DOI: 10.1093/MNRAS/STX1246. arXiv: 1701.01257 (2017): 1177–1197. arXiv: 1701.01257. arXiv: 1701.01257.
- Burrows, A., W. B. Hubbard, J. I. Lunine, and J. Liebert. “The theory of brown dwarfs and extrasolar giant planets”. *Reviews of Modern Physics* 73.3. ISSN: 00346861. DOI: 10.1103/RevModPhys.73.719. arXiv: 0103383 [astro-ph] (2001): 719–765. arXiv: 0103383 [astro-ph]. arXiv: 0103383 [astro-ph].
- Burrows, A., D. Sudarsky, and J. I. Lunine. “Beyond the T Dwarfs: Theoretical Spectra, Colors, and Detectability of the Coolest Brown Dwarfs”. *The Astrophysical Journal* 596. DOI: 10.1086/377709. arXiv: arXiv:1306.2144v2 (2003): 587–596. arXiv: arXiv:1306.2144v2. arXiv: arXiv:1306.2144v2. Web. <<http://dx.doi.org/10.3847/0004-6256/152/6/217>>.
- Bushouse, H., M. Droettboom, and P. Greenfield. “The James Webb Space Telescope Data Calibration Pipeline”. *14th Python in Science Conf.* 2015. 289. arXiv: 0606175 [astro-ph].
- Carnall, A. C. “SpectRes: A Fast Spectral Resampling Tool in Python”. Edinburgh. arXiv: 1705.05165. Web. <<http://arxiv.org/abs/1705.05165>>.
- Chauvin, G., et al. “A giant planet candidate near a young brown dwarf Direct VLT/NACO observations using IR wavefront sensing”. *Astronomy and Astrophysics* 425.2. ISSN: 00046361. DOI: 10.1051/0004-6361:200400056 (2004): 29–32. Print.

- Chauvin, G., et al. "Orbital characterization of the β Pictoris b giant planet". *Astronomy and Astrophysics* 542. ISSN: 00046361. DOI: [10.1051/0004-6361/201118346](https://doi.org/10.1051/0004-6361/201118346). arXiv: [1202.2655](https://arxiv.org/abs/1202.2655) (2012): 1–9. arXiv: [1202.2655](https://arxiv.org/abs/1202.2655). arXiv: [1202.2655](https://arxiv.org/abs/1202.2655).
- Chen, H., E. T. Wolf, Z. Zhan, and D. E. Horton. "Habitability and Spectroscopic Observability of Warm M-dwarf Exoplanets Evaluated with a 3D Chemistry-Climate Model". *The Astrophysical Journal* 886.1. DOI: [10.3847/1538-4357/ab4f7e](https://doi.org/10.3847/1538-4357/ab4f7e). arXiv: [1907.10048](https://arxiv.org/abs/1907.10048) (2019): 23. arXiv: [1907.10048](https://arxiv.org/abs/1907.10048). arXiv: [1907.10048](https://arxiv.org/abs/1907.10048). Web. <<http://arxiv.org/abs/1907.10048>>.
- Chilcote, J., et al. "1–2.4 μ m Near-IR Spectrum of the Giant Planet β Pictoris b Obtained with the Gemini Planet Imager". *The Astronomical Journal* 153.4. ISSN: 0004-6256. DOI: [10.3847/1538-3881/aa63e9](https://doi.org/10.3847/1538-3881/aa63e9). arXiv: [1703.00011](https://arxiv.org/abs/1703.00011) (2017): 182. arXiv: [1703.00011](https://arxiv.org/abs/1703.00011). arXiv: [1703.00011](https://arxiv.org/abs/1703.00011). Web. <<http://dx.doi.org/10.3847/1538-3881/aa63e9>>.
- Chilcote, J., et al. "The first H-band spectrum of the giant planet β Pictoris b". *Astrophysical Journal Letters* 798.1. ISSN: 20418213. DOI: [10.1088/2041-8205/798/1/L3](https://doi.org/10.1088/2041-8205/798/1/L3) (2015): 1–5. Print.
- Christiaens, V., et al. "Evidence for a Circumplanetary Disk around Protoplanet PDS 70 b". *The Astrophysical Journal* 877.2. ISSN: 2041-8213. DOI: [10.3847/2041-8213/ab212b](https://doi.org/10.3847/2041-8213/ab212b). arXiv: [1905.06370](https://arxiv.org/abs/1905.06370) (2019): L33. arXiv: [1905.06370](https://arxiv.org/abs/1905.06370). arXiv: [1905.06370](https://arxiv.org/abs/1905.06370). Web. <<http://dx.doi.org/10.3847/2041-8213/ab212b>>.
- Consortium, M. "MIRISim Documentation" (2018). Print.
- Cooper, C. S., D. Sudarsky, J. A. Milsom, and J. I. Lunine. "Modeling the Formation of Clouds in Brown Dwarf Atmospheres". *The Astrophysical Journal* 156.2. DOI: [10.1086/367763](https://doi.org/10.1086/367763). arXiv: [0205192v3](https://arxiv.org/abs/0205192v3) [arXiv:astro-ph] (2003): 1320–1337. arXiv: [0205192v3](https://arxiv.org/abs/0205192v3) [arXiv:astro-ph]. arXiv: [0205192v3](https://arxiv.org/abs/0205192v3) [arXiv:astro-ph].
- Cossou, C. "MIRISim Spreadsheet and Quick examples". Print.
- Crossfield, I. J., et al. "A global cloud map of the nearest known brown dwarf". *Nature* 505.7485. ISSN: 00280836. DOI: [10.1038/nature12955](https://doi.org/10.1038/nature12955) (2014): 654–656. Web. <<http://dx.doi.org/10.1038/nature12955>>.
- Currie, T., et al. "Direct imaging confirmation and characterization of a dust-enshrouded candidate exoplanet orbiting fomalhaut". *Astrophysical Journal Letters* 760.2. ISSN: 20418205. DOI: [10.1088/2041-8205/760/2/L32](https://doi.org/10.1088/2041-8205/760/2/L32) (2012): 6–11. Print.
- Cushing, M. C., et al. "The discovery of y dwarfs using data from the wide-field infrared survey explorer (WISE)". *Astrophysical Journal* 743.1. ISSN: 15384357. DOI: [10.1088/0004-637X/743/1/50](https://doi.org/10.1088/0004-637X/743/1/50). arXiv: [1108.4678](https://arxiv.org/abs/1108.4678) (2011). arXiv: [1108.4678](https://arxiv.org/abs/1108.4678). arXiv: [1108.4678](https://arxiv.org/abs/1108.4678).
- Danielski, C., et al. "Atmospheric Characterization of Directly Imaged Exoplanets with JWST /MIRI". *The Astronomical Journal* 156.6. ISSN: 1538-3881. DOI: [10.3847/1538-3881/aae651](https://doi.org/10.3847/1538-3881/aae651). arXiv: [1810.00894](https://arxiv.org/abs/1810.00894) (2018): 276. arXiv: [1810.00894](https://arxiv.org/abs/1810.00894). arXiv: [1810.00894](https://arxiv.org/abs/1810.00894).
- De Rosa, R. J., et al. "Spectroscopic characterization of HD 95086 b with the Gemini Planet Imager". *The Astrophysical Journal* 824.2. ISSN: 1538-4357. DOI: [10.3847/0004-637X/824/2/121](https://doi.org/10.3847/0004-637X/824/2/121). arXiv: [1604.01411](https://arxiv.org/abs/1604.01411) (2016): 121. arXiv: [1604.01411](https://arxiv.org/abs/1604.01411). arXiv: [1604.01411](https://arxiv.org/abs/1604.01411). Web. <<http://dx.doi.org/10.3847/0004-637X/824/2/121>>.

- Des Marais, D. J., et al. "Remote sensing of planetary properties and biosignatures on extrasolar terrestrial planets". *Astrobiology* 2.2. ISSN: 15311074. doi: [10.1089/15311070260192246](https://doi.org/10.1089/15311070260192246) (2002): 153–181. Print.
- Faherty, J. K., et al. "Signatures of cloud, temperature, and gravity from spectra of the closest brown dwarfs". *Astrophysical Journal* 790.2. ISSN: 15384357. doi: [10.1088/0004-637X/790/2/90](https://doi.org/10.1088/0004-637X/790/2/90) (2014). Print.
- Faherty, J. K., C. G. Tinney, A. Skemer, and A. J. Monson. "Indications of water clouds in the coldest known brown dwarf". *The Astrophysical Journal Letters* 793.1. arXiv: [arXiv:1408.4671v2](https://arxiv.org/abs/1408.4671v2) (2018). arXiv: [arXiv:1408.4671v2](https://arxiv.org/abs/1408.4671v2). arXiv: [arXiv:1408.4671v2](https://arxiv.org/abs/1408.4671v2).
- Fegley, B. and K. Lodders. "Chemical Models of the Deep Atmospheres of Jupiter and Saturn". *Icarus* 110 (1994): 117–154. Print.
- Feng, Y. K., et al. "Characterizing Earth Analogs in Reflected Light: Atmospheric Retrieval Studies for Future Space Telescopes". *The Astronomical Journal* 155.5. ISSN: 1538-3881. doi: [10.3847/1538-3881/aab95c](https://doi.org/10.3847/1538-3881/aab95c) (2018): 200. Web. <<http://dx.doi.org/10.3847/1538-3881/aab95c>>.
- Ferguson, H., P. Greenfield, and A. Conti. "JWST Astronomy Data Analysis Tools Roadmap Documentation vo.1". Print.
- Feroz, F. and M. P. Hobson. "Multimodal nested sampling: An efficient and robust alternative to Markov Chain Monte Carlo methods for astronomical data analyses". *Monthly Notices of the Royal Astronomical Society* 384.2. ISSN: 00358711. doi: [10.1111/j.1365-2966.2007.12353.x](https://doi.org/10.1111/j.1365-2966.2007.12353.x). arXiv: [0704.3704](https://arxiv.org/abs/0704.3704) (2008): 449–463. arXiv: [0704.3704](https://arxiv.org/abs/0704.3704). arXiv: [0704.3704](https://arxiv.org/abs/0704.3704).
- Feroz, F., M. P. Hobson, and M. Bridges. "MultiNest: An efficient and robust Bayesian inference tool for cosmology and particle physics". *Monthly Notices of the Royal Astronomical Society* 398.4. ISSN: 00358711. doi: [10.1111/j.1365-2966.2009.14548.x](https://doi.org/10.1111/j.1365-2966.2009.14548.x). arXiv: [0809.3437](https://arxiv.org/abs/0809.3437) (2009): 1601–1614. arXiv: [0809.3437](https://arxiv.org/abs/0809.3437). arXiv: [0809.3437](https://arxiv.org/abs/0809.3437).
- Feroz, F., M. P. Hobson, E. Cameron, and A. N. Pettitt. "Importance Nested Sampling and the MultiNest Algorithm". *The Open Journal of Astrophysics* 2.1. doi: [10.21105/astro.1306.2144](https://doi.org/10.21105/astro.1306.2144). arXiv: [1306.2144](https://arxiv.org/abs/1306.2144) (2019): 1–17. arXiv: [1306.2144](https://arxiv.org/abs/1306.2144). arXiv: [1306.2144](https://arxiv.org/abs/1306.2144).
- Fisher, C., et al. "Interpreting High-Resolution Spectroscopy of Exoplanets Using Cross-Correlations and Supervised Machine Learning". arXiv: [1910.11627](https://arxiv.org/abs/1910.11627) (2019): 1–15. arXiv: [1910.11627](https://arxiv.org/abs/1910.11627). arXiv: [1910.11627](https://arxiv.org/abs/1910.11627). Web. <<http://arxiv.org/abs/1910.11627>>.
- Foreman-Mackey, D. "corner.py: Scatterplot matrices in Python". *The Journal of Open Source Software* 1.2. ISSN: 2475-9066. doi: [10.21105/joss.00024](https://doi.org/10.21105/joss.00024) (2016): 24. Print.
- Foreman-Mackey, D., D. W. Hogg, D. Lang, and J. Goodman. "emcee : The MCMC Hammer ". *Publications of the Astronomical Society of the Pacific* 125.925. ISSN: 00046280. doi: [10.1086/670067](https://doi.org/10.1086/670067). arXiv: [1202.3665](https://arxiv.org/abs/1202.3665) (2013): 306–312. arXiv: [1202.3665](https://arxiv.org/abs/1202.3665). arXiv: [1202.3665](https://arxiv.org/abs/1202.3665).
- Fu, Q. and K. N. Liou. "On the correlated k-distribution method for radiative transfer in nonhomogeneous atmospheres". *Journal of the Atmospheric Sciences* 49.22. ISSN: 00224928. doi: [10.1175/1520-0469\(1992\)049<2139:otcdmf>2.0.co;2](https://doi.org/10.1175/1520-0469(1992)049<2139:otcdmf>2.0.co;2) (1992): 2139–2156. Print.
- Galicher, R., et al. "M-band imaging of the hr 8799 planetary system using an innovative loci-based background subtraction technique". *The Astrophys-*

- cal Journal Letters* 41. doi: [10.1088/2041-8205/739/2/L41](https://doi.org/10.1088/2041-8205/739/2/L41) (2011): 3–7. Print.
- Gandhi, S. and N. Madhusudhan. “Retrieval of exoplanet emission spectra with HyDRA”. *Monthly Notices of the Royal Astronomical Society* 474.1. ISSN: 13652966. doi: [10.1093/mnras/stx2748](https://doi.org/10.1093/mnras/stx2748). arXiv: [1710.06433](https://arxiv.org/abs/1710.06433) (2018): 271–278. arXiv: [1710.06433](https://arxiv.org/abs/1710.06433). arXiv: [1710.06433](https://arxiv.org/abs/1710.06433).
- Garcia, E. V., et al. “Individual, Model-independent Masses of the Closest Known Brown Dwarf Binary to the Sun”. *The Astrophysical Journal* 846.2. ISSN: 1538-4357. doi: [10.3847/1538-4357/aa844f](https://doi.org/10.3847/1538-4357/aa844f). arXiv: [1708.02714](https://arxiv.org/abs/1708.02714) (2017): 97. arXiv: [1708.02714](https://arxiv.org/abs/1708.02714). arXiv: [1708.02714](https://arxiv.org/abs/1708.02714).
- Garland, R. and P. G. J. Irwin. “Effectively Calculating Gaseous Absorption in Radiative Transfer Models of Exoplanetary and Brown Dwarf Atmospheres”. *arXiv eprint* March. arXiv: [1903.03997](https://arxiv.org/abs/1903.03997) (2019). arXiv: [1903.03997](https://arxiv.org/abs/1903.03997). arXiv: [1903.03997](https://arxiv.org/abs/1903.03997). Web. <<http://arxiv.org/abs/1903.03997>>.
- Gauza, B., et al. “Discovery of a young planetary mass companion to the nearby M dwarf VHS J125601.92-125723.9”. *Astrophysical Journal* 804.2. ISSN: 15384357. doi: [10.1088/0004-637X/804/2/96](https://doi.org/10.1088/0004-637X/804/2/96). arXiv: [1505.00806](https://arxiv.org/abs/1505.00806) (2015): 1–18. arXiv: [1505.00806](https://arxiv.org/abs/1505.00806). arXiv: [1505.00806](https://arxiv.org/abs/1505.00806). Web. <<http://dx.doi.org/10.1088/0004-637X/804/2/96>>.
- Glasse, A., et al. “The Mid-Infrared Instrument for the James Webb Space Telescope , IX: Predicted Sensitivity”. *Publications of the Astronomical Society of the Pacific* 127.953. ISSN: 00046280. doi: [10.1086/682259](https://doi.org/10.1086/682259). arXiv: [1508.02427](https://arxiv.org/abs/1508.02427) (2015): 686–695. arXiv: [1508.02427](https://arxiv.org/abs/1508.02427). arXiv: [1508.02427](https://arxiv.org/abs/1508.02427).
- Goody, R., R. West, L. Chen, and D. Crisp. “The correlated-k method for radiation calculations in nonhomogeneous atmospheres”. *Journal of Quantitative Spectroscopy and Radiative Transfer* 42.6. ISSN: 00224073. doi: [10.1016/0022-4073\(89\)90044-7](https://doi.org/10.1016/0022-4073(89)90044-7) (1989): 539–550. Print.
- Gordon, I. E., et al. “The HITRAN2016 molecular spectroscopic database”. *Journal of Quantitative Spectroscopy and Radiative Transfer* 203. ISSN: 00224073. doi: [10.1016/j.jqsrt.2017.06.038](https://doi.org/10.1016/j.jqsrt.2017.06.038) (2017): 3–69. Print.
- Goyal, J. M., et al. “Fully scalable forward model grid of exoplanet transmission spectra”. *Monthly Notices of the Royal Astronomical Society* 482.4. ISSN: 13652966. doi: [10.1093/mnras/sty3001](https://doi.org/10.1093/mnras/sty3001). arXiv: [1810.12971](https://arxiv.org/abs/1810.12971) (2019): 4503–4513. arXiv: [1810.12971](https://arxiv.org/abs/1810.12971). arXiv: [1810.12971](https://arxiv.org/abs/1810.12971).
- GRAVITY Collaboration, et al. “Peering into the formation history of beta Pictoris b with VLTI/GRAVITY long baseline interferometry”. *Astronomy & Astrophysics* 633. doi: [10.1051/0004-6361/201936898](https://doi.org/10.1051/0004-6361/201936898). arXiv: [1912.04651](https://arxiv.org/abs/1912.04651) (2020): 1–21. arXiv: [1912.04651](https://arxiv.org/abs/1912.04651). arXiv: [1912.04651](https://arxiv.org/abs/1912.04651). Web. <<http://arxiv.org/abs/1912.04651>>.
- Greenbaum, A. Z., et al. “GPI Spectra of HR 8799 c, d, and e from 1.5 to 2.4 μ m with KLIP Forward Modeling”. *The Astronomical Journal* 155.6. ISSN: 0004-6256. doi: [10.3847/1538-3881/aabcb8](https://doi.org/10.3847/1538-3881/aabcb8). arXiv: [1804.07774](https://arxiv.org/abs/1804.07774) (2018): 226. arXiv: [1804.07774](https://arxiv.org/abs/1804.07774). arXiv: [1804.07774](https://arxiv.org/abs/1804.07774).
- Guillot, T. “On the radiative equilibrium of irradiated planetary atmospheres”. *Astronomy and Astrophysics* 520.18. ISSN: 00046361. doi: [10.1051/0004-6361/200913396](https://doi.org/10.1051/0004-6361/200913396). arXiv: [1006.4702](https://arxiv.org/abs/1006.4702) (2010): 1–13. arXiv: [1006.4702](https://arxiv.org/abs/1006.4702). arXiv: [1006.4702](https://arxiv.org/abs/1006.4702).

- Haffert, S. Y., et al. "Two accreting protoplanets around the young star PDS 70". *Nature Astronomy* 3.8. ISSN: 23973366. DOI: [10.1038/s41550-019-0780-5](https://doi.org/10.1038/s41550-019-0780-5) (2019): 749–754. Web. <<http://dx.doi.org/10.1038/s41550-019-0780-5>>.
- Helling, C. and S. Casewell. "Atmospheres of Brown Dwarfs". *The Astronomy and Astrophysics Review* 22. arXiv: [arXiv:1410.6029v2](https://arxiv.org/abs/1410.6029v2) (2014): 1–53. arXiv: [arXiv:1410.6029v2](https://arxiv.org/abs/1410.6029v2).
- Hinkley, S., et al. "1386 - High Contrast Imaging of Exoplanets and Exoplanetary Systems with JWST". Print.
- Hoeijmakers, H. J., et al. "Medium-resolution integral-field spectroscopy for high-contrast exoplanet imaging: Molecule maps of the β Pictoris system with SINFONI". *Astronomy and Astrophysics* 617. ISSN: 14320746. DOI: [10.1051/0004-6361/201832902](https://doi.org/10.1051/0004-6361/201832902). arXiv: [1802.09721](https://arxiv.org/abs/1802.09721) (2018): 1–11. arXiv: [1802.09721](https://arxiv.org/abs/1802.09721). arXiv: [1802.09721](https://arxiv.org/abs/1802.09721).
- Irwin, P. G., et al. "The NEMESIS planetary atmosphere radiative transfer and retrieval tool". *Journal of Quantitative Spectroscopy and Radiative Transfer* 109.6. ISSN: 00224073. DOI: [10.1016/j.jqsrt.2007.11.006](https://doi.org/10.1016/j.jqsrt.2007.11.006) (2008): 1136–1150. Print.
- Janson, M., et al. "Direct imaging detection of methane in the atmosphere of GJ 504 b". *Astrophysical Journal Letters* 778.1. ISSN: 20418205. DOI: [10.1088/2041-8205/778/1/L4](https://doi.org/10.1088/2041-8205/778/1/L4) (2013). Print.
- JWST. "JWST Pipeline Documentation". Print.
- Keppler, M., et al. "Discovery of a planetary-mass companion within the gap of the transition disk around PDS 70". *Astronomy and Astrophysics* 617. ISSN: 14320746. DOI: [10.1051/0004-6361/201832957](https://doi.org/10.1051/0004-6361/201832957). arXiv: [1806.11568](https://arxiv.org/abs/1806.11568) (2018): 1–21. arXiv: [1806.11568](https://arxiv.org/abs/1806.11568). arXiv: [1806.11568](https://arxiv.org/abs/1806.11568).
- Keppler, M., et al. "Discovery of a planetary-mass companion within the gap of the transition disk around PDS 70". *Astronomy & Astrophysics* 617. DOI: [10.1051/0004-6361/201832957](https://doi.org/10.1051/0004-6361/201832957). arXiv: [arXiv:1806.11568](https://arxiv.org/abs/1806.11568) (2018): 1–23. arXiv: [arXiv:1806.11568](https://arxiv.org/abs/1806.11568). arXiv: [arXiv:1806.11568](https://arxiv.org/abs/1806.11568).
- Konopacky, Q. M., T. S. Barman, B. A. Macintosh, and C. Marois. "Detection of carbon monoxide and water absorption lines in an exoplanet atmosphere". *Science* 339.6126. ISSN: 10959203. DOI: [10.1126/science.1232003](https://doi.org/10.1126/science.1232003) (2013): 1398–1401. Print.
- Kreidberg, L. "Exoplanet Atmosphere Measurements from Transmission Spectroscopy and Other Planet Star Combined Light Observations". *Handbook of Exoplanets*. DOI: [10.1007/978-3-319-55333-7_100](https://doi.org/10.1007/978-3-319-55333-7_100). arXiv: [arXiv:1709.05941v2](https://arxiv.org/abs/1709.05941v2) (2018): 2083–2105. arXiv: [arXiv:1709.05941v2](https://arxiv.org/abs/1709.05941v2). arXiv: [arXiv:1709.05941v2](https://arxiv.org/abs/1709.05941v2).
- Kreidberg, L., et al. "A precise water abundance measurement for the hot jupiter WASP-43b". *Astrophysical Journal Letters* 793.2. ISSN: 20418213. DOI: [10.1088/2041-8205/793/2/L27](https://doi.org/10.1088/2041-8205/793/2/L27). arXiv: [1410.2255](https://arxiv.org/abs/1410.2255) (2014): 2–7. arXiv: [1410.2255](https://arxiv.org/abs/1410.2255). arXiv: [1410.2255](https://arxiv.org/abs/1410.2255).
- Labiano-Ortega, A., et al. "The MIRI Medium Resolution Spectrometer calibration pipeline". *SPIE Astronomical Telescopes + Instrumentation*. Edinburgh, 2016. 117. Print.
- Lacis, A. A. and V. Oinas. "A description of the correlated k distribution method for modeling nongray gaseous absorption, thermal emission, and multiple scattering in vertically inhomogeneous atmospheres". *Journal of*

- Geophysical Research* 96.D5. ISSN: 01480227. DOI: [10.1029/90JD01945](https://doi.org/10.1029/90JD01945) (1991): 9027–9063. Print.
- Lacour, S., et al. "First direct detection of an exoplanet by optical interferometry". *Astronomy & Astrophysics* 623. ISSN: 0004-6361. DOI: [10.1051/0004-6361/201935253](https://doi.org/10.1051/0004-6361/201935253) (2019): L11. Print.
- Lafrenière, D., C. Marois, R. Doyon, and T. Barman. "HST/nicmos detection of HR 8799 B in 1998". *Astrophysical Journal* 694.2. ISSN: 15384357. DOI: [10.1088/0004-637X/694/2/L148](https://doi.org/10.1088/0004-637X/694/2/L148) (2009): 148–152. Print.
- Lagage, P.-o. and D. Barrado. "1278 - MIRI Spectroscopic Observations of Brown Dwarfs". Print.
- Lagage, P.-o., J. Bouwman, and F. Lahuis. "1275 - Spectroscopic characterization of PSO J318". Print.
- Lagage, P.-o. and T. L. Roellig. "1276 - Spectroscopic Observations of WD 0806-661B". Print.
- Lagage, P., et al. "The Mid-Infrared Instrument for the James Webb Space Telescope , IV : The Low Resolution Spectrometer". *Publications of the Astronomical Society of the Pacific* 127.953. DOI: [10.1086/682255](https://doi.org/10.1086/682255). arXiv: [1512:03000](https://arxiv.org/abs/1512.03000) (2015): 1–23. arXiv: [1512:03000](https://arxiv.org/abs/1512.03000). arXiv: [1512:03000](https://arxiv.org/abs/1512.03000).
- Lagrange, A. M., et al. "A probable giant planet imaged in the β Pictoris disk* VLT/NaCo deep L'-band imaging". *Astronomy and Astrophysics* 493.2. ISSN: 00046361. DOI: [10.1051/0004-6361:200811325](https://doi.org/10.1051/0004-6361:200811325) (2009): 21–25. Print.
- Lagrange, A. M., et al. "Evidence for an additional planet in the β Pictoris system". *Nature Astronomy* 3.12. ISSN: 23973366. DOI: [10.1038/s41550-019-0857-1](https://doi.org/10.1038/s41550-019-0857-1) (2019): 1135–1142. Web. <<http://dx.doi.org/10.1038/s41550-019-0857-1>>.
- Lahuis, F. and A. Boogert. "How to Get Rid of Fringes in SIRTF/IRS Data". *SFChem 2002: Chemistry as a Diagnostic of Star Formation*. Waterloo, 2003. 335. Print.
- Lahuis, F. and M. Muller. "MIRI MRS FM Fringing Analysis". Print.
- Lavie, B., et al. "HELIOS-RETRIEVAL: An Open-source, Nested Sampling Atmospheric Retrieval Code; Application to the HR 8799 Exoplanets and Inferred Constraints for Planet Formation ". *The Astronomical Journal* 154.3. ISSN: 0004-6256. DOI: [10.3847/1538-3881/aa7ed8](https://doi.org/10.3847/1538-3881/aa7ed8). arXiv: [1610.03216](https://arxiv.org/abs/1610.03216) (2017): 91. arXiv: [1610.03216](https://arxiv.org/abs/1610.03216). arXiv: [1610.03216](https://arxiv.org/abs/1610.03216).
- Lee, J. M., L. N. Fletcher, and P. G. Irwin. "Optimal estimation retrievals of the atmospheric structure and composition of HD189733b from secondary eclipse spectroscopy". *Monthly Notices of the Royal Astronomical Society* 420.1. ISSN: 00358711. DOI: [10.1111/j.1365-2966.2011.20013.x](https://doi.org/10.1111/j.1365-2966.2011.20013.x). arXiv: [1110.2934](https://arxiv.org/abs/1110.2934) (2012): 170–182. arXiv: [1110.2934](https://arxiv.org/abs/1110.2934). arXiv: [1110.2934](https://arxiv.org/abs/1110.2934).
- Leggett, S. K., C. V. Morley, M. S. Marley, and D. Saumon. "Near-infrared photometry of Y dwarfs: Low ammonia abundance and the onset of water clouds". *Astrophysical Journal* 799.1. ISSN: 15384357. DOI: [10.1088/0004-637X/799/1/37](https://doi.org/10.1088/0004-637X/799/1/37) (2015). Print.
- Li, J., D. B. Hibbert, S. Fuller, and G. Vaughn. "A comparative study of point-to-point algorithms for matching spectra". *Chemometrics and Intelligent Laboratory Systems* 82.1-2 SPEC. ISS. ISSN: 01697439. DOI: [10.1016/j.chemolab.2005.05.015](https://doi.org/10.1016/j.chemolab.2005.05.015) (2006): 50–58. Print.
- Line, M. R. and V. Parmentier. "the Influence of Nonuniform Cloud Cover on Transit Transmission Spectra". *The Astrophysical Journal* 820.1. ISSN: 153-

4357. DOI: [10.3847/0004-637X/820/1/78](https://doi.org/10.3847/0004-637X/820/1/78). arXiv: [1511.09443](https://arxiv.org/abs/1511.09443) (2016): 78. arXiv: [1511.09443](https://arxiv.org/abs/1511.09443). Web. <<http://dx.doi.org/10.3847/0004-637X/820/1/78>>.
- Line, M. R., et al. "A systematic retrieval analysis of secondary eclipse spectra. I. A comparison of atmospheric retrieval techniques". *Astrophysical Journal* 775.2. ISSN: 15384357. DOI: [10.1088/0004-637X/775/2/137](https://doi.org/10.1088/0004-637X/775/2/137). arXiv: [1304.5561](https://arxiv.org/abs/1304.5561) (2013). arXiv: [1304.5561](https://arxiv.org/abs/1304.5561). arXiv: [1304.5561](https://arxiv.org/abs/1304.5561).
- Line, M. R., et al. "Uniform Atmospheric Retrieval Analysis of Ultracool Dwarfs. I. Characterizing Benchmarks, Gl 570D and HD 3651B". *Astrophysical Journal* 807.2. ISSN: 15384357. DOI: [10.1088/0004-637X/807/2/183](https://doi.org/10.1088/0004-637X/807/2/183). arXiv: [1504.06670](https://arxiv.org/abs/1504.06670) (2015): 183. arXiv: [1504.06670](https://arxiv.org/abs/1504.06670). arXiv: [1504.06670](https://arxiv.org/abs/1504.06670). Web. <<http://dx.doi.org/10.1088/0004-637X/807/2/183>>.
- Line, M. R., et al. "Uniform Atmospheric Retrieval Analysis of Ultracool Dwarfs. II. Properties of 11 T dwarfs". *The Astrophysical Journal* 848.2. ISSN: 1538-4357. DOI: [10.3847/1538-4357/aa7ff0](https://doi.org/10.3847/1538-4357/aa7ff0). arXiv: [1612.02809](https://arxiv.org/abs/1612.02809) (2017): 83. arXiv: [1612.02809](https://arxiv.org/abs/1612.02809). arXiv: [1612.02809](https://arxiv.org/abs/1612.02809).
- Line, M. R., et al. "Astro2020 Science White Paper The Importance of Thermal Emission Spectroscopy for Understanding Terrestrial Exoplanets Thematic Areas". Print. Astro2020.
- López-Morales, M., et al. "Detecting Earth-like Biosignatures on Rocky Exoplanets around Nearby Stars with Ground-based Extremely Large Telescopes". arXiv: [1903.09523](https://arxiv.org/abs/1903.09523). Web. <<http://arxiv.org/abs/1903.09523>>. Astro2020.
- Luhman, K. L. "Discovery of a ~250K Brown Dwarf at 2pc from the Sun". *The Astrophysical Journal Letters* 18. doi: [10.1088/2041-8205/786/2/L18](https://doi.org/10.1088/2041-8205/786/2/L18) (2014): 2–7. Print.
- Lupu, R. E., et al. "Developing Atmospheric Retrieval Methods for Direct Imaging Spectroscopy of Gas Giants in Reflected Light. I. Methane Abundances and Basic Cloud Properties". *The Astronomical Journal* 152.6. ISSN: 0004-6256. DOI: [10.3847/0004-6256/152/6/217](https://doi.org/10.3847/0004-6256/152/6/217). arXiv: [1604.05370](https://arxiv.org/abs/1604.05370) (2016): 217. arXiv: [1604.05370](https://arxiv.org/abs/1604.05370). arXiv: [1604.05370](https://arxiv.org/abs/1604.05370). Web. <<http://dx.doi.org/10.3847/0004-6256/152/6/217>>.
- LUVOIR Mission Concept Study Team. "The LUVOIR Final Report". Print.
- MacDonald, R. J., J. M. Goyal, and N. K. Lewis. "Why is it so Cold in Here?: Explaining the Cold Temperatures Retrieved from Transmission Spectra of Exoplanet Atmospheres". arXiv: [2003.11548](https://arxiv.org/abs/2003.11548) (2020). arXiv: [2003.11548](https://arxiv.org/abs/2003.11548). arXiv: [2003.11548](https://arxiv.org/abs/2003.11548). Web. <<http://arxiv.org/abs/2003.11548>>.
- MacDonald, R. J. and N. Madhusudhan. "HD 209458b in new light: evidence of nitrogen chemistry, patchy clouds and sub-solar water". *Monthly Notices of the Royal Astronomical Society* 469.2. ISSN: 0035-8711. DOI: [10.1093/mnras/stx804](https://doi.org/10.1093/mnras/stx804). arXiv: [1701.01113](https://arxiv.org/abs/1701.01113) (2017): 1979–1996. arXiv: [1701.01113](https://arxiv.org/abs/1701.01113). arXiv: [1701.01113](https://arxiv.org/abs/1701.01113).
- Macintosh, B., et al. "Discovery and spectroscopy of the young jovian planet 51 Eri b with the Gemini Planet Imager". *Science* 350.6256. ISSN: 10959203. DOI: [10.1126/science.aac5891](https://doi.org/10.1126/science.aac5891) (2015): 64–67. Print.
- MacKay, D. J. *Information Theory, Inference, and Learning Algorithms*. Fourth Edi. Cambridge University Press, 2003. Print.
- Madhusudhan, N. and S. Seager. "A Temperature and Abundance Retrieval Method for Exoplanet Atmospheres". *The Astrophysical Journal* 707.1. DOI:

- [10.1088/0004-637X/707/1/24](https://doi.org/10.1088/0004-637X/707/1/24). arXiv: [arXiv:0910.1347v2](https://arxiv.org/abs/0910.1347v2) (2009): 24–39. arXiv: [arXiv:0910.1347v2](https://arxiv.org/abs/0910.1347v2). arXiv: [arXiv:0910.1347v2](https://arxiv.org/abs/0910.1347v2).
- Madhusudhan, N. “Atmospheric Retrieval of Exoplanets”. *Handbook of Exoplanets*. DOI: [10.1007/978-3-319-55333-7_104](https://doi.org/10.1007/978-3-319-55333-7_104). arXiv: [1808.04824](https://arxiv.org/abs/1808.04824) (2018): 2153–2182. arXiv: [1808.04824](https://arxiv.org/abs/1808.04824). arXiv: [1808.04824](https://arxiv.org/abs/1808.04824).
- .“C/O ratio as a dimension for characterizing exoplanetary atmospheres”. *Astrophysical Journal* 758.1. ISSN: 15384357. DOI: [10.1088/0004-637X/758/1/36](https://doi.org/10.1088/0004-637X/758/1/36). arXiv: [1209.2412](https://arxiv.org/abs/1209.2412) (2012). arXiv: [1209.2412](https://arxiv.org/abs/1209.2412). arXiv: [1209.2412](https://arxiv.org/abs/1209.2412).
- Madhusudhan, N., M. Agúndez, J. I. Moses, and Y. Hu. “Exoplanetary Atmospheres—Chemistry, Formation Conditions, and Habitability”. *Space Science Reviews* 205.1-4. ISSN: 15729672. DOI: [10.1007/s11214-016-0254-3](https://doi.org/10.1007/s11214-016-0254-3). arXiv: [arXiv:1604.06092v1](https://arxiv.org/abs/1604.06092v1) (2016): 285–348. arXiv: [arXiv:1604.06092v1](https://arxiv.org/abs/1604.06092v1). arXiv: [arXiv:1604.06092v1](https://arxiv.org/abs/1604.06092v1).
- Madhusudhan, N., D. Apai, and S. Gandhi. “Atmospheric Compositions of Three Brown Dwarfs and Implications for their Formation Conditions”. *arXiv eprint*. arXiv: [arXiv:1612.03174v1](https://arxiv.org/abs/1612.03174v1) (2018). arXiv: [arXiv:1612.03174v1](https://arxiv.org/abs/1612.03174v1). arXiv: [arXiv:1612.03174v1](https://arxiv.org/abs/1612.03174v1).
- Madhusudhan, N., H. Knutson, J. J. Fortney, and T. Barman. “Exoplanetary Atmospheres”. 2014. arXiv: [arXiv:1402.1169v1](https://arxiv.org/abs/1402.1169v1). arXiv: [arXiv:1402.1169v1](https://arxiv.org/abs/1402.1169v1).
- Madhusudhan, N., et al. “High C / O Ratio and Weak Thermal Inversion in the Very Hot Atmosphere of Exoplanet WASP-12b”. *Nature* 469.7328. DOI: [10.1038/nature09602](https://doi.org/10.1038/nature09602). arXiv: [arXiv:1012.1603](https://arxiv.org/abs/1012.1603) (2011): 64–67. arXiv: [arXiv:1012.1603](https://arxiv.org/abs/1012.1603). arXiv: [arXiv:1012.1603](https://arxiv.org/abs/1012.1603).
- Malik, M., et al. “Helios: an Open-Source, Gpu-Accelerated Radiative Transfer Code for Self-Consistent Exoplanetary Atmospheres”. *The Astronomical Journal* 153.2. ISSN: 0004-6256. DOI: [10.3847/1538-3881/153/2/56](https://doi.org/10.3847/1538-3881/153/2/56). arXiv: [1606.05474](https://arxiv.org/abs/1606.05474) (2017): 56. arXiv: [1606.05474](https://arxiv.org/abs/1606.05474). arXiv: [1606.05474](https://arxiv.org/abs/1606.05474). Web. <<http://dx.doi.org/10.3847/1538-3881/153/2/56>>.
- Malik, M., et al. “Self-luminous and Irradiated Exoplanetary Atmospheres Explored with HELIOS”. *The Astronomical Journal* 157.5. ISSN: 0004-6256. DOI: [10.3847/1538-3881/ab1084](https://doi.org/10.3847/1538-3881/ab1084). arXiv: [1903.06794](https://arxiv.org/abs/1903.06794) (2019): 170. arXiv: [1903.06794](https://arxiv.org/abs/1903.06794). arXiv: [1903.06794](https://arxiv.org/abs/1903.06794). Web. <<http://dx.doi.org/10.3847/1538-3881/ab1084>>.
- Malumuth, E. M., et al. “Removing the Fringes from Space Telescope Imaging Spectrograph Slitless Spectra”. *Publications of the Astronomical Society of the Pacific* 115.804. ISSN: 0004-6280. DOI: [10.1086/345913](https://doi.org/10.1086/345913) (2003): 218–234. Print.
- Mamajek, E. E. and C. P. Bell. “On the age of the β pictoris moving group”. *Monthly Notices of the Royal Astronomical Society* 445.3. ISSN: 13652966. DOI: [10.1093/mnras/stu1894](https://doi.org/10.1093/mnras/stu1894) (2014): 2169–2180. Print.
- Manjavacas, E. “Physical characterization of brown dwarfs”. Diss. Ruperto-Carola-University of Heidelberg, 2014. Print.
- Marley, M. S. and T. D. Robinson. “On the Cool Side : Modeling the Atmospheres of Brown Dwarfs and Giant Planets arXiv : 1410 . 6512v1 [astro-ph . EP] 23 Oct 2014”. *Annual Review of Astronomy and Astrophysics* 53. DOI: [10.1146/annurev-astro-082214-122522](https://doi.org/10.1146/annurev-astro-082214-122522). arXiv: [arXiv:1410.6512v1](https://arxiv.org/abs/1410.6512v1) (2015): 279–323. arXiv: [arXiv:1410.6512v1](https://arxiv.org/abs/1410.6512v1). arXiv: [arXiv:1410.6512v1](https://arxiv.org/abs/1410.6512v1).

- Marois, C., B. Macintosh, D. Nadeau, and D. Lafrenie. "Angular Differential Imaging: A Powerful High-Contrast Imaging Technique". *The Astrophysical Journal* 641 (2006): 556–564. Print.
- Marois, C., et al. "Direct imaging of multiple planets orbiting the star HR 8799". *Science* 322.5906. ISSN: 00368075. DOI: [10.1126/science.1166585](https://doi.org/10.1126/science.1166585). arXiv: [0811.2606](https://arxiv.org/abs/0811.2606) (2008): 1348–1352. arXiv: [0811.2606](https://arxiv.org/abs/0811.2606). arXiv: [0811.2606](https://arxiv.org/abs/0811.2606).
- Marois, C., et al. "Images of a fourth planet orbiting HR 8799". *Nature Letters* 468.23. DOI: [10.1038/nature09684](https://doi.org/10.1038/nature09684) (2010): 8–11. Print.
- Mayor, M. and D. Queloz. "A Jupiter-mass companion to a solar-type star". *Nature* 378 (1995): 667–668. Print.
- McLatchey, R., et al. "AFCRL atmospheric absorption line parameters compilation". *Environmental Research Papers* 434. ISSN: 0003-6935. DOI: [10.1364/ao.20.000791](https://doi.org/10.1364/ao.20.000791) (1973): 87. Print.
- Mesa, D., et al. "VLT/SPHERE exploration of the young multiplanetary system PDS70". *Astronomy and Astrophysics* 632. ISSN: 14320746. DOI: [10.1051/0004-6361/201936764](https://doi.org/10.1051/0004-6361/201936764). arXiv: [1910.11169](https://arxiv.org/abs/1910.11169) (2019): 1–12. arXiv: [1910.11169](https://arxiv.org/abs/1910.11169). arXiv: [1910.11169](https://arxiv.org/abs/1910.11169).
- Miles, B. E., et al. "Methane in Analogs of Young Directly Imaged Exoplanets". *The Astrophysical Journal* 869.1. ISSN: 1538-4357. DOI: [10.3847/1538-4357/aae6cd](https://doi.org/10.3847/1538-4357/aae6cd). arXiv: [1810.04684](https://arxiv.org/abs/1810.04684) (2018): 18. arXiv: [1810.04684](https://arxiv.org/abs/1810.04684). arXiv: [1810.04684](https://arxiv.org/abs/1810.04684). Web. <<http://dx.doi.org/10.3847/1538-4357/aae6cd>>.
- Mohanty, S., R. Jayawardhana, N. Huelamo, and E. Mamajek. "The Planetary Mass Companion 2MASS 1207-3932B: Temperature, Mass, and Evidence for an Edge-on Disk". *The Astrophysical Journal* 657.2. ISSN: 0004-637X. DOI: [10.1086/510877](https://doi.org/10.1086/510877) (2007): 1064–1091. Print.
- Molliere, P. and I. A. Snellen. "Detecting isotopologues in exoplanet atmospheres using ground-based high-dispersion spectroscopy". *Astronomy and Astrophysics* 622. ISSN: 14320746. DOI: [10.1051/0004-6361/201834169](https://doi.org/10.1051/0004-6361/201834169). arXiv: [1809.01156](https://arxiv.org/abs/1809.01156) (). arXiv: [1809.01156](https://arxiv.org/abs/1809.01156). arXiv: [1809.01156](https://arxiv.org/abs/1809.01156).
- Mollière, P., et al. "Observing transiting planets with JWST: Prime targets and their synthetic spectral observations". *Astronomy and Astrophysics* 600. ISSN: 14320746. DOI: [10.1051/0004-6361/201629800](https://doi.org/10.1051/0004-6361/201629800). arXiv: [1611.08608](https://arxiv.org/abs/1611.08608) (2017): 1–23. arXiv: [1611.08608](https://arxiv.org/abs/1611.08608). arXiv: [1611.08608](https://arxiv.org/abs/1611.08608).
- Mollière, P., et al. "petitRADTRANS: a Python radiative transfer package for exoplanet characterization and retrieval". *Astronomy & Astrophysics* 627. ISSN: 0004-6361. DOI: [10.1051/0004-6361/201935470](https://doi.org/10.1051/0004-6361/201935470). arXiv: [1904.11504](https://arxiv.org/abs/1904.11504) (2019): 1–17. arXiv: [1904.11504](https://arxiv.org/abs/1904.11504). arXiv: [1904.11504](https://arxiv.org/abs/1904.11504). Web. <<http://arxiv.org/abs/1904.11504%7B%5C%7D0Ahttp://dx.doi.org/10.1051/0004-6361/201935470>>.
- Mollière, P., et al. "Model Atmospheres of Irradiated Exoplanets: The Influence of Stellar Parameters, Metallicity and the C/O Ratio". *The Astrophysical Journal* 813.1. ISSN: 1538-4357. DOI: [10.1088/0004-637X/813/1/47](https://doi.org/10.1088/0004-637X/813/1/47) (2015): 47. Web. <<http://dx.doi.org/10.1088/0004-637X/813/1/47>>.
- Morley, C. V., et al. "An L Band Spectrum of the Coldest Brown Dwarf". *The Astrophysical Journal* 858.2. ISSN: 1538-4357. DOI: [10.3847/1538-4357/aabe8b](https://doi.org/10.3847/1538-4357/aabe8b). arXiv: [1804.07771](https://arxiv.org/abs/1804.07771) (2018): 97. arXiv: [1804.07771](https://arxiv.org/abs/1804.07771). arXiv: [1804.07771](https://arxiv.org/abs/1804.07771). Web. <<http://dx.doi.org/10.3847/1538-4357/aabe8b>>.

- Morley, C. V., et al. "Water clouds in γ dwarfs and exoplanets". *Astrophysical Journal* 787.1. ISSN: 15384357. DOI: [10.1088/0004-637X/787/1/78](https://doi.org/10.1088/0004-637X/787/1/78). arXiv: [1404.0005](https://arxiv.org/abs/1404.0005) (2014). arXiv: [1404.0005](https://arxiv.org/abs/1404.0005).
- Moroz, V. "On the infrared spectra of Jupiter and Saturn (0.9-2.5 μ m)". *Soviet Astronomy* 5.6 (1962). Print.
- Moses, J. I., N. Madhusudhan, C. Visscher, and R. S. Freedman. "Chemical consequences of the C/O ratio on hot jupiters: Examples from WASP-12b, CoRoT-2b, XO-1b, and HD 189733b". *Astrophysical Journal* 763.1. ISSN: 15384357. DOI: [10.1088/0004-637X/763/1/25](https://doi.org/10.1088/0004-637X/763/1/25). arXiv: [1211.2996](https://arxiv.org/abs/1211.2996) (2013). arXiv: [1211.2996](https://arxiv.org/abs/1211.2996). arXiv: [1211.2996](https://arxiv.org/abs/1211.2996).
- Müller, A., et al. "Orbital and atmospheric characterization of the planet within the gap of the PDS 70 transition disk". *Astronomy and Astrophysics* 617. ISSN: 14320746. DOI: [10.1051/0004-6361/201833584](https://doi.org/10.1051/0004-6361/201833584). arXiv: [1806.11567](https://arxiv.org/abs/1806.11567) (2018): 1–10. arXiv: [1806.11567](https://arxiv.org/abs/1806.11567). arXiv: [1806.11567](https://arxiv.org/abs/1806.11567).
- National Academies of Sciences Engineering and Medicine. *Exoplanet science strategy*. Washington, DC: The National Academies Press, 2018. 1–172. DOI: [10.17226/25187](https://doi.org/10.17226/25187). Print.
- Oliveira, C. A. D. "Peering into the physics of brown dwarfs : spectroscopy with JWST / NIRSpec". Web. <<https://www.cosmos.esa.int/documents/739790/758041/AlvesdeOliveiraC.pdf>>.
- Oliveira, C. A. D., et al. "1230 - The Physics of Brown Dwarfs - Part # 3". 1. Print.
- Oreshenko, M., et al. "Supervised Machine Learning for Inter-comparision of Model Grids of Brown Dwarfs: Application to GJ 570D and the Epsilon Indi B Binary System". *The Astronomical Journal* 159.1. DOI: [10.3847/1538-3881/ab5955](https://doi.org/10.3847/1538-3881/ab5955). arXiv: [arXiv:1910.11795v1](https://arxiv.org/abs/1910.11795v1) (2020): 15. arXiv: [arXiv:1910.11795v1](https://arxiv.org/abs/1910.11795v1). arXiv: [arXiv:1910.11795v1](https://arxiv.org/abs/1910.11795v1).
- Petermann, R. "Atmospheric characterization of terrestrial planets using high-resolution spectroscopy with ELT / METIS A study of Proxima Cen b". Master's Thesis. ETH Zurich, 2019. Print.
- Quanz, S. P., et al. "Atmospheric characterization of terrestrial exoplanets in the mid-infrared: biosignatures, habitability & diversity". arXiv: [1908.01316](https://arxiv.org/abs/1908.01316). Web. <<http://arxiv.org/abs/1908.01316>>. Voyage 2050 long-term plan.
- Quanz, S. P., et al. "First results from very large telescope NACO apodizing phase plate: 4 μ m images of the exoplanet β Pictoris b". *Astrophysical Journal Letters* 722.1 PART 2. ISSN: 20418213. DOI: [10.1088/2041-8205/722/1/L49](https://doi.org/10.1088/2041-8205/722/1/L49) (2010): 49–53. Print.
- Rameau, J., et al. "Confirmation of the Planet Around Hd 95086 By Direct Imaging". *The Astrophysical Journal* 779.2. ISSN: 2041-8205. DOI: [10.1088/2041-8205/779/2/l26](https://doi.org/10.1088/2041-8205/779/2/l26) (2013): L26. Print.
- Ressler, M. E., et al. "The Mid-Infrared Instrument for the James Webb Space Telescope , VIII: The MIRI Focal Plane System". *Publications of the Astronomical Society of the Pacific* 127.953. ISSN: 00046280. DOI: [10.1086/682258](https://doi.org/10.1086/682258) (2015): 675–685. Print.
- Rich, E. A., et al. "Thermal Infrared Imaging and Atmospheric Modeling of VHS J125601.92-125723.9 b: Evidence for Moderately Thick Clouds and Equilibrium Carbon Chemistry in a Hierarchical Triple System." *The Astrophysical Journal* 830.2. ISSN: 1538-4357. DOI: [10.3847/0004-637x/830/2/114](https://doi.org/10.3847/0004-637x/830/2/114).

- arXiv: [1607.06007](#) (2016): 114. arXiv: [1607.06007](#). arXiv: [1607.06007](#). Web. <<http://dx.doi.org/10.3847/0004-637X/830/2/114>>.
- Rieke, G. H., et al. "The Mid-Infrared Instrument for the James Webb Space Telescope , I: Introduction". *Publications of the Astronomical Society of the Pacific* 127.953. ISSN: 00046280. DOI: [10.1086/682252](#) (2015): 584–594. Print.
- ." The Mid-Infrared Instrument for the James Webb Space Telescope , I: Introduction ". *Publications of the Astronomical Society of the Pacific* 127.953. ISSN: 00046280. DOI: [10.1086/682252](#) (2015): 584–594. Print.
- Rieke, G. H., et al. "The Mid-Infrared Instrument for the James Webb Space Telescope , VII: The MIRI Detectors". *Publications of the Astronomical Society of the Pacific* 127.953. ISSN: 00046280. DOI: [10.1086/682257](#) (2015): 665–674. Print.
- Robinson, T. D., K. R. Stapelfeldt, and M. S. Marley. "Characterizing rocky and gaseous exoplanets with 2m class space-based coronagraphs". *Publications of the Astronomical Society of the Pacific* 128.960. ISSN: 00046280. DOI: [10.1088/1538-3873/128/960/025003](#) (2016): 1–22. Web. <<http://dx.doi.org/10.1088/1538-3873/128/960/025003>>.
- Rothman, L. S. "AFGL atmospheric absorption line parameters compilation: 1980 version". *Applied Optics* 20.5. ISSN: 0003-6935. DOI: [10.1364/ao.20.000791](#) (1981): 791. Print.
- Rothman, L. S., et al. "HITEMP, the high-temperature molecular spectroscopic database". *Journal of Quantitative Spectroscopy and Radiative Transfer* 111.15. ISSN: 00224073. DOI: [10.1016/j.jqsrt.2010.05.001](#) (2010): 2139–2150. Web. <<http://dx.doi.org/10.1016/j.jqsrt.2010.05.001>>.
- Rothman, L. S., et al. "The HITRAN2012 molecular spectroscopic database". *Journal of Quantitative Spectroscopy and Radiative Transfer* 130. ISSN: 00224073. DOI: [10.1016/j.jqsrt.2013.07.002](#) (2013): 4–50. Print.
- Sahlmann, J. and P. F. Lazorenko. "Mass ratio of the 2 pc binary brown dwarf LUH 16 and limits on planetary companions from astrometry". *Monthly Notices of the Royal Astronomical Society: Letters* 453.1. ISSN: 17453933. DOI: [10.1093/mnrasl/slv113](#). arXiv: [1506.07994](#) (2015): L103–L107. arXiv: [1506.07994](#). arXiv: [1506.07994](#).
- Sallum, S., et al. "Accreting protoplanets in the LkCa 15 transition disk". *Nature* 527.7578. ISSN: 14764687. DOI: [10.1038/nature15761](#). arXiv: [1511.07456](#) (2015): 342–344. arXiv: [1511.07456](#). arXiv: [1511.07456](#). Web. <<http://dx.doi.org/10.1038/nature15761>>.
- Schlawin, E., et al. "Clear and Cloudy Exoplanet Forecasts for JWST : Maps, Retrieved Composition, and Constraints on Formation with MIRI and NIRCam ". *The Astronomical Journal* 156.1. ISSN: 0004-6256. DOI: [10.3847/1538-3881/aac774](#). arXiv: [1803.08173](#) (2018): 40. arXiv: [1803.08173](#). arXiv: [1803.08173](#).
- Schneider, A. C., M. C. Cushing, J. D. Kirkpatrick, and C. R. Gelino. "the Collapse of the Wien Tail in the Coldest Brown Dwarf? Hubble Space Telescope Near-Infrared Photometry of WISE J085510.83-071442.5". *The Astrophysical Journal* 823.2. ISSN: 2041-8213. DOI: [10.3847/2041-8205/823/2/L35](#). arXiv: [1605.05618](#) (2016): L35. arXiv: [1605.05618](#). arXiv: [1605.05618](#). Web. <<http://dx.doi.org/10.3847/2041-8205/823/2/L35>>.

- Seager, S. and D. Deming. "Exoplanet Atmospheres". *Annual Review of Astronomy and Astrophysics* 48.1. ISSN: 0066-4146. DOI: [10.1146/annurev-astro-081309-130837](https://doi.org/10.1146/annurev-astro-081309-130837). arXiv: [1005.4037](https://arxiv.org/abs/1005.4037) (2010): 631–672. arXiv: [1005.4037](https://arxiv.org/abs/1005.4037). arXiv: [1005.4037](https://arxiv.org/abs/1005.4037).
- Simkin, S. M. "Measurements of Velocity Dispersions and Doppler Shifts from Digitized Optical Spectra". *Astronomy & Astrophysics* 32 (1974): 129–136. Print.
- Sing, D. K., J. J. Fortney, J. Tennyson, and D. Grassi. *Astrophysics of Exoplanetary Atmospheres*. Edited by V. Bozza, L. Mancini, and A. Sozzetti. Vietri sul Mare: Springer Nature, 2018. 199. DOI: [10.1007/978-3-319-89701-1](https://doi.org/10.1007/978-3-319-89701-1). Print.
- Skemer, A. J., et al. "First light LBT AO images of HR 8799 bcde at 1.6 and 3.3 μm: New discrepancies between young planets and old brown dwarfs". *Astrophysical Journal* 753.1. ISSN: 15384357. DOI: [10.1088/0004-637X/753/1/14](https://doi.org/10.1088/0004-637X/753/1/14). arXiv: [1203.2615](https://arxiv.org/abs/1203.2615) (2012). arXiv: [1203.2615](https://arxiv.org/abs/1203.2615). arXiv: [1203.2615](https://arxiv.org/abs/1203.2615).
- Skemer, A. J., et al. "The First Spectrum of the Coldest Brown Dwarf". *The Astrophysical Journal* 826.2. ISSN: 2041-8213. DOI: [10.3847/2041-8205/826/2/l17](https://doi.org/10.3847/2041-8205/826/2/l17). arXiv: [1605.04902](https://arxiv.org/abs/1605.04902) (2016): L17. arXiv: [1605.04902](https://arxiv.org/abs/1605.04902). arXiv: [1605.04902](https://arxiv.org/abs/1605.04902). Web. <<http://dx.doi.org/10.3847/2041-8205/826/2/L17>>.
- Skemer, A. J., et al. "The LEECH Exoplanet Imaging Survey: Characterization of the Coldest Directly Imaged Exoplanet, GJ 504 b, and Evidence for Super-Stellar Metallicity". *The Astrophysical Journal* 817.2. ISSN: 1538-4357. DOI: [10.3847/0004-637x/817/2/166](https://doi.org/10.3847/0004-637x/817/2/166). arXiv: [1511.09183](https://arxiv.org/abs/1511.09183) (2016): 166. arXiv: [1511.09183](https://arxiv.org/abs/1511.09183). arXiv: [1511.09183](https://arxiv.org/abs/1511.09183). Web. <<http://dx.doi.org/10.3847/0004-637X/817/2/166>>.
- Skilling, J. "Nested Sampling". *Bayesian Inference and Maximum Entropy Methods in Science and Engineering*. 2004. 395–405. Print.
- Snellen, I., et al. "Combining high-dispersion spectroscopy with high contrast imaging: Probing rocky planets around our nearest neighbors". *Astronomy and Astrophysics* 576.3. ISSN: 14320746. DOI: [10.1051/0004-6361/201425018](https://doi.org/10.1051/0004-6361/201425018). arXiv: [1503.01136](https://arxiv.org/abs/1503.01136) (2015). arXiv: [1503.01136](https://arxiv.org/abs/1503.01136). arXiv: [1503.01136](https://arxiv.org/abs/1503.01136).
- Snellen, I., et al. "The fast spin-rotation of a young extrasolar planet". *Nature* 509.7498. ISSN: 0028-0836, 1476-4687. DOI: [10.1038/nature13253](https://doi.org/10.1038/nature13253). arXiv: [1404.7506 \[astro-ph.EP\]](https://arxiv.org/abs/1404.7506) (2014): 63–65. arXiv: [1404.7506 \[astro-ph.EP\]](https://arxiv.org/abs/1404.7506). arXiv: [1404.7506 \[astro-ph.EP\]](https://arxiv.org/abs/1404.7506). Web. <<http://arxiv.org/abs/1404.7506>>.
- Soummer, R., et al. "Orbital motion of HR 8799 b, c, d using hubble space telescope data from 1998: Constraints on inclination, eccentricity, and stability". *Astrophysical Journal* 741.1. ISSN: 15384357. DOI: [10.1088/0004-637X/741/1/55](https://doi.org/10.1088/0004-637X/741/1/55). arXiv: [1110.1382](https://arxiv.org/abs/1110.1382) (2011). arXiv: [1110.1382](https://arxiv.org/abs/1110.1382). arXiv: [1110.1382](https://arxiv.org/abs/1110.1382).
- Speagle, J. S. "dynest: A Dynamic Nested Sampling Package for Estimating Bayesian Posteriors and Evidences". *Monthly Notices of the Royal Astronomical Society* 4. ISSN: 0035-8711. DOI: [10.1093/mnras/staa278](https://doi.org/10.1093/mnras/staa278) (2020). Print.
- . "A Conceptual Introduction to Markov Chain Monte Carlo Methods". *Journal of Statistics Education*. arXiv: [1909.12313](https://arxiv.org/abs/1909.12313) (2019). arXiv: [1909.12313](https://arxiv.org/abs/1909.12313). arXiv: [1909.12313](https://arxiv.org/abs/1909.12313). Web. <<http://arxiv.org/abs/1909.12313>>.

- Stephens, D. C., et al. "The 0.8–14.5 μm Spectra of mid-L to mid-T dwarfs: Diagnostics of effective temperature, grain sedimentation, gas transport, and surface gravity". *Astrophysical Journal* 702.1. ISSN: 15384357. DOI: 10.1088/0004-637X/702/1/154 (2009): 154–170. Print.
- Stolker, T., et al. "MIRACLES: atmospheric characterization of directly imaged planets and substellar companions at 4–5 micron. I. Photometric analysis of β Pic b, HIP 65426 b, PZ Tel B and HD 206893 B". *arXiv ePrint in Press*. arXiv: 1912.13316 (2020): 1–25. arXiv: 1912.13316. arXiv: 1912.13316. Web. <<http://arxiv.org/abs/1912.13316>>.
- Stone, J. M., et al. "Adaptive Optics Imaging of Vhs 1256–1257: a Low Mass Companion To a Brown Dwarf Binary System". *The Astrophysical Journal* 818.1. ISSN: 2041-8213. DOI: 10.3847/2041-8205/818/1/L12 (2016): L12. Web. <<http://dx.doi.org/10.3847/2041-8205/818/1/L12>>.
- Taylor, J., et al. "Understanding and Mitigating Biases when Studying Inhomogeneous Emission Spectra with JWST". *accepted Monthly Notices of the Royal Astronomical Society in Press*. February. arXiv: 2002.00773 (2020): 1–13. arXiv: 2002.00773. arXiv: 2002.00773. Web. <<http://arxiv.org/abs/2002.00773>>.
- Tennyson, J. and S. N. Yurchenko. "The ExoMol project: Software for computing large molecular line lists". *International Journal of Quantum Chemistry* 117.2. ISSN: 1097461X. DOI: 10.1002/qua.25190. arXiv: 1607.01220 (2017): 92–103. arXiv: 1607.01220. arXiv: 1607.01220.
- Tennyson, J., et al. "The ExoMol database: Molecular line lists for exoplanet and other hot atmospheres". *Journal of Molecular Spectroscopy* 327. ISSN: 1096083X. DOI: 10.1016/j.jms.2016.05.002. arXiv: 1603.05890 (2016): 73–94. arXiv: 1603.05890. arXiv: 1603.05890. Web. <<http://dx.doi.org/10.1016/j.jms.2016.05.002>>.
- Tinney, C. G., et al. "The Luminosities of the Coldest Brown Dwarfs". *The Astrophysical Journal* 39. Luhman. DOI: 10.1088/0004-637X/796/1/39 (2014): 1–13. Print.
- Tokunaga, A. T. "High-Resolution Infrared Spectroscopy of Planetary Atmospheres". *Publications of the Astronomical Society of the Pacific* 95. October (1983): 691–699. Print.
- Tremblin, P., et al. "Fingering convection and cloudless models for cool brown dwarf atmospheres". *Astrophysical Journal Letters* 804.1. ISSN: 20418213. DOI: 10.1088/2041-8205/804/1/L17. arXiv: 1504.03334 (2015): 6. arXiv: 1504.03334. arXiv: 1504.03334. Web. <<http://dx.doi.org/10.1088/2041-8205/804/1/L17>>.
- Tsiaras, A., et al. "Water vapour in the atmosphere of the habitable-zone eight-Earth-mass planet K2-18 b". *Nature Astronomy* 3.12. ISSN: 23973366. DOI: 10.1038/s41550-019-0878-9. arXiv: 1909.05218 (2019): 1086–1091. arXiv: 1909.05218. arXiv: 1909.05218. Web. <<http://dx.doi.org/10.1038/s41550-019-0878-9>>.
- Turrini, D., R. P. Nelson, and M. Barbieri. "The role of planetary formation and evolution in shaping the composition of exoplanetary atmospheres". *Experimental Astronomy* 40.2–3. DOI: 10.1007/s10686-014-9401-6 (2015): 501–522. Print.
- VanderPlas, J. T. "Understanding the Lomb–Scargle Periodogram". *The Astrophysical Journal Supplement Series* 236.1. ISSN: 0067-0049. DOI: 10.3847/

- 1538-4365/aab766. arXiv: 1703.09824 (2018): 16. arXiv: 1703.09824. arXiv: 1703.09824. Web. <<http://dx.doi.org/10.3847/1538-4365/aab766>>.
- Villanueva, G. L., et al. "Planetary Spectrum Generator: An accurate online radiative transfer suite for atmospheres, comets, small bodies and exoplanets". *Journal of Quantitative Spectroscopy and Radiative Transfer* 217. ISSN: 00224073. DOI: 10.1016/j.jqsrt.2018.05.023. arXiv: 1803.02008 (2018): 86–104. arXiv: 1803.02008. arXiv: 1803.02008. Web. <<https://doi.org/10.1016/j.jqsrt.2018.05.023>>.
- Vos, J. M., et al. "Astro2020 White Paper: The L/T Transition". arXiv: 1903.06691. Web. <<http://arxiv.org/abs/1903.06691>>. Astro2020.
- Waldmann, I. P., et al. "T-Rex. II. Retrieval of Emission Spectra". *Astrophysical Journal* 813.1. ISSN: 15384357. DOI: 10.1088/0004-637X/813/1/13. arXiv: 1508.07591 (2015): 13. arXiv: 1508.07591. arXiv: 1508.07591. Web. <<http://dx.doi.org/10.1088/0004-637X/813/1/13>>.
- Waldmann, I. P., et al. "Tau-Rex I: A next generation retrieval code for exoplanetary atmospheres". *Astrophysical Journal* 802.2. ISSN: 15384357. DOI: 10.1088/0004-637X/802/2/107. arXiv: 1409.2312 (2015): 107. arXiv: 1409.2312. arXiv: 1409.2312. Web. <<http://dx.doi.org/10.1088/0004-637X/802/2/107>>.
- Wells, M., et al. "The Mid-Infrared Instrument for the James Webb Space Telescope , VI: The Medium Resolution Spectrometer". *Publications of the Astronomical Society of the Pacific* 127.953. ISSN: 00046280. DOI: 10.1086/682281. arXiv: 1508.03070 (2015): 646–664. arXiv: 1508.03070. arXiv: 1508.03070.
- Wright, E. L., et al. "NEOWISE-R observation of the coolest known brown dwarf". *Astronomical Journal* 148.5. ISSN: 00046256. DOI: 10.1088/0004-6256/148/5/82 (2014): 2012–2015. Print.
- Wright, G. S., et al. "The Mid-Infrared Instrument for JWST , II : Design and Build". *Publications of the Astronomical Society of the Pacific* 127.953. DOI: 10.1086/682253. arXiv: 1508.02333 (2015): 595. arXiv: 1508.02333. arXiv: 1508.02333.
- Yurchenko, S. N., A. F. Al-Refaie, and J. Tennyson. "EXO CROSS: A general program for generating spectra from molecular line lists". *Astronomy and Astrophysics* 614. ISSN: 14320746. DOI: 10.1051/0004-6361/201732531. arXiv: 1801.09803 (2018): 1–12. arXiv: 1801.09803. arXiv: 1801.09803.
- Zalesky, J. A., M. R. Line, A. C. Schneider, and J. Patience. "A Uniform Retrieval Analysis of Ultra-cool Dwarfs. III. Properties of Y Dwarfs". *The Astrophysical Journal* 877.1. ISSN: 1538-4357. DOI: 10.3847/1538-4357/ab16db. arXiv: 1903.11658 (2019): 24. arXiv: 1903.11658. arXiv: 1903.11658.
- Zhang, M., Y. Chachan, E. M. Kempton, and H. A. Knutson. "Forward modeling and retrievals with PLATON, a fast open-source tool". *Publications of the Astronomical Society of the Pacific* 131.997. ISSN: 00046280. DOI: 10.1088/1538-3873/aaf5ad. arXiv: 1811.11761 (2019). arXiv: 1811.11761. arXiv: 1811.11761.
- Zhou, Y., et al. "Cloud Atlas: High-contrast Time-resolved Observations of Planetary-mass Companions". *The Astronomical Journal* 157.3. ISSN: 0004-6256. DOI: 10.3847/1538-3881/ab037f. arXiv: 1902.00085 (2019): 128. arXiv: 1902.00085. arXiv: 1902.00085. Web. <<http://dx.doi.org/10.3847/1538-3881/ab037f>>.

Zucker, S. "Cross-correlation and maximum-likelihood analysis : a new approach to combining cross-correlation functions". *Monthly Notices of the Royal Astronomical Society* 342 (2003): 1291–1298. Print.

Zurlo, A., et al. "First light of the VLT planet finder SPHERE: III. New spectrophotometry and astrometry of the HR 8799 exoplanetary system". *Astronomy and Astrophysics* 587. ISSN: 14320746. DOI: [10.1051/0004-6361/201526835](https://doi.org/10.1051/0004-6361/201526835). arXiv: [1511.04083](https://arxiv.org/abs/1511.04083) (2016): 1–13. arXiv: [1511.04083](https://arxiv.org/abs/1511.04083). arXiv: [1511.04083](https://arxiv.org/abs/1511.04083).